The Optoelectronic Swept-Frequency Laser and Its Applications in Ranging, Three-Dimensional Imaging, and Coherent Beam Combining of Chirped-Seed Amplifiers

Thesis by

Arseny Vasilyev

In Partial Fulfillment of the Requirements

for the Degree of

Doctor of Philosophy

California Institute of Technology

Pasadena, California

2013

(Defended May 20, 2013)

Acknowledgments

I am deeply thankful to my advisor, Prof. Amnon Yariv, for taking me into his research group and providing an environment in which I had the freedom to pursue original ideas. Prof. Yariv's advice has been key in picking the direction of our work and his expertise in optical physics has been a continuous source of inspiration.

I thank Profs. Bruno Crosignani, Keith Schwab, Kerry Vahala, and Changhuei Yang for serving on my thesis committee.

I was trained to conduct experiments in optoelectronics by Dr. Naresh Satyan, and I am deeply thankful for his instruction and his patience. I also learned a great deal from Dr. George Rakuljic, and am thankful for his support and for the many technical discussions that we had over the years.

I would like to acknowledge our collaborators at the United States Army Research Laboratories. Dr. Jeffrey White made it possible for us to participate in an exciting research program, and on a few occasions hosted us at the US ARL. I am thankful to have had the opportunity to work with and learn from Dr. White's team and his colleagues: Dr. Eliot Petersen, Dr. Olukayode Okusaga, Dr. Carl Mungan, James Cahill, and Zhi Yang.

I am also thankful to our collaborators at the Jet Propulsion Laboratory: Dr. Baris Erkmen, Dr. John Choi, and Dr. William Farr.

My fellow Yariv group members have supported and encouraged me throughout the years, and I am deeply grateful to have been surrounded with such kind and talented individuals. I have enjoyed my time with Prof. Bruno Crosignani, Prof. Avi Zadok, Dr. Naresh Satyan, Dr. George Rakuljic, Dr. Jacob Sendowski, Dr. Christos Santis, Dr. Hsi-Chun Liu, Dr. Xiankai Sun, Scott Steger, Yasha Vilenchik, Mark

Harfouche, Marilena Dimotsantou, Sinan Zhao, and Dongwan Kim. I am particularly thankful to Dr. Reg Lee for the excellent technical advice that he has given to us over the years. I am grateful to Connie Rodriguez for taking care of all of us and for making sure that I started writing my thesis on time. I would also like to acknowledge Alireza Ghaari, Kevin Cooper and Mabel Chik for their support.

I want to thank my parents and family for their love, support, and patience with me on this journey. Lastly, I want to thank my new best friend, Debi, for filling my life with joy and happiness over these last several months.

Abstract

This thesis explores the design, construction, and applications of the optoelectronic swept-frequency laser (SFL). The optoelectronic SFL is a feedback loop designed around a swept-frequency (chirped) semiconductor laser (SCL) to control its instantaneous optical frequency, such that the chirp characteristics are determined solely by a reference electronic oscillator. The resultant system generates precisely controlled optical frequency sweeps. In particular, we focus on linear chirps because of their numerous applications. We demonstrate optoelectronic SFLs based on vertical-cavity surface-emitting lasers (VCSELs) and distributed-feedback lasers (DFBs) at wavelengths of 1550 nm and 1060 nm. We develop an iterative bias current predistortion procedure that enables SFL operation at very high chirp rates, up to 10^{16} Hz/sec. We describe commercialization efforts and implementation of the predistortion algorithm in a stand-alone embedded environment, undertaken as part of our collaboration with Telaris, Inc. We demonstrate frequency-modulated continuous-wave (FMCW) ranging and three-dimensional (3-D) imaging using a 1550 nm optoelectronic SFL.

We develop the technique of multiple source FMCW (MS-FMCW) reflectometry, in which the frequency sweeps of multiple SFLs are "stitched" together in order to increase the optical bandwidth, and hence improve the axial resolution, of an FMCW ranging measurement. We demonstrate computer-aided stitching of DFB and VCSEL sweeps at 1550 nm. We also develop and demonstrate hardware stitching, which enables MS-FMCW ranging without additional signal processing. The culmination of this work is the hardware stitching of four VCSELs at 1550 nm for a total optical bandwidth of 2 THz, and a free-space axial resolution of 75 μm.

We describe our work on the tomographic imaging camera (TomICam), a 3-D

imaging system based on FMCW ranging that features non-mechanical acquisition of transverse pixels. Our approach uses a combination of electronically tuned optical sources and low-cost full-field detector arrays, completely eliminating the need for moving parts traditionally employed in 3-D imaging. We describe the basic TomICam principle, and demonstrate single-pixel TomICam ranging in a proof-of-concept experiment. We also discuss the application of compressive sensing (CS) to the TomICam platform, and perform a series of numerical simulations. These simulations show that tenfold compression is feasible in CS TomICam, which effectively improves the volume acquisition speed by a factor ten.

We develop chirped-wave phase-locking techniques, and apply them to coherent beam combining (CBC) of chirped-seed amplifiers (CSAs) in a master oscillator power amplifier configuration. The precise chirp linearity of the optoelectronic SFL enables non-mechanical compensation of optical delays using acousto-optic frequency shifters, and its high chirp rate simultaneously increases the stimulated Brillouin scattering (SBS) threshold of the active fiber. We characterize a 1550 nm chirped-seed amplifier coherent-combining system. We use a chirp rate of 5×10^{14} Hz/sec to increase the amplifier SBS threshold threefold, when compared to a single-frequency seed. We demonstrate efficient phase-locking and electronic beam steering of two 3 W erbium-doped fiber amplifier channels, achieving temporal phase noise levels corresponding to interferometric fringe visibilities exceeding 98%.

Contents

List of Figures

List of Tables

Glossary of Acronyms

2-D two-dimensional

3-D three-dimensional

AOFS acousto-optic frequency shifter

CBC coherent beam combining

CHDL chirped diode laser

CS compressive sensing

CSA chirped-seed amplifier

DDS direct digital synthesis

DFB distributed-feedback laser

EDFA erbium-doped fiber amplifier

FDML Fourier-domain mode-locked

FM frequency modulation

FMCW frequency-modulated continuous-wave

FSR free spectral range

FT Fourier transform

FWHM full width at half maximum

GRIN gradient-index

I/Q in-phase and quadrature

lidar light detection and ranging

MEMS microelectromechanical

MOPA master oscillator power amplifier

MS-FMCW multiple source FMCW

MZI Mach-Zehnder interferometer

OPLL optical phase-locked loop

PCB printed circuit board

PD photodetector

PLL phase-locked loop

PSD power spectral density

PSF point spread function

radar radio detection and ranging

RF radio frequency

RIN relative intensity noise

SBS stimulated Brillouin scattering

SCL semiconductor laser

SER signal-to-error ratio

SFL swept-frequency laser

SNR signal-to-noise ratio

SOA semiconductor optical amplifier

SS-OCT swept-source optical coherence tomography

TOF time-of-flight

TomICam tomographic imaging camera

VCO voltage-controlled oscillator

VCSEL vertical-cavity surface-emitting laser

VOA variable optical attenuator

Chapter 1

Overview and Thesis Organization

1.1 Introduction

This thesis focuses on the construction and applications of the optoelectronic swept-frequency laser (SFL)—a feedback system that enables closed-loop control over the instantaneous optical frequency of a chirped semiconductor laser (SCL) [1–3]. Even though our feedback architecture is laser-agnostic, we restrict our attention to SCL diodes because of their small size, high wall-plug efficiency, and superior sub-MHz linewidths. The wide gain bandwidth of semiconductor quantum wells, the ability to fabricate SCLs with precisely controlled emission frequencies [4], and the fact that SCLs can be frequency tuned with current [5] enable broadband and agile coverage of the optical spectrum. These properties uniquely position the SCL as the device of choice for a range of high-fidelity applications, such as optical phase-locking and coherent combining [6–12], ranging and 3-D imaging [1, 13, 14], and spectroscopy and chemical sensing [6, 15]. The design and construction of the optoelectronic SFL is discussed in chapter 3.

The optoelectronic SFL can be configured to generate chirps with any arbitrary optical frequency vs. time profile, subject to the tunability of the SCL in its core. Precisely linear frequency sweeps are of particular interest because of their applications in optical frequency-modulated continuous-wave (FMCW) reflectometry and 3-D imaging, as described in chapter 2, and chirped-seed phase-locking, as described in chapter 6. Building on our group's expertise in the field of phase and frequency

control of SCLs, we develop applications that take advantage of the unique properties of the SCL-based optoelectronic SFL. These applications can be subdivided into two categories: ranging and 3-D imaging using FMCW reflectometry, and coherent beam combining (CBC) of chirped-seed amplifiers (CSAs).

1.2 Ranging and 3-D Imaging Applications

The fundamental challenge of 3-D imaging is ranging—the retrieval of depth information from a scene or a sample. One way to construct a 3-D imaging system is to launch a laser beam along a particular axis, and collect the reflected light, in an effort to determine the depths of all the scatterers encountered by the beam as it propagates. A 3-D image may then be recorded by scanning the beam over the entire object space.

A conceptually simple way to retrieve depth information is to launch optical pulses, and record arrival times of the reflections. Scatterer depth can then be calculated by multiplying the arrival times by the speed of light c. Implementations based on this idea, collectively known as time-of-flight (TOF) systems, have been successfully demonstrated [16, 17]. The depth resolution, also called range resolution or axial resolution, of TOF methods depends on the system detection bandwidth, with 1 GHz yielding a resolution of $\Delta z \propto c \times (1\text{ ns}) = 30$ cm in free space. Improvement of the resolution to the sub-mm range requires detectors with 100s of GHz of bandwidth, and is prohibitively expensive with current technology.

1.2.1 Optical FMCW Reflectometry

The technique of frequency-modulated continuous-wave (FMCW) reflectometry, originally developed for radio detection and ranging (radar), can be applied to the optical domain to circumvent the detector bandwidth limit by using a swept-frequency optical waveform. Systems utilizing FMCW reflectometry, also known as swept-source optical coherence tomography (SS-OCT) in the biomedical optics community, are capable of

resolutions of a few μm with low detection bandwidths. As a result, FMCW reflectometry has found numerous applications, e.g. light detection and ranging (lidar) [18,19], biomedical imaging [20, 21], non-contact profilometry [22, 23] and biometrics [24, 25].

The FMCW technique is analyzed in full detail in chapter 2, and in chapter 3 we apply the optoelectronic SFL to FMCW imaging and demonstrate a simple profilometry application.

1.2.2 Multiple Source FMCW Reflectometry

In chapter 4 we describe multiple source FMCW (MS-FMCW) reflectometry—a novel imaging approach aimed at increasing the effective bandwidth of an FMCW ranging system. This is achieved by combining, or stitching, separate swept-frequency lasers (SFLs), to approximate a swept-source with an enhanced bandwidth [13,14,19]. The result is an improvement in the range resolution proportional to the increase in the swept-frequency range. This technique is of particular interest in the context of the SCL-based optoelectronic SFL. MS-FMCW leverages narrow SCL linewidths to present a pathway towards long-distance ranging systems with sub-100 μm resolutions.

1.2.3 The Tomographic Imaging Camera

FMCW reflectometry enables the retrieval of depth information from a single location in the transverse plane. One way to acquire a full 3-D data set is through mechanical raster-scanning of the laser beam across the object space. The acquisition time in such systems is ultimately limited by the scan speed, and for very high resolution datasets ($>$ 1 transverse mega pixel) is prohibitively slow. Rapid 3-D imaging is of crucial importance in *in vivo* biomedical diagnostics [21, 26] because it reduces artifacts introduced by patient motion. In addition, a high-throughput, non-destructive 3-D imaging technology is necessary to meet the requirements of several new industrial developments, including 3-D printing and manufacturing [27], 3-D tissue engineering [28–30], and 3-D cell cultures and tissue models [31].

In chapter 5 we discuss the tomographic imaging camera (TomICam), which combines FMCW ranging with non-mechanical transverse imaging, enabling robust, large field of view, and rapid 3-D imaging. We also discuss the application of compressive sensing (CS) to the TomICam platform. CS is an acquisition methodology that takes advantage of signal structure to compress and sample the information in a single step. It is of particular interest in applications involving large data sets, such as 3-D imaging, because compression reduces the volume of information that is recorded by the sensor, effectively speeding up the measurement.

1.3 Phase-Locking and Coherent Combining of Chirped Optical Waves

In chapter 6, we switch gears and discuss our work on the phase-locking of and coherent combining of chirped optical waves. The phase-locking of optical waves with arbitrary frequency chirps is a difficult problem in general. However, precisely linear chirps, such as the ones generated by the optoelectronic SFL can be phase-locked with very high efficiency using a frequency shifter. The main application of this result is the simultaneous stimulated Brillouin scattering (SBS) suppression and coherent combining of high-power fiber amplifiers.

The output power of optical fiber amplifiers is usually limited by SBS. Conventional methods to suppress SBS by increasing its threshold include the broadening of the seed laser linewidth through high-speed phase modulation. The increase in the amplifier SBS threshold comes at the expense of the seed coherence length [32], which places strict path-length matching requirements on the scaling of optical power through coherent combining of multiple amplifiers. Efficient coherent combining of such amplifiers has been demonstrated, but requires careful path-length matching to submillimeter accuracy [33, 34].

In chapter 6 we explore an architecture capable of SBS suppression and coherent combining without stringent mechanical path-length matching requirements. Our

approach is to use the optoelectronic SFL as the amplifier seed, in order to reduce the effective length over which SBS occurs [35, 36]. We develop a chirped phase-locking technique and demonstrate its use in coherent beam combining of multiple chirped-seed amplifiers. Path-length matching requirements are relaxed due to the long coherence length (10s of meters) of semiconductor laser based SFLs.

The work described in chapter 6 was performed in collaboration with Jeffrey O. White's group at the United States Army Research Laboratory.

Chapter 2

Optical FMCW Reflectometry

2.1 Introduction

The centerpiece and workhorse of the research described in this thesis is the optoelectronic swept-frequency laser (SFL)—a feedback system designed around a frequency-agile laser to produce precisely linear optical frequency sweeps (chirps) [1–3]. This system is studied in detail in chapter 3. In the present chapter, by way of introduction, we focus on an application of swept-frequency waveforms, optical frequency-modulated continuous-wave (FMCW) reflectometry, and its use in three-dimensional (3-D) imaging. We examine how chirp characteristics affect application metrics and therefore motivate the choices made in the design of the optoelectronic SFL.

The fundamental challenge of 3-D imaging is ranging—the retrieval of depth information from a scene or a sample. One way to construct a 3-D imaging system is to launch a laser beam along a particular axis, and collect the reflected light, in an effort to determine the depths of all the scatterers encountered by the beam as it propagates. A 3-D image may then be recorded by scanning the beam over the entire object space.

A conceptually simple way to retrieve depth information is to launch optical pulses, and record arrival times of the reflections. Scatterer depth can then be calculated by multiplying the arrival times by the speed of light c. Implementations based on this idea, collectively known as time-of-flight (TOF) systems, have been successfully demonstrated [16, 17]. The depth resolution, also called range resolution or axial

resolution, of TOF methods depends on the system's ability to generate and record temporally narrow optical pulses. A state-of-the-art TOF system therefore requires a costly pulse source, e.g., a mode-locked laser, and a high-bandwidth detector [37]. A detection bandwidth of 1 GHz yields a resolution of $\Delta z \propto c \times (1\text{ ns}) = 30$ cm in free space. Improvement of the resolution to the sub-mm range requires detectors with 100s of GHz of bandwidth, and is prohibitively expensive with current technology.

The technique of frequency-modulated continuous-wave (FMCW) reflectometry, originally developed for radio detection and ranging (radar), can be applied to the optical domain to circumvent the detector bandwidth limit by using a swept-frequency optical waveform. Systems utilizing FMCW reflectometry, also known as swept-source optical coherence tomography (SS-OCT) in the biomedical optics community, are capable of resolutions of a few μm with low detection bandwidths. Moreover, optical FMCW is an interferometric technique in which the measured signal is proportional to the reflected electric field, as opposed to the reflected intensity, as in the TOF case. The signal levels due to a scatterer with reflectivity $R < 1$ are therefore proportional to R and $\sqrt{R}$ in TOF and FMCW systems, respectively. The combination of higher signal levels due to electric field dependence, and lower noise due to low detection bandwidths results in a significantly higher dynamic range and sensitivity of the FMCW system versus a TOF implementation [37,38]. As a result, FMCW reflectometry has found numerous applications, e.g., light detection and ranging (lidar) [18,19], biomedical imaging [20, 21], non-contact profilometry [22, 23] and biometrics [24, 25].

2.1.1 Basic FMCW Analysis and Range Resolution

Let us first examine the problem of recovering single-scatterer depth information using a SFL. For simplicity, we consider a noiseless laser whose frequency changes linearly with time. The normalized electric field at the source, for a single chirp period, is given by

$$e(t) = \text{rect}\left(\frac{t - T/2}{T}\right)\cos\left(\phi_0 + \omega_0 t + \frac{\xi t^2}{2}\right), \tag{2.1}$$

where T is the scan duration, ξ is the slope of the optical chirp, and ϕ_0 and ω_0 are the initial phase and frequency, respectively. The rect function models the finite time-extent of the chirp and is defined by:

$$\text{rect}(x) \equiv \begin{cases} 0, & |x| > 1/2 \\ 1/2, & |x| = 1/2 \\ 1, & |x| < 1/2 \end{cases} \tag{2.2}$$

The instantaneous optical frequency is given by the time derivative of the argument of the cosine in equation (2.1)

$$\omega_{SFL}(t) = \frac{d}{dt}\left(\phi_0 + \omega_0 t + \frac{\xi t^2}{2}\right) = \omega_0 + \xi t \tag{2.3}$$

The total frequency excursion of the source (in Hz) is then given by $B = \xi T/2\pi$. We illuminate a single scatterer with the chirped field, and collect the reflected light. The time evolution of the frequencies of the launched and reflected beams is shown in figure 2.1. Because the chirp is precisely linear, a scatterer with a round-trip time delay τ (and a corresponding displacement $c\tau/2$ from the source) results in constant frequency difference $\xi\tau$ between the launched and reflected waves.

The FMCW technique relies on a measurement of this frequency differences to determine the time delay τ. This is accomplished in a straightforward way by recording the time-dependent interference signal between the launched and reflected waves on a photodetector. An FMCW measurement setup based on a Mach-Zehnder interferometer (MZI) is shown schematically in figure 2.2. Another common implementation

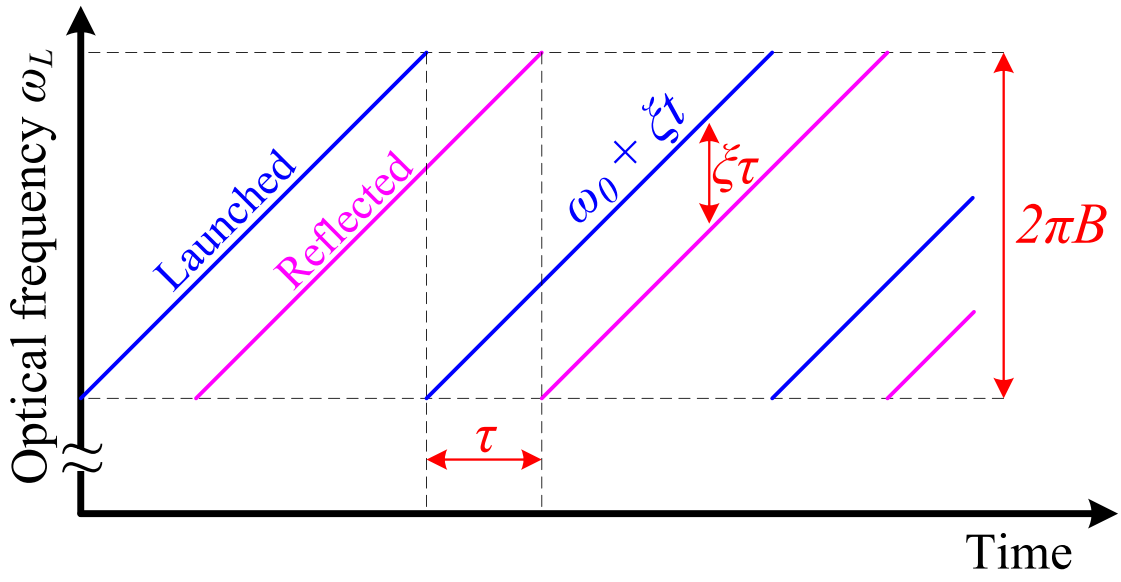

Figure 2.1: Time evolution of the optical frequencies of the launched and reflected waves in a single-scatterer FMCW ranging experiment

is based on a Michelson interferometer, and is shown in figure 2.3. In both implementations, the sum of the electric fields of the launched and reflected waves is incident on a photodetector. It is common to call the launched wave a local or a reference wave, and we will use all three terms interchangeably (hence the reference arm and reference mirror designations in the MZI and Michelson interferometer figures).

The normalized photocurrent is equal to the time-averaged intensity of the incident beam, and is given by

$$\begin{aligned} i(t) &= \left\langle \left| e(t) + \sqrt{R}\, e(t-\tau) \right|^2 \right\rangle_t \\ &= \text{rect}\left(\frac{t - T/2}{T} \right) \left\{ \frac{1+R}{2} + \sqrt{R} \cos\left[(\xi\tau)t + \omega_0 \tau - \frac{\xi\tau^2}{2} \right] \right\}, \end{aligned} \tag{2.4}$$

where R is the target reflectivity, and we have assumed that $\tau << T$. The averaging, denoted by $\langle \cdot \rangle_t$, is done over an interval that is determined by the photodetector response time, and is much longer than an optical cycle, yet much shorter than the period of the cosine in equation (2.4). In the expressions that follow we drop the DC term $(1 + R)/2$ for simplicity. It is convenient to work in the optical frequency

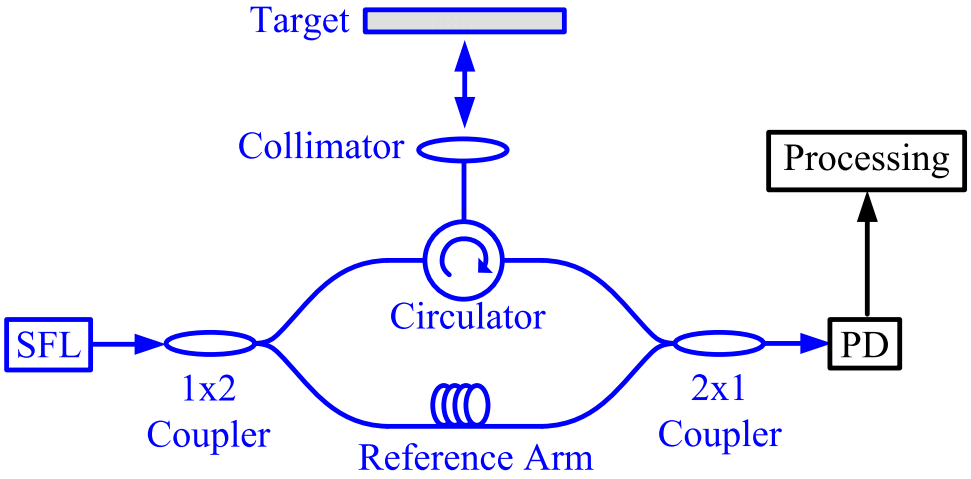

Figure 2.2: Mach-Zehnder interferometer implementation of the FMCW ranging experiment

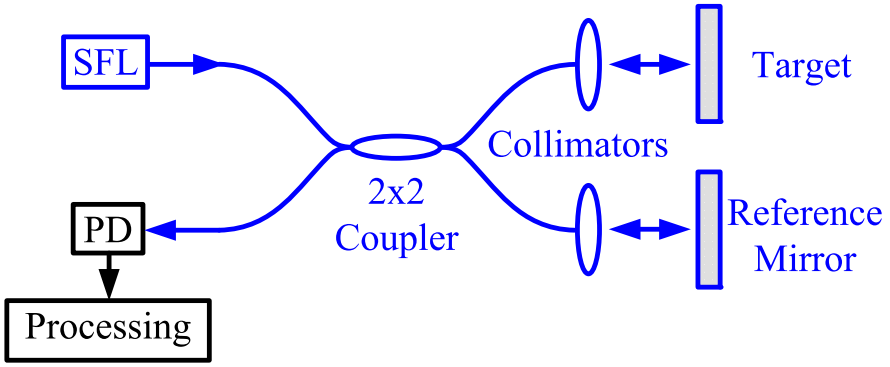

Figure 2.3: Michelson interferometer implementation of the FMCW ranging experiment

domain, so we use equation (2.3) to rewrite the photocurrent as a function of ω_{SFL}.

$$\begin{aligned} y(\omega_{SFL}) &\equiv i\left(\frac{\omega_{SFL}-\omega_0}{\xi}\right) \\ &= \sqrt{R}\,\mathrm{rect}\left(\frac{\omega_{SFL}-\omega_0-\pi B}{2\pi B}\right)\cos\left(\omega_{SFL}\tau-\frac{\xi\tau^2}{2}\right). \end{aligned} \tag{2.5}$$

The delay τ is found by taking the Fourier transform (FT) of $y(\omega_{SFL})$ with respect to the variable ω_{SFL}, which yields a single sinc function centered at the delay τ.

$$Y(\zeta) \equiv \mathcal{F}_{\omega_{SFL}}\{y(\omega_{SFL})\} = \pi B\sqrt{R}\,\exp\left(-j\frac{\xi\tau^2}{2}\right)\exp\left[-j(\zeta-\tau)(\omega_0+\pi B)\right]\mathrm{sinc}\left[\pi B(\zeta-\tau)\right], \tag{2.6}$$

where ζ is the independent variable of the FT of $y(\omega_{SFL})$, and has units of time, and $\mathrm{sinc}(x) = \frac{\sin x}{x}$. Additionally, we only consider positive Fourier frequencies since the signals of interest are purely real, and the FT therefore possesses symmetry about $\zeta = 0$.

A collection of scatterers along the direction of beam propagation arising, for example, from multiple tissue layers in an SS-OCT application, results in a collection of sinusoidal terms in the photodetector current, so that equation (2.6) becomes:

$$Y(\zeta) = \pi B\sum_n \sqrt{R_n}\,\exp\left(-j\frac{\xi\tau_n^2}{2}\right)\exp\left[-j(\zeta-\tau_n)(\omega_0+\pi B)\right]\mathrm{sinc}\left[\pi B(\zeta-\tau_n)\right], \tag{2.7}$$

where τ_n and R_n are the round-trip time delay and the reflectivity of the n-th scatterer. Each scatterer manifests itself as a sinc function positioned at its delay, with a strength determined by its reflectivity. The ζ-domain description is therefore a map of scatterers along the axial direction.

The range resolution is traditionally chosen to correspond to the coordinate of the first null of the sinc function in equation (2.6) [39]. The null occurs at $\zeta = \tau + 1/B$, which corresponds to a free-space axial resolution

$$\Delta z = \frac{c}{2B}. \tag{2.8}$$

The first constraint on the SFL is therefore the chirp bandwidth B—a large optical frequency range is necessary in order to construct a high-resolution imaging system. SS-OCT applications require resolutions below 10 μm in order to resolve tissue structure, and therefore make use of sources with bandwidths exceeding 10 THz.

An additional constraint on the imaging system is the need for precise knowledge of the instantaneous optical frequency as a function of time—it was used in transforming the photocurrent to the ω-domain. In the preceding analysis we have assumed a linear frequency sweep. While chirp linearity is preferred since it simplifies signal processing, it is not strictly necessary. As long as $\omega_{SFL}(t)$ is known precisely, it is still possible to transform the measured signal to the optical frequency domain, and extract the scatterer depth information. Because most SFLs have nonlinear chirps, it is common practice to measure the instantaneous chirp rate in parallel with the measurement using a reference interferometer. A related technique relies on what is called a k-clock—an interferometer that is used to trigger photocurrent sampling at time intervals that correspond to equal steps in optical frequency [20]. The k-clock is therefore a hardware realization of the ω-domain transformation.

While nonlinear chirps can be dealt with, they require faster electronics in order to acquire the higher frequency photocurrents associated with a nonuniform chirp rate. The optoelectronic SFL described in chapter 3 uses active feedback to enable precise control of the instantaneous optical frequency. As a result, the chirp can be programmed to be exactly linear in advance, allowing the use of a lower detection bandwidth, and hence decreasing electronic noise in an FMCW measurement.

2.1.2 Balanced Detection and RIN

In the preceding FMCW analysis we have simplified the expressions by intentionally leaving out DC contributions to the photocurrent. This simplification, while valid in an ideal noiseless laser, needs further justification in a practical measurement. The output intensity of laser systems varies due to external causes such as temperature and acoustic fluctuations, and also due to spontaneous emission into the lasing mode [40].

These intensity fluctuations scale with the nominal output intensity and are termed relative intensity noise (RIN). In a laser with RIN, the terms which give rise to the DC components of equation (2.4), also give rise to a noise component that we call $n(t)$. Equation (2.4) is therefore modified to

$$i(t) = \text{rect}\left(\frac{t - T/2}{T}\right)\left\{\left(\frac{1+R}{2} + n(t)\right) + \sqrt{R}\cos\left[(\xi\tau)t + \omega_0\tau - \frac{\xi\tau^2}{2}\right]\right\}. \quad (2.9)$$

The term $n(t)$ is a random variable whose statistics depend on the environmental conditions, the type of laser used in the measurement, and on the frequency response of the detection circuit. While the DC terms are readily filtered out, $n(t)$ is broadband and can corrupt the signal. This corruption is particularly important when the scatterers are weak and the signal level is low.

Balanced detection is a standard way to null the contribution of the DC terms and RIN. It relies on the use of a 2x2 coupler and a pair of photodetectors to measure the intensities of both the sum and the difference of the reference and reflected electric fields. Mach-Zehnder interferometer (MZI) and Michelson interferometer balanced FMCW implementations are shown in figure 2.4 and figure 2.5. These measurements produce pairs of photocurrents

$$i_{\pm}(t) = \text{rect}\left(\frac{t - T/2}{T}\right)\left\{\left(\frac{1+R}{2} + n(t)\right) \pm \sqrt{R}\cos\left[(\xi\tau)t + \omega_0\tau - \frac{\xi\tau^2}{2}\right]\right\}. \quad (2.10)$$

Balanced processing consists of averaging the two photocurrents, yielding

$$i_{\text{diff}}(t) \equiv \frac{i_+(t) - i_-(t)}{2} = \text{rect}\left(\frac{t - T/2}{T}\right)\sqrt{R}\cos\left[(\xi\tau)t + \omega_0\tau - \frac{\xi\tau^2}{2}\right]. \quad (2.11)$$

The DC and RIN terms are nulled in the subtraction, justifying the simplification made earlier. However, small gain differences in the photodetector circuitry, as well as slight asymmetries in the splitting ratio of the 2x2 coupler, result in a small amount of residual DC and RIN being present in the balanced photocurrent. This places a further constraint on the SFL—it is desirable that the laser possess a minimal amount of RIN so as to limit the amount of noise left over after balancing, and therefore

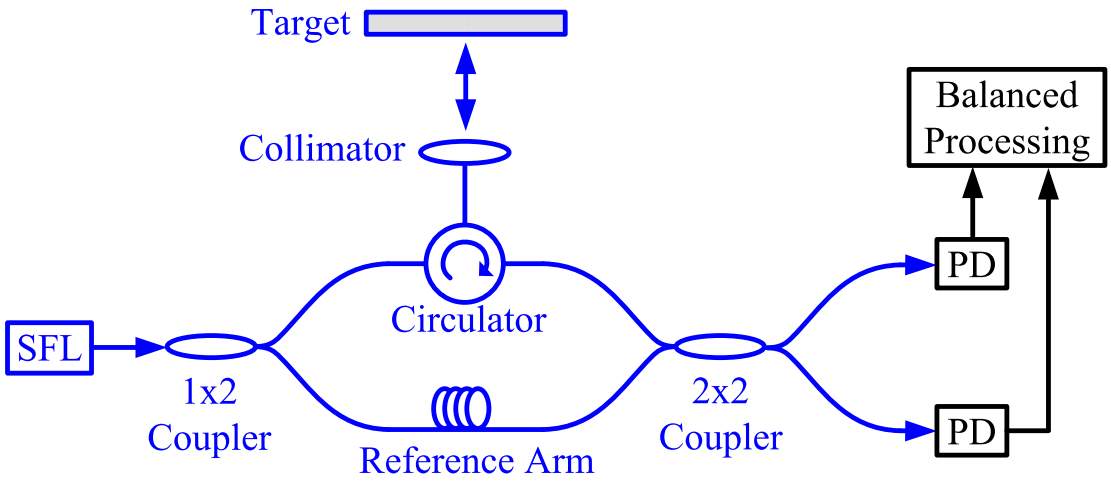

Figure 2.4: A balanced Mach-Zehnder interferometer implementation of the FMCW ranging experiment

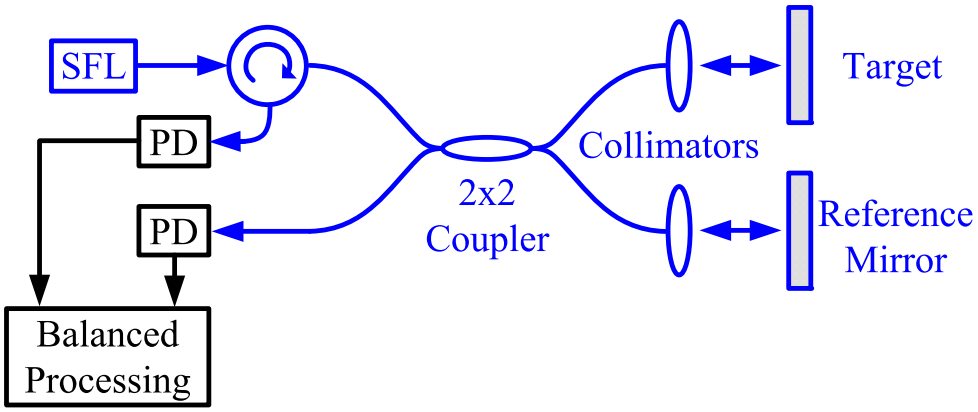

Figure 2.5: A balanced Michelson interferometer implementation of the FMCW ranging experiment

enhance the measurement dynamic range.

2.1.3 Effects of Phase Noise on the FMCW Measurement

So far we have assumed an SFL with a perfectly sinusoidal electric field. Practical lasers, however, exhibit phase and frequency noise. These fluctuations arise due to both external causes, such as thermal fluctuations, as well as due to spontaneous emission into the lasing mode [40]. These phenomena are responsible for a broadening of the spectrum of the electric field of a laser. In this section we analyze the effects of phase noise on the FMCW measurement. We begin by deriving the linewidth $\Delta\omega$ of single-frequency emission with phase noise. We then modify the FMCW equations to account for phase noise, derive its effects on fringe visibility, and define the notion of coherence time. To further quantify the effects of phase noise, we calculate the FMCW photocurrent spectrum. It will turn out that phase noise degrades the signal-to-noise ratio (SNR) with increasing target delay, putting a limit on the maximum range that can be reliably measured. We conclude by deriving statistical properties of the measurement accuracy, which help quantify system performance in a single-scatterer application (for example, profilometry).

2.1.3.1 Statistics and Notation

We first review some useful statistical results and introduce notation. For a wide-sense stationary random process $x(t)$, we denote its autocorrelation function by $\mathcal{R}_x$:

$$\mathcal{R}_x(u) = \mathcal{E}\left[x(t)x(t-u)\right], \tag{2.12}$$

where $\mathcal{E}[\cdot]$ is the statistical expectation value. For an ergodic random process, the expectation can be replaced by an average over all time, giving:

$$\mathcal{R}_x(u) = \left\langle x(t)x(t-u)\right\rangle_t, \tag{2.13}$$

By the Wiener–Khinchin theorem, the power spectral density (PSD) $\mathcal{S}_x(\omega)$ and autocorrelation $\mathcal{R}_x(u)$ are FT pairs.

$$\mathcal{S}_x(\omega) = \mathcal{F}_u\left[\mathcal{R}_x(u)\right] = \int_{-\infty}^{\infty} \mathcal{R}_x(u) e^{-i\omega u} du, \tag{2.14}$$

where $\mathcal{F}_u[\cdot]$ is the Fourier transform with respect to the variable u. We denote the variance of $x(t)$ by σ_x^2. For an ergodic process, the variance may be calculated in the time domain:

$$\sigma_x^2 = \left\langle x(t)^2 \right\rangle_t - \left\langle x(t) \right\rangle_t^2. \tag{2.15}$$

Alternatively, it may be calculated by integrating the PSD:

$$\sigma_x^2 = \frac{1}{2\pi} \int_{-\infty}^{\infty} \mathcal{S}_x(\omega) d\omega. \tag{2.16}$$

2.1.3.2 Linewidth of Single-Frequency Emission

We first derive a standard model for the spontaneous emission linewidth of a single-frequency laser [41]. The electric field is given by

$$e(t) = \cos\left[\omega_0 t + \phi_n(t)\right], \tag{2.17}$$

where $\phi_n(t)$ is a zero-mean stationary phase noise term. Plugging this expression into equation (2.13), we find the autocorrelation.

$$\begin{aligned} \mathcal{R}_e(u) &= \left\langle \cos\left[\omega_0 t + \phi_n(t)\right] \cos\left[\omega_0 (t-u) + \phi_n(t-u)\right] \right\rangle_t \\ &= \frac{1}{2} \left\langle \cos\left[\omega_0 u + \Delta\phi_n(t,u)\right] \right\rangle_t + \cancel{\frac{1}{2} \left\langle \cos\left[2\omega_0 t - \omega_0 u + \phi_n(t) + \phi_n(t-u)\right] \right\rangle_t}, \end{aligned} \tag{2.18}$$

where the sum term is crossed out because it averages out to zero. $\Delta\phi_n(t,u)$ is the accumulated phase error during time u, defined by

$$\Delta\phi_n(t,u) \equiv \phi_n(t) - \phi_n(t-u), \tag{2.19}$$

and is the result of a large number of independent spontaneous emission events. By the central limit theorem, $\Delta\phi_n(t,u)$ must be a zero-mean Gaussian random variable. The following identities therefore apply:

$$\langle \cos\left[\Delta\phi_n(t,u)\right]\rangle_t = \exp\left[-\frac{\sigma^2_{\Delta\phi_n}(u)}{2}\right], \text{ and } \langle \sin\left[\Delta\phi_n(t,u)\right]\rangle_t = 0. \tag{2.20}$$

So, equation (2.18) simplifies to

$$\mathcal{R}_e(u) = \frac{1}{2}\cos(\omega_0 u)\exp\left[-\frac{\sigma^2_{\Delta\phi_n}(u)}{2}\right]. \tag{2.21}$$

Taking the FT of equation (2.21), we find the spectrum of the electric field,

$$\mathcal{S}_e(\omega) = \frac{1}{4}\left[S_e^{\circ}(\omega-\omega_0) + S_e^{\circ}(\omega+\omega_0)\right], \tag{2.22}$$

where $S_e^{\circ}(\omega)$ is the baseband spectrum given by

$$S_e^{\circ}(\omega) = \mathcal{F}_u\left\{\exp\left[-\frac{\sigma^2_{\Delta\phi_n}(u)}{2}\right]\right\}. \tag{2.23}$$

To determine the emission lineshape we first consider the variance of the accumulated phase error. We start by expressing the autocorrelation of $\Delta\phi_n(t,u)$ in terms of the autocorrelation of $\phi_n(t)$. Using equation (2.13) and equation (2.19),

$$\mathcal{R}_{\Delta\phi_n}(s,u) = \langle \Delta\phi_n(t,u)\Delta\phi_n(t-s,u)\rangle_t = 2\mathcal{R}_{\phi_n}(s) - \mathcal{R}_{\phi_n}(s+u) - \mathcal{R}_{\phi_n}(s-u). \tag{2.24}$$

The PSD is given by

$$\begin{aligned}\mathcal{S}_{\Delta\phi_n}(\omega,u) &= \mathcal{F}_s\left[\mathcal{R}_{\Delta\phi_n}(s,u)\right] = \mathcal{S}_{\phi_n}(\omega)\left(2 + e^{j\omega u} + e^{-j\omega u}\right) \\ &= 4\mathcal{S}_{\phi_n}(\omega)\sin^2(\omega u) = 4u^2\mathcal{S}_{\dot{\phi}_n}(\omega)\mathrm{sinc}^2(\omega u),\end{aligned} \tag{2.25}$$

where $\mathcal{S}_{\dot{\phi}_n}(\omega) = \omega^2\mathcal{S}_{\phi_n}(\omega)$ is the spectrum of the frequency noise $\dot{\phi}_n$. Spontaneous emission into the lasing mode gives rise to a flat frequency noise spectrum [40, 42],

and we therefore assign a constant value to $\mathcal{S}_{\dot{\phi}_n}(\omega)$,

$$\mathcal{S}_{\dot{\phi}_n}(\omega) \equiv \Delta\omega. \tag{2.26}$$

We plug equation (2.25) and equation (2.26) into equation (2.16) to calculate the variance of the accumulated phase error.

$$\begin{aligned}\sigma^2_{\Delta\phi_n}(u) &= \frac{1}{2\pi}\int_{-\infty}^{\infty} \mathcal{S}_{\Delta\phi_n}(\omega, u)d\omega \\ &= \frac{1}{2\pi}\int_{-\infty}^{\infty} 4u^2\Delta\omega\ \mathrm{sinc}^2(\omega u)d\omega \\ &= |u|\Delta\omega.\end{aligned} \tag{2.27}$$

Plugging this result into equation (2.23), we obtain the baseband spectrum of the electric field.

$$\begin{aligned}S_e^{\circ}(\omega) &= \mathcal{F}_u\left\{\exp\left[-\frac{\sigma^2_{\Delta\phi_n}(u)}{2}\right]\right\} = \mathcal{F}_u\left[\exp\left(-|u|\frac{\Delta\omega}{2}\right)\right] \\ &= \frac{\Delta\omega}{(\Delta\omega/2)^2 + \omega^2}.\end{aligned} \tag{2.28}$$

The presence of phase noise broadens the baseband spectrum from a delta function to a Lorentzian function with a full width at half maximum (FWHM), or linewidth, of $\Delta\omega$.

To summarize, a flat frequency noise spectrum with a value of $\Delta\omega$ corresponds to a linewidth of $\Delta\omega$.

$$\mathcal{S}_{\dot{\phi}_n}(\omega) = \Delta\omega \iff \text{linewidth } \Delta\omega \text{ (rad/s)} \tag{2.29}$$

So far we have been using angular frequency units (rad/s) for both frequency noise and linewidth. Ordinary frequency units (Hz) are often used, so we convert the relation in equation (2.29) to

$$\mathcal{S}_{\dot{\frac{\phi_n}{2\pi}}}(\nu) = \frac{1}{(2\pi)^2}\mathcal{S}_{\dot{\phi}_n}(2\pi\nu) = \frac{\Delta\nu}{2\pi} \iff \text{linewidth } \Delta\nu = \frac{\Delta\omega}{2\pi} \text{ (Hz)}, \tag{2.30}$$

where $\nu = \omega/(2\pi)$ is the Fourier frequency in Hz. In practice, there are other noise sources that give rise to a $1/f$ behavior of the frequency noise spectrum. It has been shown that such noise sources generate a Gaussian lineshape [43].

As an exercise, we numerically verify equation (2.30) using a Monte Carlo simulation. We model a flat angular frequency noise spectrum by drawing samples from a zero-mean Gaussian distribution. These frequency noise samples are integrated in time, and the cosine of the resultant phase noise is calculated. The PSD of this signal therefore corresponds to half the baseband spectrum of equation (2.28). Each iteration of this procedure is performed over a finite time T, and therefore yields only an *estimate* of the true PSD. If the angular frequency resolution $2\pi/T$ is much smaller than the angular linewidth $\Delta\omega$, the mean of this estimate, over many iterations, will converge to equation (2.28) [44].

Estimates of baseband electric field spectra corresponding to $\mathcal{S}_{\dot{\phi}_n}(\omega) = 2\pi(1\text{ MHz})$ are shown in blue in figure 2.6. As the number of iterations N used in the calculation is increased, the simulated PSD converges to the true PSD of equation (2.28), shown in red. Simulated frequency noise spectra and corresponding baseband lineshapes for three different values of $\Delta\omega$ are plotted in figure 2.7, illustrating the relation of equation (2.29).

2.1.3.3 Fringe Visibility in an FMCW Measurement

We continue or analysis by modifying the chirped electric field in equation (2.1) to include phase noise,

$$e(t) = \text{rect}\left(\frac{t - T/2}{T}\right)\cos\left(\phi_0 + \omega_0 t + \frac{\xi t^2}{2} + \phi_n(t)\right), \tag{2.31}$$

and assume a perfect reflector ($R = 1$). The photocurrent is therefore given by

$$i(t) = \text{rect}\left(\frac{t - T/2}{T}\right)\left\{1 + \cos\left[(\xi\tau)t + \omega_0\tau - \frac{\xi\tau^2}{2} + \Delta\phi_n(t,\tau)\right]\right\}, \tag{2.32}$$

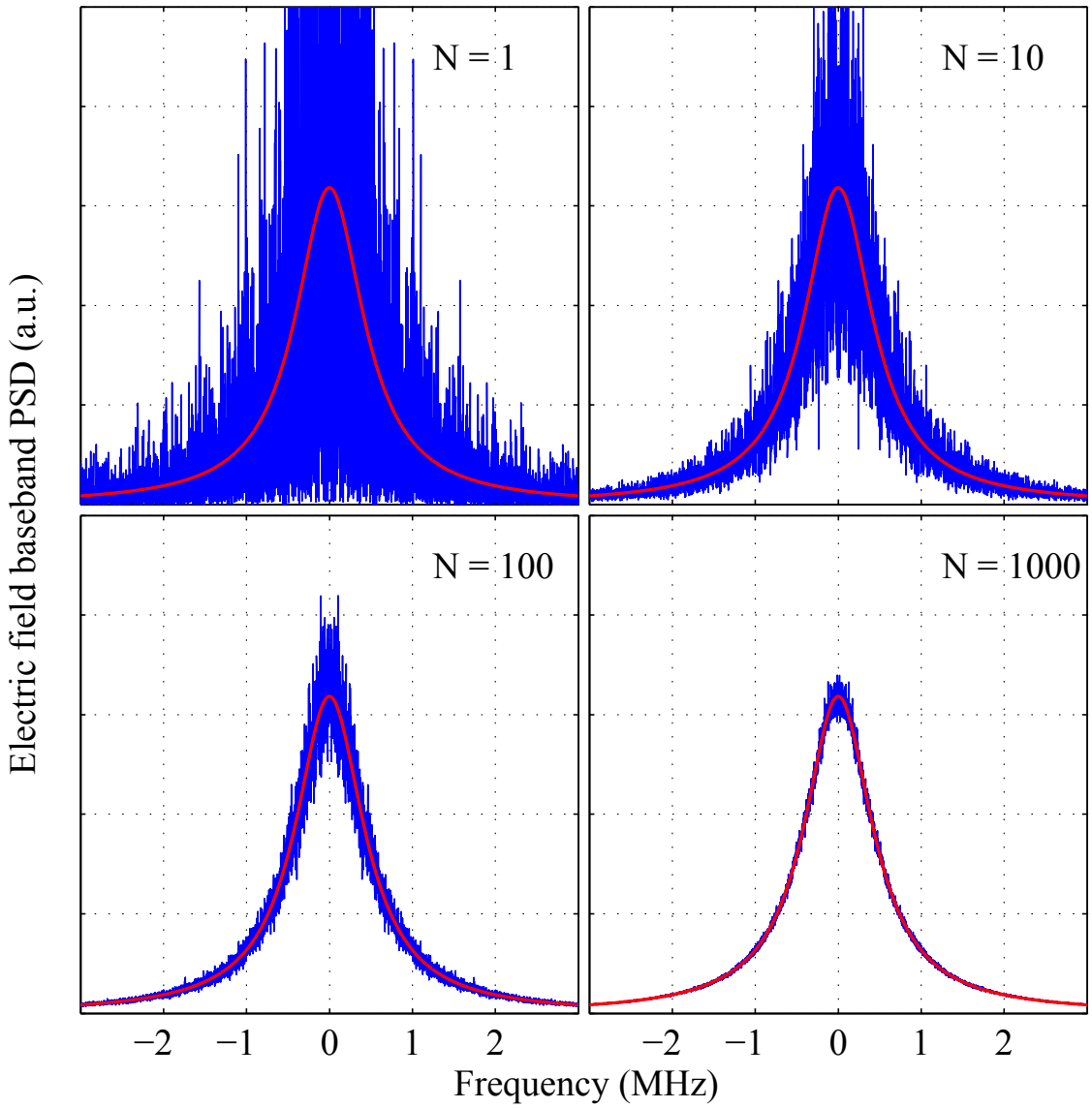

Figure 2.6: Convergence of the Monte Carlo simulation of the baseband electric field spectrum (blue) to the theoretical expression (red). The angular linewidth is $\Delta\omega = 2\pi(1\text{ MHz})$. N is the number of iterations used in calculating the PSD estimate.

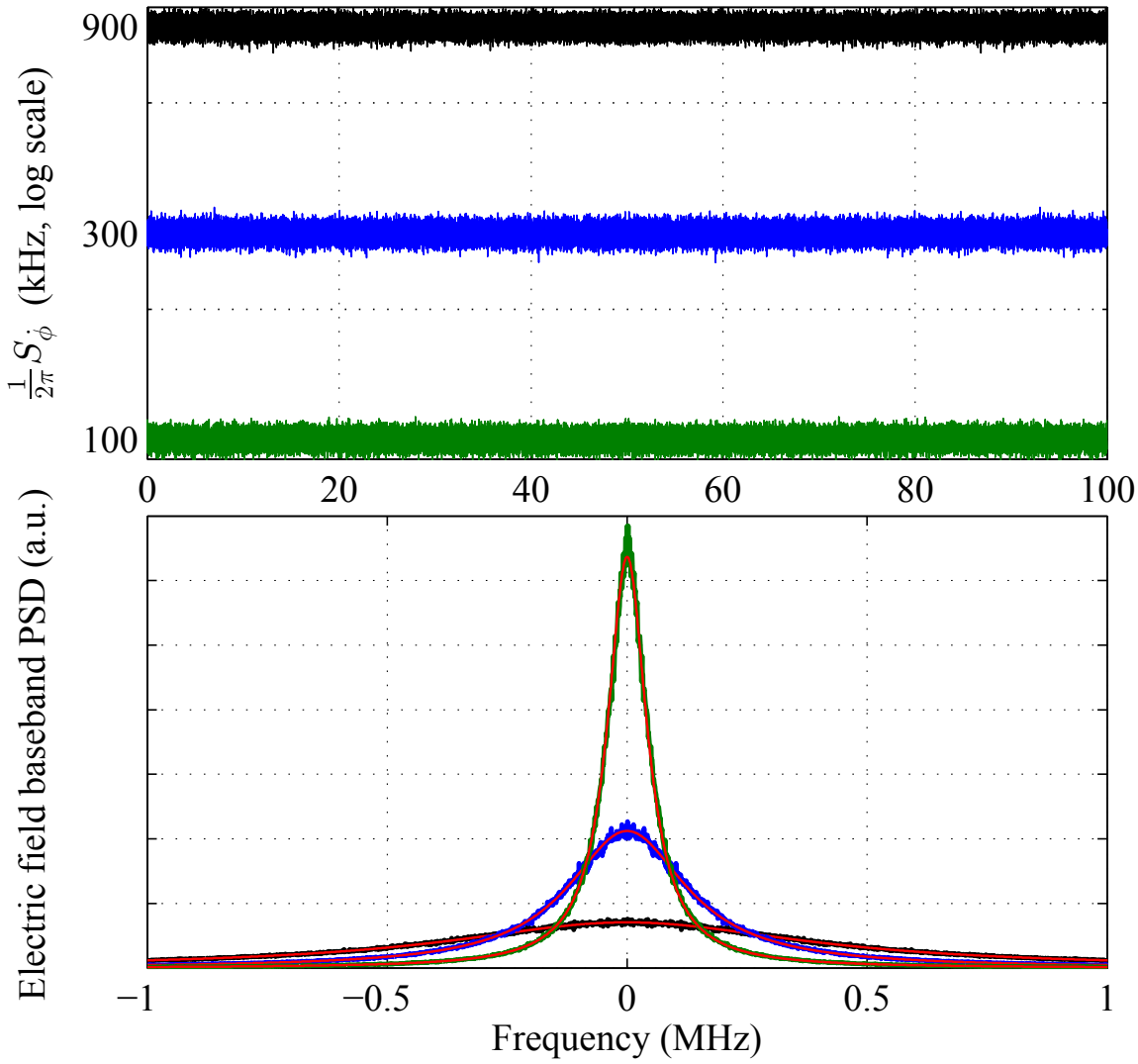

Figure 2.7: Normalized frequency noise spectra (top panel) and corresponding baseband electric field spectra (bottom panel) for $\Delta\omega = 2\pi(900\text{ kHz})$ (black), $2\pi(300\text{ kHz})$ (blue), and $2\pi(100\text{ kHz})$ (green). The spectra are averaged over N=1000 iterations. The red curves are plots of the theoretical lineshape for the three values of $\Delta\omega$.

where $\Delta\phi_n(t,\tau)$ is the familiar accumulated phase error during time τ. In the noiseless case, the oscillations (fringes) in the photocurrent extend from 0 to 2. The presence of phase noise will add jitter to the locations of the peaks and troughs. The amplitude of the fringes, averaged over many scans, is therefore expected to decrease with increasing phase noise. To quantify this effect, we define the fringe visibility

$$V \equiv \frac{i_{max} - i_{min}}{i_{max} + i_{min}}, \tag{2.33}$$

where i_{max} and i_{min} are the photocurrent values at the peaks and troughs, averaged over many scans. The visibility takes on a value of 1 in the noiseless case, and goes to zero as the amount of noise increases. Using the identities in equation (2.20), we write down expressions for the maximum and minimum currents,

$$\begin{aligned} i_{max} &= 1 + \exp\left[-\frac{\sigma^2_{\Delta\phi_n}(\tau)}{2}\right], \text{ and} \\ i_{min} &= 1 - \exp\left[-\frac{\sigma^2_{\Delta\phi_n}(\tau)}{2}\right]. \end{aligned} \tag{2.34}$$

Plugging in equation (2.27) and equation (2.34) into equation (2.33), we arrive at an expression for the phase-noise-limited visibility [45],

$$V = \exp\left(-|\tau|\frac{\Delta\omega}{2}\right) = \exp\left(-\frac{|\tau|}{\tau_c}\right), \tag{2.35}$$

where

$$\tau_c \equiv \frac{2}{\Delta\omega} = \frac{1}{\pi\Delta\nu} \tag{2.36}$$

is the coherence time of the SFL. For delays much shorter than the coherence time, the visibility decreases linearly with τ. Once τ is comparable to τ_c, the visibility drops exponentially. The coherence time is therefore a measure of the longest range that can be acquired by an FMCW system.

2.1.3.4 Spectrum of the FMCW Photocurrent and the SNR

The signal-to-noise ratio (SNR) is more useful in quantifying the effect of phase noise than the visibility. To determine the SNR we must first calculate the photocurrent spectrum. We assume a balanced detector and disregard, for now, the rect function that models the finite chirp bandwidth of the SFL. The photocurrent expression becomes

$$i(t) = \sqrt{R}\cos\left[(\xi\tau)t + \omega_0\tau - \frac{\xi\tau^2}{2} + \Delta\phi_n(t,\tau)\right]. \tag{2.37}$$

Plugging this expression into equation (2.13), we find the autocorrelation,

$$\begin{aligned}\mathcal{R}_i(u) &= \frac{R}{2}\left\langle\cos\left[(\xi\tau)u + \Delta\phi_n(t,\tau) - \Delta\phi_n(t-u,\tau)\right]\right\rangle_t \\ &= \frac{R}{2}\left\langle\cos\left[(\xi\tau)u + \theta(t,\tau,u)\right]\right\rangle_t \\ &= \frac{R}{2}\cos\left[(\xi\tau)u\right]\exp\left[-\frac{\sigma_\theta^2(\tau,u)}{2}\right],\end{aligned} \tag{2.38}$$

where

$$\theta(t,\tau,u) \equiv \Delta\phi_n(t,\tau) - \Delta\phi_n(t-u,\tau), \tag{2.39}$$

and we have assumed that $\theta(t,\tau,u)$ possesses Gaussian statistics. Taking the FT of equation (2.38), we find the spectrum of the photocurrent.

$$\mathcal{S}_i(\omega) = \frac{1}{4}\left[S_i^\circ(\omega-\xi\tau) + S_i^\circ(\omega+\xi\tau)\right], \tag{2.40}$$

where $S_i^\circ(\omega)$ is the baseband spectrum given by

$$S_i^\circ(\omega) = \mathcal{F}_u\left\{\exp\left[-\frac{\sigma_{\theta(\tau,u)}^2}{2}\right]\right\}. \tag{2.41}$$

To find the baseband spectrum and the SNR we need to calculate the variance of $\theta(t,\tau,u)$. First we derive a useful identity. Let us write down the variance of $\Delta\phi_n(t,u)$,

as it is defined in equation (2.15),

$$\begin{aligned}\sigma^2_{\Delta\phi_n}(u) &= \left\langle [\phi_n(t) - \phi_n(t-u)]^2 \right\rangle_t \\ &= 2\sigma^2_{\phi_n} - 2\left\langle \phi_n(t)\phi_n(t-u) \right\rangle_t .\end{aligned} \tag{2.42}$$

This gives us an expression for the autocorrelation of $\phi_n(t)$,

$$\mathcal{R}_\phi(u) = \left\langle \phi_n(t)\phi_n(t-u) \right\rangle_t = \sigma^2_{\phi_n} - \frac{\sigma^2_{\Delta\phi_n}(u)}{2}. \tag{2.43}$$

We plug this result into equation (2.24),

$$\begin{aligned}\mathcal{R}_{\Delta\phi_n}(s,u) &= 2\mathcal{R}_{\phi_n}(s) - \mathcal{R}_{\phi_n}(s+u) - \mathcal{R}_{\phi_n}(s-u) \\ &= \frac{\sigma^2_{\Delta\phi_n}(s+u)}{2} + \frac{\sigma^2_{\Delta\phi_n}(s-u)}{2} - \sigma^2_{\Delta\phi_n}(s)\end{aligned} . \tag{2.44}$$

We are now in a position to calculate the variance of $\theta(t,\tau,u)$. Beginning with the definition in equation (2.15),

$$\begin{aligned}\sigma^2_\theta(\tau,u) &= \left\langle [\Delta\phi_n(t,\tau) - \Delta\phi_n(t-u,\tau)]^2 \right\rangle_t \\ &= \left\langle \Delta\phi_n(t,\tau)^2 + \Delta\phi_n(t-u,\tau)^2 - 2\Delta\phi_n(t,\tau)\Delta\phi_n(t-u,\tau) \right\rangle_t \\ &= 2\sigma^2_{\Delta\phi_n}(\tau) - 2\mathcal{R}_{\Delta\phi_n}(u,\tau).\end{aligned} \tag{2.45}$$

Plugging in equation (2.44), we arrive at

$$\sigma^2_\theta(\tau,u) = 2\sigma^2_{\Delta\phi_n}(\tau) + 2\sigma^2_{\Delta\phi_n}(u) - \sigma^2_{\Delta\phi_n}(u+\tau) - \sigma^2_{\Delta\phi_n}(u-\tau). \tag{2.46}$$

Using the result of equation (2.27), we write down a final expression for the variance of $\theta(t,\tau,u)$,

$$\begin{aligned}\sigma^2_\theta(\tau,u) &= \Delta\omega\left(2\tau + 2|u| - |u-\tau| - |u+\tau|\right) \\ &= \begin{cases} \dfrac{4|u|}{\tau_c} & |u| \le \tau, \\ \dfrac{4\tau}{\tau_c} & |u| > \tau. \end{cases}\end{aligned} \tag{2.47}$$

The baseband photocurrent spectrum is found by plugging equation (2.47) into equation (2.41), yielding [46, 47]

$$\begin{aligned} S_i^{\circ}(\omega) &= \mathcal{F}_u \left\{ \exp\left[-\frac{\sigma^2_{\theta(\tau,u)}}{2} \right] \right\} \\ &= 2\pi\delta(\omega) e^{-\frac{2\tau}{\tau_c}} + \frac{\tau_c}{1 + \left(\frac{\omega\tau_c}{2}\right)^2} \left\{ 1 - e^{-\frac{2\tau}{\tau_c}} \left[\cos(\omega\tau) + \frac{2}{\omega\tau_c} \sin(\omega\tau) \right] \right\}. \end{aligned} \tag{2.48}$$

This expression has two terms—the delta function that represents the beat signal due to an interference of the reference and reflected beams, and the noise pedestal that arises as a result of the finite coherence time of the chirped beam. Each FMCW measurement is performed over a finite time T, and its PSD is therefore only an estimate of equation (2.48). The expected spectrum is given by the convolution of equation (2.48) and the PSD of the rect function that accompanies the electric field of equation (2.31) [44],

$$\begin{aligned} S_i^{\circ}(\omega, T) &= \frac{1}{2\pi} S_i^{\circ}(\omega) \star \left[T \mathrm{sinc}^2\left(\frac{\mathrm{T}\omega}{2} \right) \right] \\ &= T \mathrm{sinc}^2\left(\frac{\mathrm{T}\omega}{2} \right) e^{-\frac{2\tau}{\tau_c}} + \frac{\tau_c}{1 + \left(\frac{\omega\tau_c}{2}\right)^2} \left\{ 1 - e^{-\frac{2\tau}{\tau_c}} \left[\cos(\omega\tau) + \frac{2}{\omega\tau_c} \sin(\omega\tau) \right] \right\}. \end{aligned} \tag{2.49}$$

In performing this convolution we have assumed that the scan time is the slowest time scale in the model, i.e., $T \gg \tau$ and $T \gg \tau_c$, so that the sinc-squared PSD of the rect function effectively acts as a delta function when convolved with the spectrum of the noise pedestal. Plots of equation (2.49) for four different values of τ/τ_c are shown in figure 2.8. The scan time is $T = 1$ ms and the coherence time is $\tau_c = 1$ μs. The spectra are normalized to the level of the noise at $\omega = 0$. In the coherent regime, i.e., $\tau \ll \tau_c$, the PSD comprises a sinc-squared signal peak and a broad noise pedestal with oscillations. The period of these oscillations is given by $2\pi/\tau$. As the delay is increased, the signal peak shrinks, and the noise pedestal grows, until we obtain a Lorentzian profile with a FWHM of $2\Delta\omega$. This is what we expect for a beat spectrum of two uncorrelated beams with a linewidth of $\Delta\omega$ each.

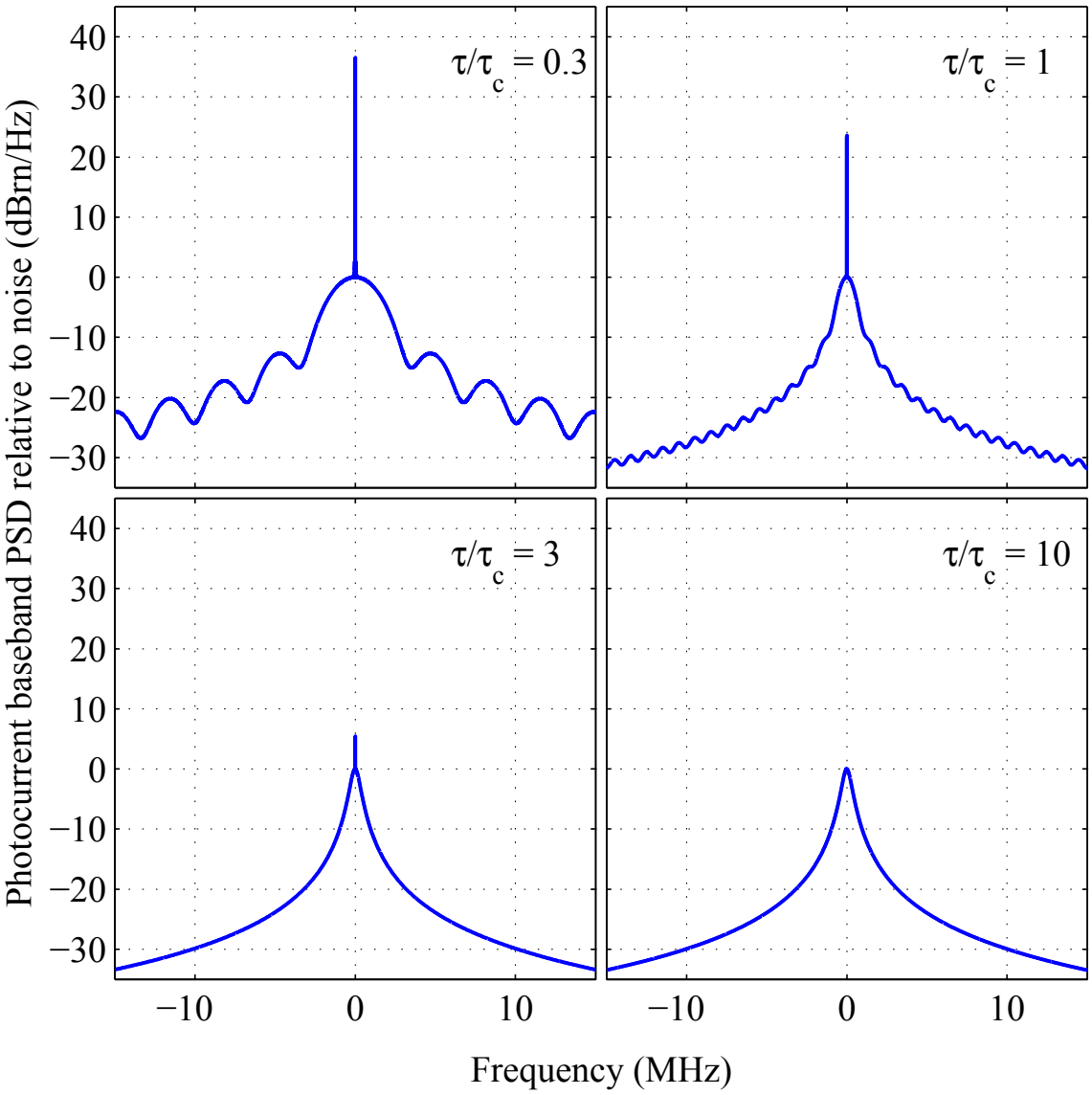

Figure 2.8: Baseband FMCW photocurrent spectra for four different values of τ/τ_c, normalized to zero-frequency noise levels. The scan time is $T = 1$ ms and the coherence time is $\tau_c = 1$ μs.

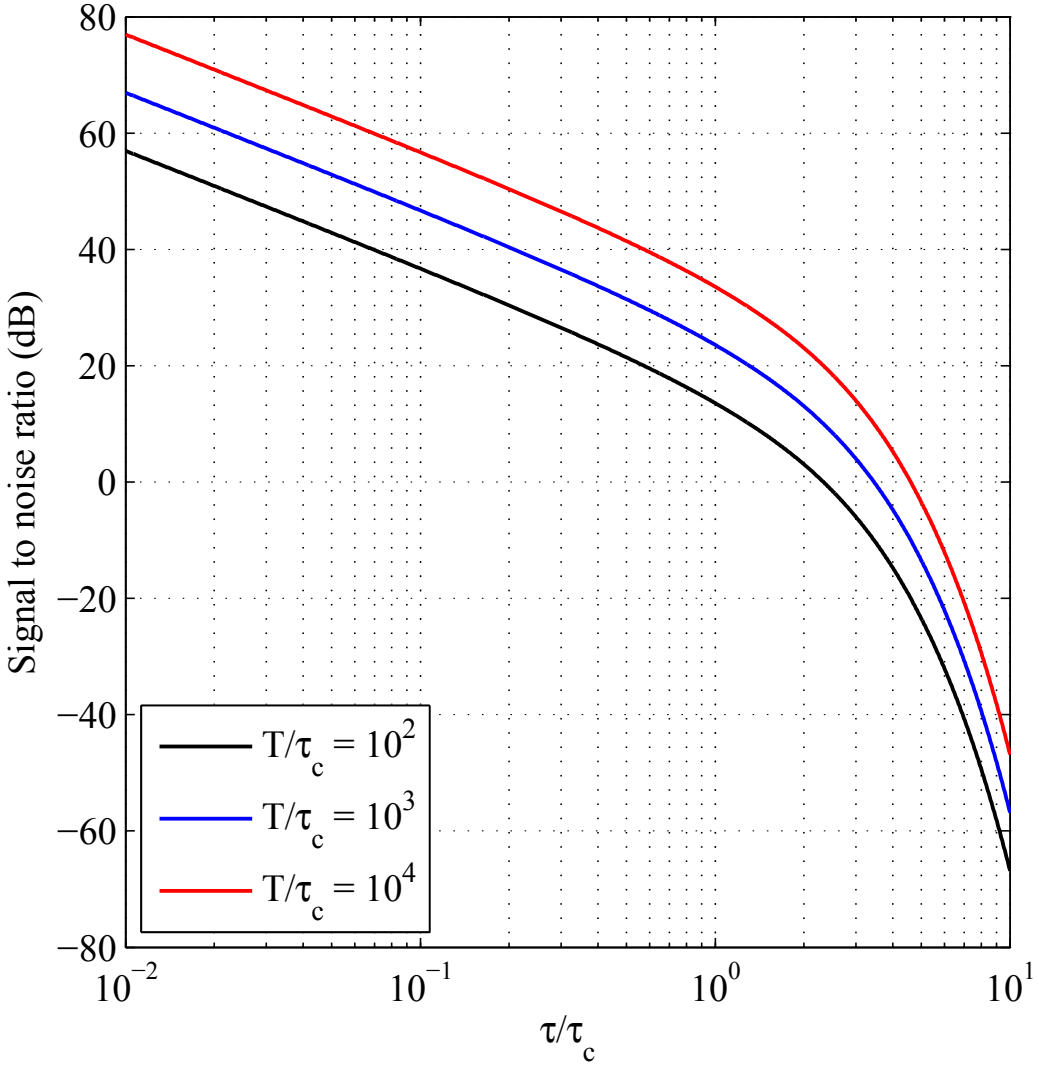

Figure 2.9: FMCW SNR as a function of τ/τ_c for three different values of T/τ_c

The SNR is readily calculated from equation (2.49), and is given in decibel units by

$$\mathrm{SNR}_{\mathrm{dB}} = 10\log_{10}\left[\frac{T}{\tau_i} \times \frac{1}{e^{2\tau/\tau_c} - \left(1 + \frac{2\tau}{\tau_c}\right)}\right]. \tag{2.50}$$

A plot of the SNR versus τ/τ_c is shown in figure 2.9 for three different values of T/τ_c. In the coherent regime, the SNR decreases at 20 dB/decade with τ/τ_c, and drops sharply for $\tau > \tau_c$. This is consistent with the rapid decrease in visibility for delays longer than the coherence time, as predicted by equation (2.35). As the current analysis shows, the visibility is not the full story—even low fringe visibilities can result in a decent SNR, provided that the scan time T is long enough.

2.1.3.5 Phase-Noise-Limited Accuracy

The axial resolution of an FMCW system, $\Delta z = c/2B$, quantifies its ability to tell apart closely-spaced scatterers. If we assume that the beam only encounters a single scatterer, as it would in a profilometry application, then the relevant system metric is the accuracy—the deviation of the measured target delay τ^m from the true target delay τ. We briefly consider statistical properties of the accuracy using the phase noise model developed above.

The instantaneous photocurrent frequency in a single-scatterer FMCW experiment is given by a derivative of the cosine phase in equation (2.37),

$$\omega_{PD}(t) = \xi\tau + \frac{d}{dt}\Delta\phi_n(t,\tau). \tag{2.51}$$

The target delay is calculated from an average of the photocurrent frequency over the scan time T,

$$\xi\tau^m = \frac{1}{T}\int_0^T \omega_{PD}(t) = \xi\tau + \frac{\Delta\phi_n(T,\tau) - \Delta\phi_n(0,\tau)}{T}. \tag{2.52}$$

The accuracy is therefore given by

$$\delta\tau \equiv \tau^m - \tau = \frac{\Delta\phi_n(T,\tau) - \Delta\phi_n(0,\tau)}{B}. \tag{2.53}$$

The accuracy of a single measurement is a zero-mean random process with standard deviation

$$\sigma_{\delta\tau} = \frac{1}{B}\sqrt{\frac{4\tau}{\tau_c}}, \tag{2.54}$$

where we have used equation (2.39) and equation (2.47). Likewise, the depth accuracy δz is characterized by the standard deviation

$$\sigma_{\delta z} = \frac{c}{2B}\sqrt{\frac{4\tau}{\tau_c}} = \Delta z\sqrt{\frac{4\tau}{\tau_c}}. \tag{2.55}$$

Equation (2.55) shows that by operating in the sub-coherent regime, $\tau \ll \tau_c$, it is possible to measure spatial features on a scale that is much finer than the axial resolution. We come back to this idea in section 3.5.2, where we are able to record surface variations on a scale of a few tens of microns using an FMCW system with an axial resolution of 300 μm.

2.1.4 Summary

We have introduced the technique of optical frequency-modulated continuous-wave reflectometry and outlined its advantages over TOF ranging in 3-D imaging applications. We have derived the dependence of axial resolution on the chirp bandwidth and introduced balanced detection as a way to mitigate intensity noise. We have shown that SFL linewidth puts an upper limit on the target range, introduced system performance metrics, and derived the dependence of these metrics on the SFL coherence length, target delay, and scan time.

An ideal SFL will possess a narrow linewidth, linear frequency tuning, high chirp bandwidth, and a low RIN. The semiconductor laser (SCL)-based optoelectronic SFL attains these qualities without moving parts, and is studied in detail in chapter 3.

Chapter 3

The Optoelectronic Swept-Frequency Laser

3.1 Introduction

In this chapter we study the optoelectronic swept-frequency laser (SFL)—a feedback system that enables closed-loop control over the instantaneous optical frequency of a chirped semiconductor laser (SCL). Precisely linear frequency sweeps are of particular interest because of their applications in optical frequency-modulated continuous-wave (FMCW) reflectometry and 3-D imaging, as described in chapter 2. The SFL is a key component of an FMCW system since its characteristics directly affects important performance metrics. Specifically, the axial resolution and the maximum range are inversely proportional to the laser frequency tuning range and linewidth, respectively.

Mechanically tunable extended cavity lasers with large frequency excursions of about 10 THz have been used in medical tomographic applications to achieve range resolutions of about 10 μm [26, 48]. However, linewidths of tens of GHz, which are typical for such devices, limit ranging depths to just a few mm [49, 50]. Moreover, the mechanical nature of the frequency tuning limits the scan repetition rate and adds overall system complexity. Commercially available semiconductor laser (SCL) diodes, on the other hand, offer superior sub-MHz linewidths, corresponding to ranging depths of a few hundred meters, and can be frequency tuned with current [5], enabling precise chirp control with closed-loop feedback [1]. The small size and high

wall-plug efficiency of these devices makes them attractive for hand-held applications. The wide gain bandwidth of semiconductor quantum wells and the ability to fabricate SCLs with precisely controlled emission frequencies [4] make possible sophisticated imaging modalities such as multiple source FMCW [13, 14], described in chapter 4.

In this chapter we begin by analyzing the SCL-based optoelectronic SFL. We derive equations governing the SFL closed-loop operation, and describe a bias current predistortion algorithm that improves the SFL linearity. We discuss the SCLs that were used in our experiments and describe an amplitude control sub-system that suppresses the intensity modulation of a current-tuned SCL. We demonstrate closed-loop linear chirps at range of chirp rates and wavelengths, and show that the optoelectronic SFL is capable of generating arbitrary chirp profiles. We describe our collaborative efforts with Telaris Inc. to implement the feedback and predistortion functionality on an embedded electronic platform and commercialize the SFL. We conclude by demonstrating the use of the optoelectronic SFL in reflectometry and profilometry applications.

3.2 System Analysis

A schematic diagram of the optoelectronic SFL is shown in figure 3.1. The system comprises an SCL coupled to a Mach-Zehnder interferometer (MZI), a photodetector at the MZI output, a mixer that compares the phases of the photocurrent and the reference oscillator, and an integrator that processes the mixed-down signal and feeds it back into the SCL. The MZI measures the instantaneous chirp slope, and the feedback loop locks it to a constant value that is determined by the reference frequency, ensuring a perfectly linear chirp. An amplitude controller is used to keep the SCL intensity constant as its frequency is tuned with input current. We begin our analysis by noting an analogy between the SFL feedback and a phase-locked loop (PLL). We then derive its steady-state operating point and analyze small-signal deviations in the frequency domain. We introduce an iterative predistortion procedure that relaxes constraints on the optoelectronic feedback and enables locking at high chirp rates.

We conclude by discussing different SCL platforms and how they motivate the choice of an amplitude control element.

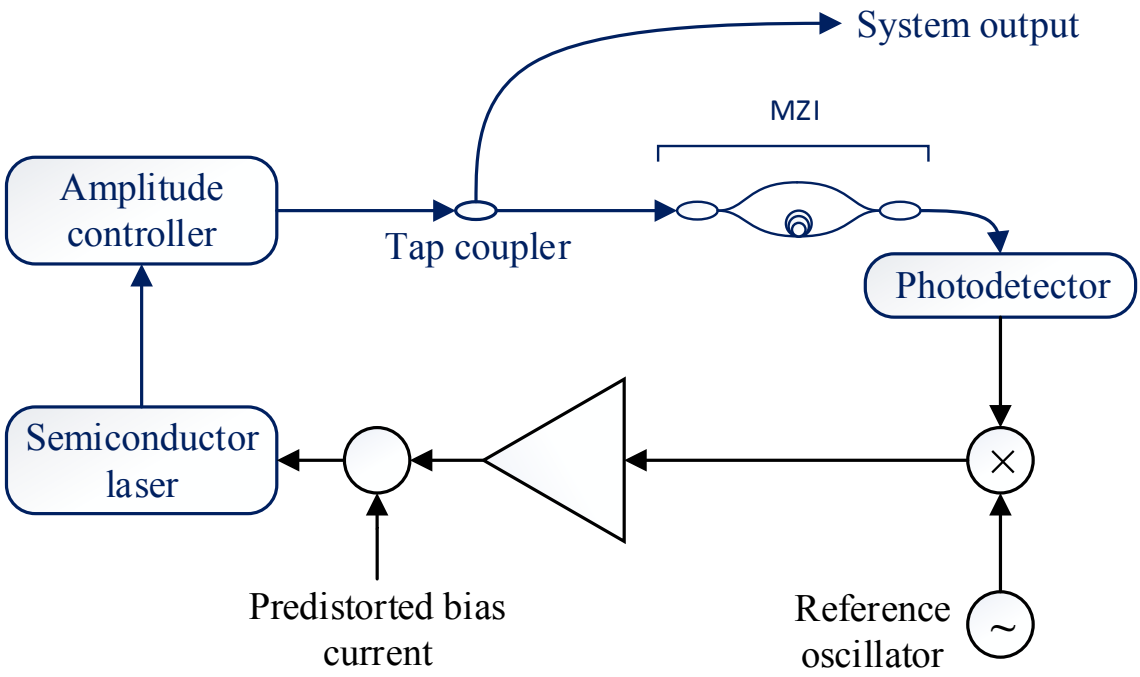

Figure 3.1: Schematic diagram of the SCL-based optoelectronic SFL

3.2.1 The Optoelectronic SFL as a PLL

We first demonstrate that the optoelectronic SFL acts like a phase-locked loop in the small-signal approximation. We begin by assuming that the SCL bias current predistortion is perfect, so that the output chirp is precisely linear. We will later remove this assumption by treating post-predistortion residual nonlinearity as additional phase noise. The electric field of a linear chirp is given by equation (2.1), replicated below without the rect function that models the chirp's finite duration:

$$e(t) = \cos\left[\phi_{SFL}(t)\right], \text{ and } \phi_{SFL}(t) \equiv \phi_0 + \omega_0 t + \frac{\xi t^2}{2}, \tag{3.1}$$

where $\phi_{SFL}(t)$ is an overall electric field phase that is quadratic in time, ξ is the slope of the optical chirp, and ϕ_0 and ω_0 are the initial phase and frequency, respectively.

The instantaneous optical frequency is therefore the derivative of $\phi_{SFL}(t)$:

$$\omega_{SFL}(t) = \frac{d\phi_{SFL}(t)}{dt}. \tag{3.2}$$

A tap coupler is used to launch a small amount of the chirped light into a MZI with delay τ. The beat signal between $e(t)$ and $e(t-\tau)$ is measured by a photodetector, so that its output current is given by:

$$\begin{aligned} i_{\mathrm{PD}} &\propto \cos\left[\phi_{SFL}(t) - \phi_{SFL}(t-\tau)\right] \\ &\approx \cos\left(\tau\frac{d\phi_{SFL}}{dt}\right) = \cos\left[\phi_{PD}(t)\right], \text{ and } \phi_{PD}(t) \equiv \omega_{SFL}(t)\tau, \end{aligned} \tag{3.3}$$

and we have ignored DC terms for simplicity. Equation (3.3) shows that if the MZI delay is chosen small enough, the photocurrent phase ϕ_{PD} is proportional to the instantaneous SCL frequency. Consider a small-signal $\delta s(t)$ at the input to the integrator in figure 3.1. Assuming that the integrated signal is small enough so that the SCL tuning remains linear, the associated change in the photocurrent phase $\delta\phi_{PD}(t)$ is given by:

$$\delta\phi_{PD}(t) = \delta\omega_{SFL}(t)\tau \propto \int^{t} \delta s(u)\, du, \tag{3.4}$$

where $\delta\omega_{SFL}(t)$ is the SCL frequency shift due to the additional bias current. The photocurrent phase shift is proportional an integral of $\delta s(t)$ in the small-signal approximation, which is the defining characteristic of an ideal voltage-controlled oscillator (VCO). The integrator, the SCL, the MZI, and the photodetector may therefore be lumped together and treated as a VCO. These elements are highlighted in figure 3.2.

The action of the optoelectronic SFL is therefore to lock the phase of the effective VCO to a reference electronic oscillator.

$$\phi^{L}_{PD}(t) = \phi_{REF}(t) + 2\pi n \implies \omega^{L}_{SFL}(t)\tau = \omega_{REF}t + \phi_{REF}(0) + 2\pi n,\ n \in \mathbb{Z}, \tag{3.5}$$

where $\phi_{REF}(t)$ is the overall phase of the reference oscillator and ω_{REF} is its fre-

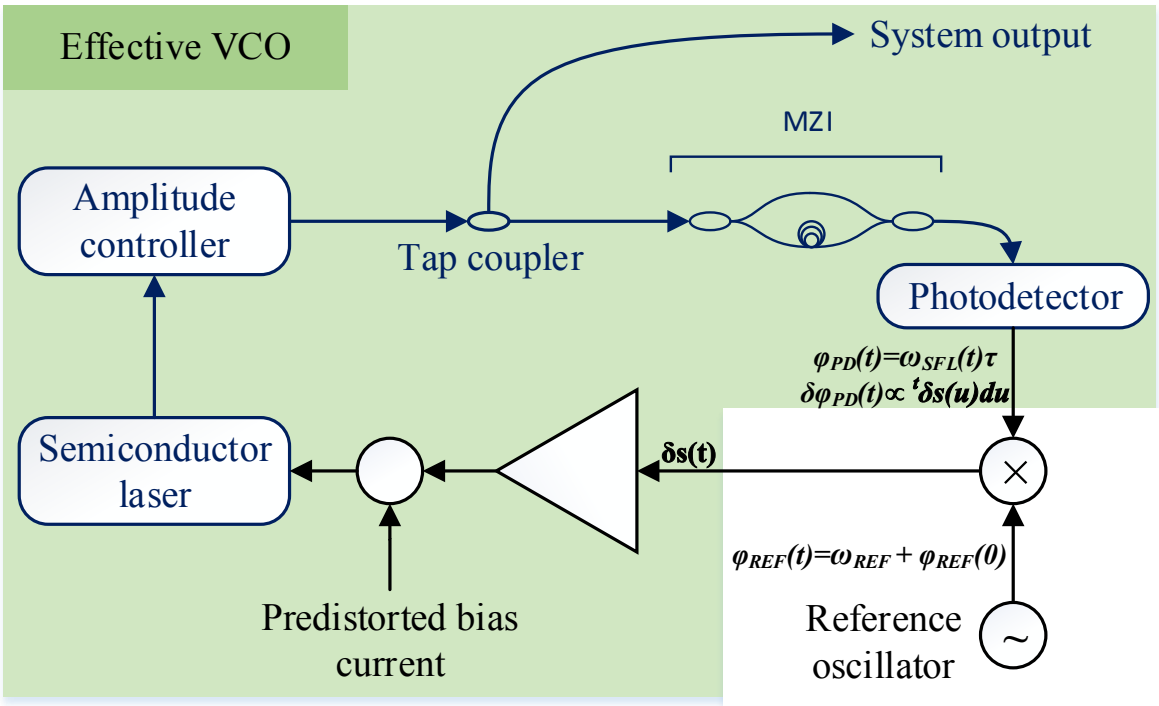

Figure 3.2: Elements of the optoelectronic SFL lumped together as an effective VCO

quency. We use the superscript L to denote quantities associated with the locked state. The feedback maintains a precisely linear chirp with a chirp rate and initial optical frequency given by

$$\xi^L = \frac{\omega_{REF}}{\tau} \text{ and } \omega_0^L = \frac{\phi_{REF}}{\tau} + n\frac{2\pi}{\tau}. \tag{3.6}$$

We recognize that $\frac{2\pi}{\tau}$ is just the free spectral range (FSR) of the MZI. Equation (3.5) describes a family of closed-loop linear chirp solutions indexed by the integer n. The solutions are separated in optical frequency by the MZI FSR, and the choice of a particular one depends on the free-running chirp parameters. Specifically, the system will lock to the solution whose initial optical frequency most closely matches the free-running optical frequency.

At the end of the scan the system is taken out of lock, and the SCL current is brought back to its original value. The chirp is consequently re-started and lock re-established. As a result, if the fluctuations in the free-running initial optical frequency are great enough, for example, due to imperfect SCL temperature control,

the SFL will lock to a different system solution during subsequent scans. To obtain repeatable chirps, it is therefore necessary to choose the MZI FSR large enough, so that fluctuations in the free-running chirp are localized around a single closed-loop solution.

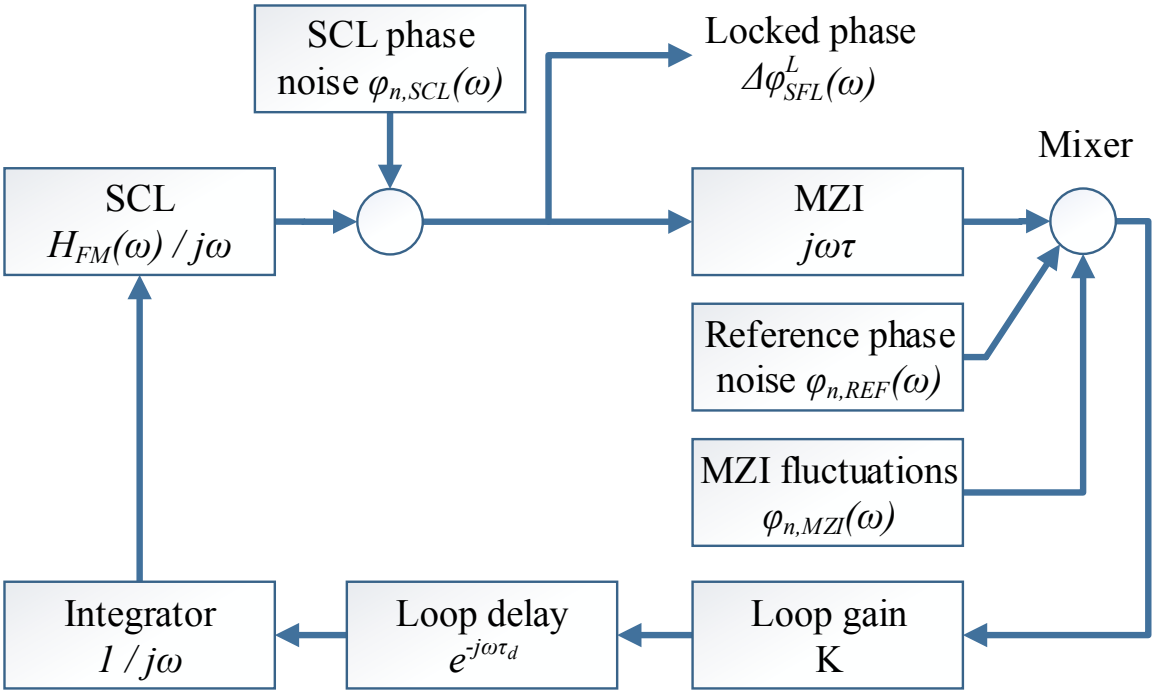

Figure 3.3: Small-signal frequency-domain model of the optoelectronic SFL

3.2.2 Small-Signal Analysis

The preceding discussion establishes an analogy between the optoelectronic SFL and a phase-locked loop. We now apply small-signal analysis [1, 51] to study fluctuations about the locked state in the Fourier domain, with the Fourier frequency denoted by ω. The small-signal model of the feedback loop is shown in figure 3.3. The loop variable is the deviation of the optical phase from its steady-state value,

$$\phi^{L}_{SFL}(t) = \phi_0 + \frac{\phi_{REF}}{\tau}t + n\frac{2\pi}{\tau}t + \frac{\omega_{REF}t^2}{2\tau}. \tag{3.7}$$

The transfer function of the SCL is $\frac{H_{FM}(\omega)}{j\omega}$, where $H_{FM}(\omega)$ is the frequency modulation (FM) response of the SCL, normalized to unity at DC, and $\frac{1}{j\omega}$ results from the

integral relationship between the SCL bias current and the optical phase. The FM response of single-section SCLs is characterized by a competition between thermal and electronic tuning mechanisms [52–55]. At low modulation frequencies, the optical frequency decreases with rising bias current due to increased junction heating. At higher modulation frequencies, carrier tuning dominates, and the optical frequency is increased with rising bias current. As a result, the FM response of the SCL undergoes a phase reversal in the Fourier frequency range of $0.1 - 10$ MHz. This phenomenon is the dominant bandwidth limitation in the optoelectronic SFL [7, 9].

For frequencies much smaller than its free spectral range, the MZI can be approximated as an ideal optical phase differentiator with gain τ (this is the same approximation as in equation (3.3)) [56]. The total DC loop gain K is given by the product of the gains of all the loop elements—laser, photodetector, mixer, integrator, and other electronic circuits that are not explicitly shown. The loop propagation delay τ_d is on the order of tens of ns. While it does add to the loop phase response at higher frequencies, around the feedback bandwidth its contribution is small compared to the phase acquired due to the SCL FM response.

The optical phase noise of the SCL and the optical phase excursion due to residual nonlinearity are lumped together and denoted by $\phi_{n,SCL}(\omega)$. The phase noise of the reference oscillator and the phase noise introduced by environmental fluctuations in the MZI are denoted by $\phi_{n,REF}(\omega)$ and $\phi_{n,MZI}(\omega)$, respectively. Going around the loop, we write a frequency-domain expression for the locked phase deviation $\Delta\phi^L_{SFL}(\omega)$ from the steady state.

$$\begin{aligned}\Delta\phi^L_{SFL}(\omega) = \phi_{n,SCL}(\omega) - K\frac{H_{FM}(\omega)e^{-j\omega\tau_d}}{\omega^2}\left[\phi_{n,REF}(\omega) + \phi_{n,MZI}(\omega)\right] \\ + K\tau\frac{H_{FM}(\omega)e^{-j\omega\tau_d}}{j\omega}\Delta\phi^L_{SFL}(\omega)\end{aligned} \tag{3.8}$$

Solving for $\Delta\phi^L_{SFL}(\omega)$ yields

$$\begin{aligned}\Delta\phi^L_{SFL}(\omega) = &\frac{j\omega}{j\omega + K\tau H_{FM}(\omega)e^{-j\omega\tau_d}}\phi_{n,SCL}(\omega) \\ &+ \frac{1}{j\omega\tau} \times \frac{K\tau H_{FM}(\omega)e^{-j\omega\tau_d}}{j\omega + K\tau H_{FM}(\omega)e^{-j\omega\tau_d}} \left[\phi_{n,REF}(\omega) + \phi_{n,MZI}(\omega)\right].\end{aligned} \tag{3.9}$$

We observe that for frequencies within the loop bandwidth, the residual phase deviation tracks the reference oscillator and MZI noise, suppressed by the term $j\omega\tau$,

$$\Delta\phi^L_{SFL}(\omega \ll K\tau) \approx \frac{\phi_{n,REF}(\omega) + \phi_{n,MZI}(\omega)}{j\omega\tau}. \tag{3.10}$$

For frequencies outside the loop bandwidth, the residual phase deviation is given by the free-running phase noise term,

$$\Delta\phi^L_{SFL}(\omega \gg K\tau) \approx \phi_{n,SCL}(\omega). \tag{3.11}$$

From equation (3.10) it is clear that there are three considerations involved in the generation of precisely linear chirps: (1) using an electronic oscillator with low phase noise, (2) stabilizing the MZI against acoustic and thermal fluctuations, and (3) picking a large τ.

High quality electronic oscillator integrated circuits are widely available. In our systems we use direct digital synthesis (DDS) oscillators because they offer excellent phase and frequency stability, precise control of the reference frequency, and broad frequency tuning. The latter is useful in generating a wide range of chirp rates.

Active and passive interferometer stabilization techniques are well known, and include locking the delay to a reference laser using a fiber stretcher [57], athermal design of the MZI waveguides [58], and the use of vibration-damping polymers in interferometer packaging [59], to name a few. In our systems we use fiber-based MZIs packaged with sheets of Sorbothane®.

The choice of MZI delay is constrained by the free-running frequency fluctuations of the SCL, as discussed in section 3.2.1. In our systems we choose the largest

τ that yields repeatable chirps from scan to scan. For distributed-feedback laser (DFB) systems we use a delay from 5ns to as much as 30 ns, depending on the laser quality. Systems based on vertical-cavity surface-emitting lasers (VCSELs) possess more frequency jitter, and we therefore use MZIs with delays of about 1 ns.

3.2.3 Bias Current Predistortion

So far we have assumed that the SCL bias current is predistorted so that the chirp is sufficiently linear for lock acquisition. In this section we describe a predistortion procedure based on a simple nonlinear tuning model [1]. Even though the model is inaccurate, and a single use of this procedure does not yield a linear chirp, it is possible to achieve the desired linearity through iteration.

We model the nonlinear current-frequency relation of an SCL by introducing a tuning constant K that is a function of the SCL modulation current.

$$\omega_{SFL}(t) = \omega_0 + i(t)K[i(t)], \tag{3.12}$$

where ω_0 is the initial SCL frequency due to some bias current, and $i(t)$ is the deviation from that bias. To characterize the chirp we calculate the spectrogram of the MZI photocurrent. The spectrogram allows us to extract the instantaneous photocurrent frequency, found by differentiating the photocurrent phase in equation (3.3)

$$\omega_{PD}(t) = \frac{d\phi_{PD}(t)}{dt} = \tau\frac{d\omega_{SFL}(t)}{dt}. \tag{3.13}$$

Plugging in equation (3.12), we arrive at

$$\omega_{\mathrm{PD}}(t) = \tau\frac{d\omega_{SFL}(t)}{dt} = \tau\left[K(i) + iK'(i)\right]\frac{di(t)}{dt} = S(i)\frac{di(t)}{dt}, \tag{3.14}$$

where $S(i) \equiv K(i) + iK'(i)$. The function $S(i)$ describes the nonlinear tuning of the SCL and can be measured by launching a linear current ramp into the SCL and using

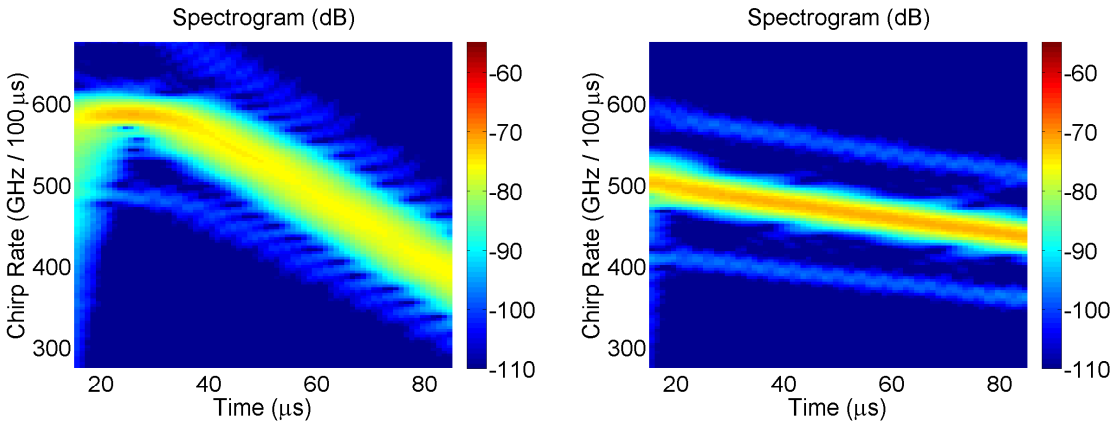

(a) Current ramp chirp spectrogram (b) Predistorted chirp spectrogram

Figure 3.4: Single predistortion results

a spectrogram to calculate $\omega_{\mathrm{PD}}(t)$. Then,

$$S(i) = \frac{\omega_{\mathrm{PD}}\left[t(i)\right]}{\alpha}, \tag{3.15}$$

where α is the current ramp slope. We use equation (3.14) to write a differential equation for the SCL modulation current

$$\frac{di(t)}{dt} = \frac{\tau}{S(i)}\frac{d\omega_{SFL,d}}{dt}, \tag{3.16}$$

where $\omega_{SFL,d}(t)$ is the desired optical chirp. We solve this equation numerically to find the current that will generate the desired tuning behavior $\omega_{SFL,d}(t)$.

The outlined procedure was used to predistort the current for a 1.55 μm VCSEL chirping 475 GHz in 100 μs. According to equation (3.13), a perfectly linear chirp is described by a flat photocurrent spectrogram. Figure 3.4a shows the spectrogram corresponding to a current ramp that was used to characterize $S(i)$. The y-axis has been rescaled by τ to show the instantaneous chirp rate. Figure 3.4b shows the spectrogram corresponding to the predistorted waveform, confirming the improvement in linearity.

Figure 3.4b is not perfectly flat, meaning that the corresponding optical chirp is not perfectly linear. The reason is that the tuning model is incomplete—it fails to cap-

ture dynamic tuning behavior, e.g., the competition between thermal and electronic tuning mechanisms described in section 3.2.2. Even though the model is incomplete, its application yields an improvement in chirp linearity. It stands to reason that iterative application of the model may yield additional improvements in chirp linearity. Iterative application means that we use the previous current predistortion to re-characterize the function $S(i)$, and calculate the next approximation by again solving equation (3.16). This process is repeated until the ensuing optical chirp is perfectly linear. We can combine equation (3.16) and equation (3.14) to write down the differential equation that can be used to calculate the n^{th}-order predistortion $i_n(t)$ from the preceding order predistortion, $i_{n-1}(t)$, and the corresponding photocurrent frequency measurement $\omega_{PD,n-1}(t)$.

$$\frac{di_n(t)}{dt} = \frac{\xi_d \tau}{\omega_{PD,n-1}\left[t_{n-1}(i_n)\right]} \times \frac{di_{n-1}}{dt}, \tag{3.17}$$

where ξ_d is the desired chirp rate, and $t_{n-1}(i)$ is the inverse of the i_{n-1}-th predistortion.

We have found that using a fourth-order predistortion is sufficient. The results are shown in figure 3.5. Each successive predistortion results in a chirp that is closer to the desired tuning characteristic, so that by the fourth order we arrive at a sufficiently linear chirp.

It is possible to further simplify the predistortion procedure. In equation (3.17) we evaluate the photocurrent frequency at time $t_{n-1}(i_n) = i_{n-1}^{-1}(i_n)$. It stands to reason that once the difference between successive predistortions is small enough, the photocurrent frequency may be evaluated just at time t,

$$\frac{di_n(t)}{dt} = \frac{\xi_d \tau}{\omega_{PD,n-1}(t)} \times \frac{di_{n-1}}{dt}. \tag{3.18}$$

This procedure makes sense intuitively—the slope of the previous predistortion is scaled by the ratio of the desired photocurrent frequency to the instantaneous photocurrent frequency. If the chirp is too fast, then the ratio will be less than one, slowing down the sweep at that particular time. Likewise, if the chirp is too slow, the

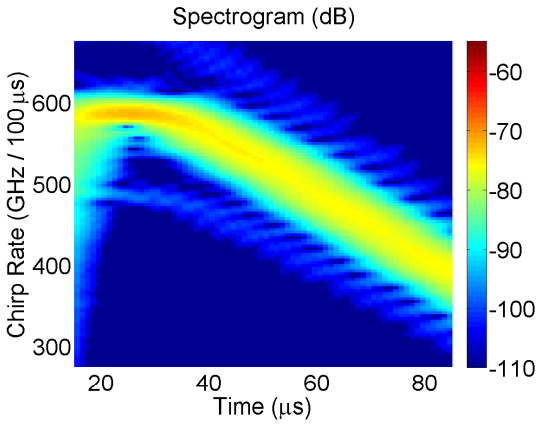

(a) Zeroth-order predistortion (current ramp) spectrogram

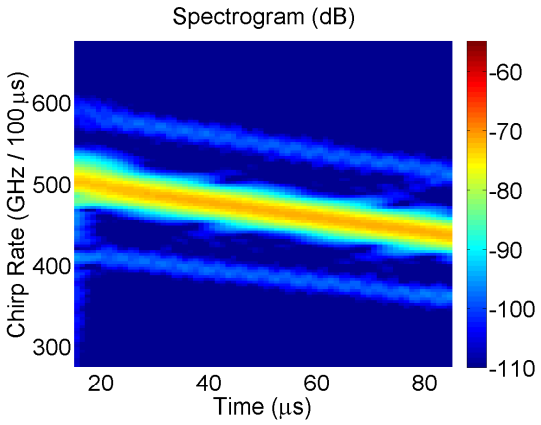

(b) First-order predistortion spectrogram

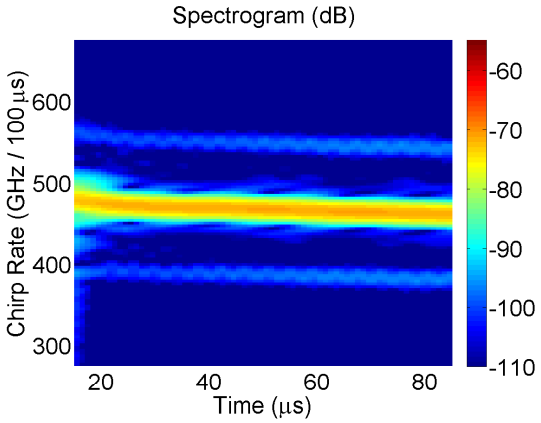

(c) Second-order predistortion spectrogram

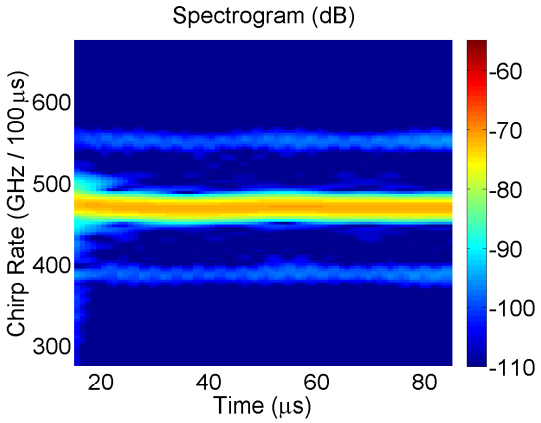

(d) Third-order predistortion spectrogram

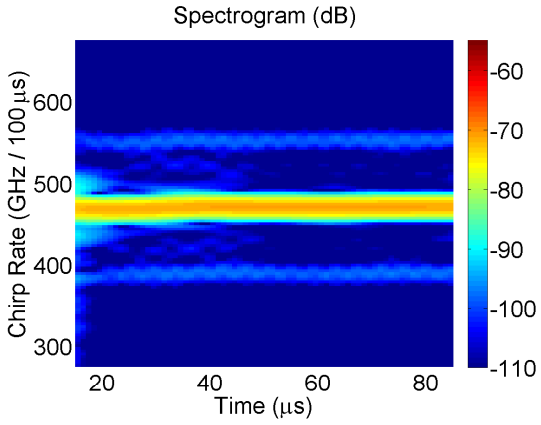

(e) Fourth-order predistortion spectrogram

Figure 3.5: Iterative predistortion results

ratio will be greater than unity, speeding it up.

This procedure is simpler computationally—it does not involve inverses, and therefore avoids interpolation. The differential equation (3.18) itself is simpler as well, since the right hand side no longer depends on i_n. We motivated these simplifications with the assumption that the successive predistortions are already close to each other. It is the case, however, that the simplified procedure works well in practice, and demonstrates the same rate of convergence as the original scheme, even if iterated starting at the linear current ramp. As part of our collaboration with Telaris Inc. to commercialize the optoelectronic SFL, we have implemented the simplified predistortion procedure on a microcontroller. The full predistortion procedure would have been significantly more difficult to realize in the computationally-limited embedded environment.

3.3 Design of the Optoelectronic SFL

3.3.1 SCL Choice

The choice of the semiconductor laser to use in the optoelectronic SFL is dependent upon the desired chirp bandwidth and linewidth. Distributed-feedback lasers (DFB) are inherently single-mode, possess a stable polarization, and a narrow linewidth of hundreds of kHz to a $\sim$ 1 MHz. The chirp ranges of commercially-available DFB lasers depend on the emission wavelength. In our experience, 1550 nm DFB lasers are limited in chirp range to about 100 GHz. The frequency chirp range increases with decreasing wavelength, and we have found that DFB lasers in the 1060 nm range can be current-tuned over a spectral range of about 200 GHz. The output power of DFB lasers is usually in the tens of mW.

When compared to DFBs, vertical-cavity surface-emitting lasers (VCSELs) are much cheaper, and generally tune over greater regions of the optical spectrum. We have tested VCSELs at wavelengths of 1550 nm, 1310 nm, 1060 nm, and 850 nm. We measured chirp bandwidths of $\sim$ 500 GHz at 1550 nm, $\sim$ 1 THz at 1310 nm,

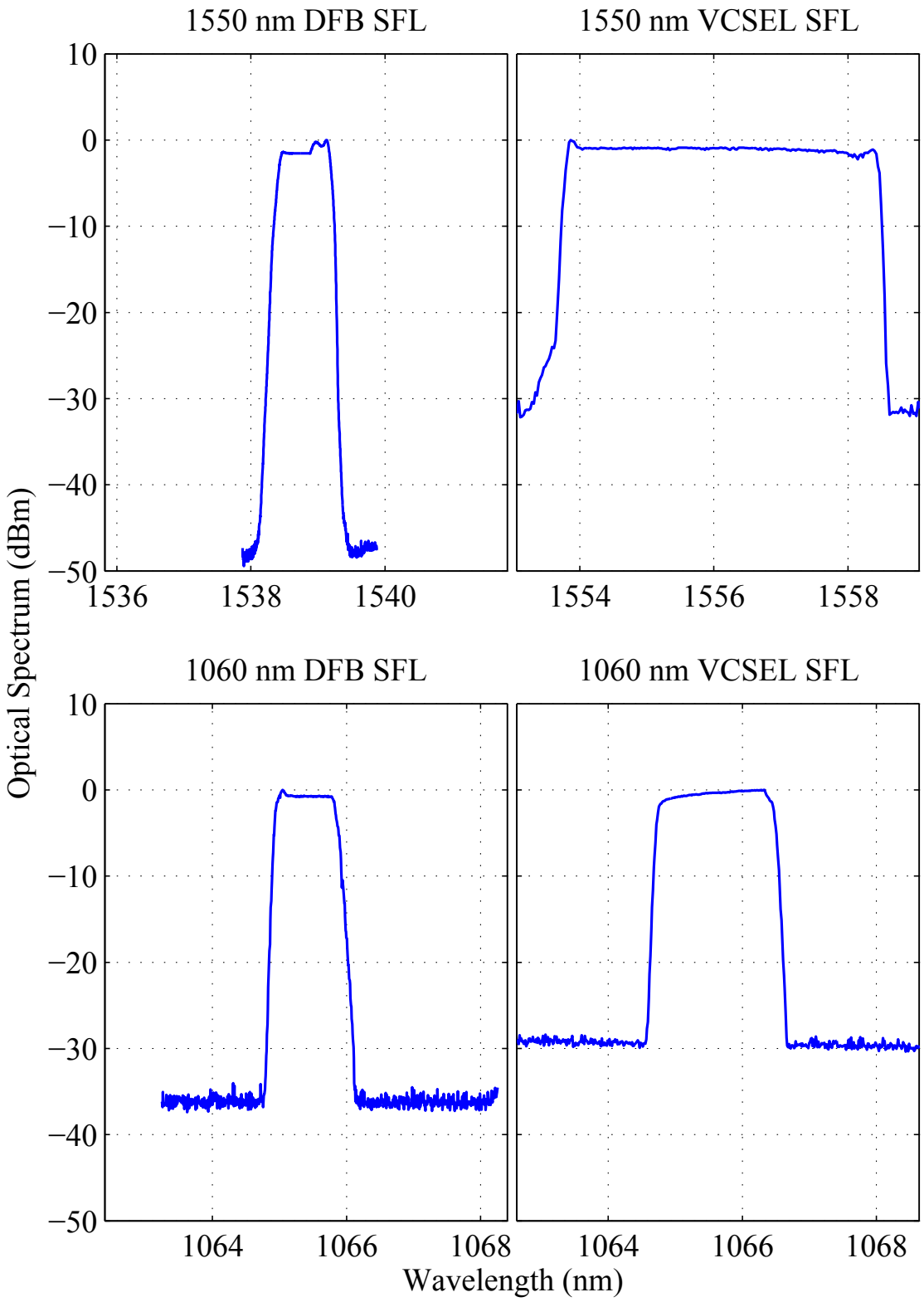

Figure 3.6: Measured optical spectra of DFB and VCSEL SFLs at wavelengths of 1550 nm and 1060 nm

$\sim$ 400 GHz at 1060 nm, and $\sim$ 1.5 THz at 850 nm. The 1060 nm VCSEL breaks the pattern, possibly because this is the least-developed VCSEL wavelength. Because of their short cavity lengths, VCSELs have broader linewidths of a few tens of MHz, and suffer from a reduced frequency stability. The reduced stability necessitates the use of shorter MZIs in the SFL feedback, increasing the closed-loop residual phase error, as described in section 3.2.2. In addition, VCSELs possess significantly lower powers of hundreds of μW to a few mW. As a result, VCSEL-based SFLs require amplitude control elements capable of providing optical gain, as described in section 3.3.2. Due to the circular symmetry of the VCSEL cavity, these devices sometimes have polarization instability and polarization mode hops [60], limiting their use in applications requiring polarization control. Nevertheless, VCSELs remain extremely attractive as swept sources in imaging and ranging applications due to their broad chirp bandwidths.

The optical spectra of the locked optoelectronic SFLs based on some of the SCLs discussed above are shown in figure 3.6. Swept sources based on 1310 nm and 850 nm VCSELs are currently being developed.

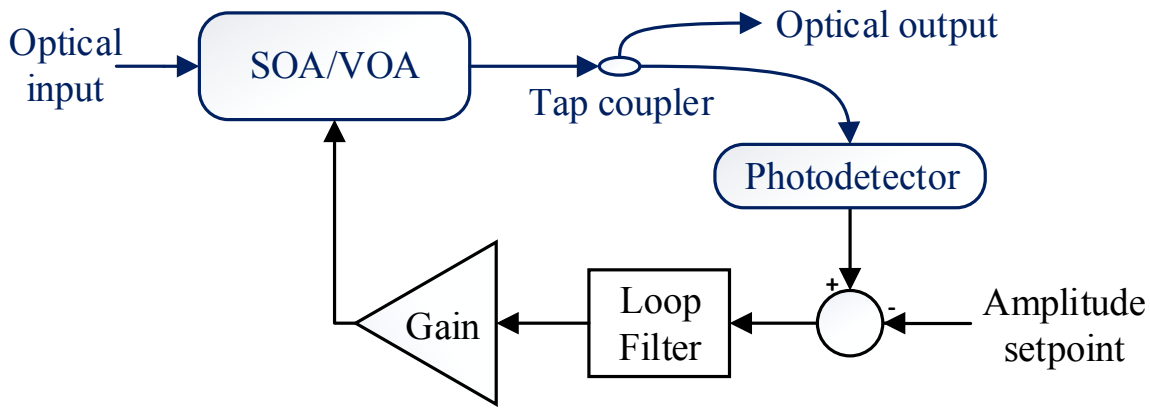

Figure 3.7: Schematic diagram of the amplitude controller feedback system

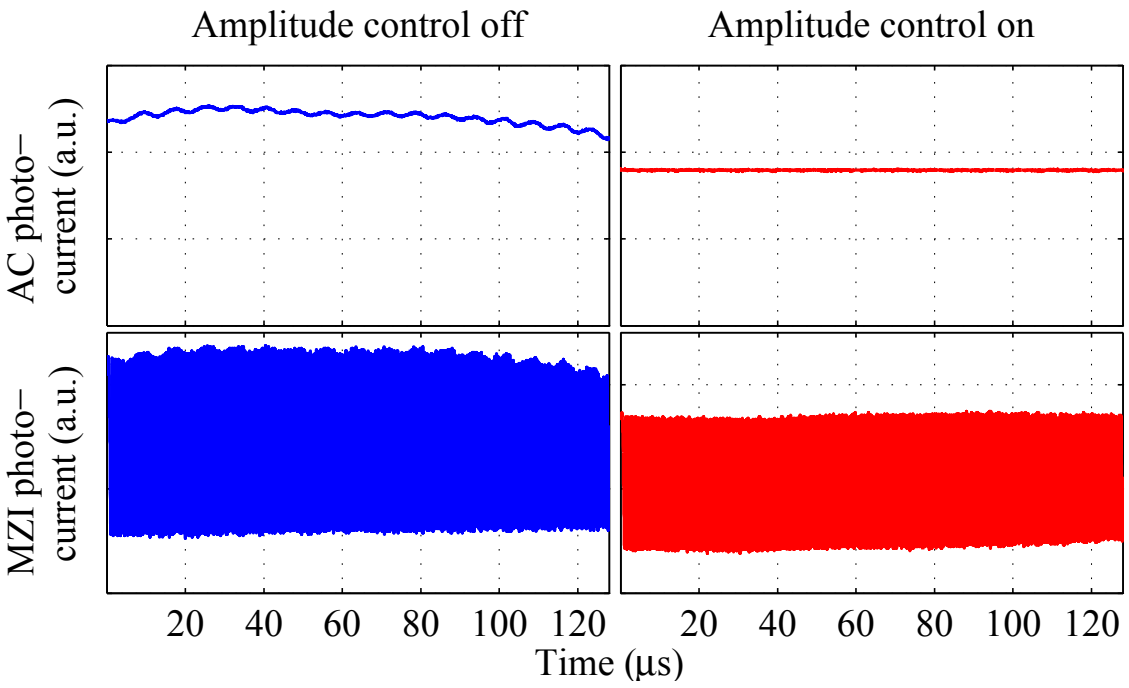

Figure 3.8: Comparison between the off(blue) and on(red) states of the SOA amplitude controller

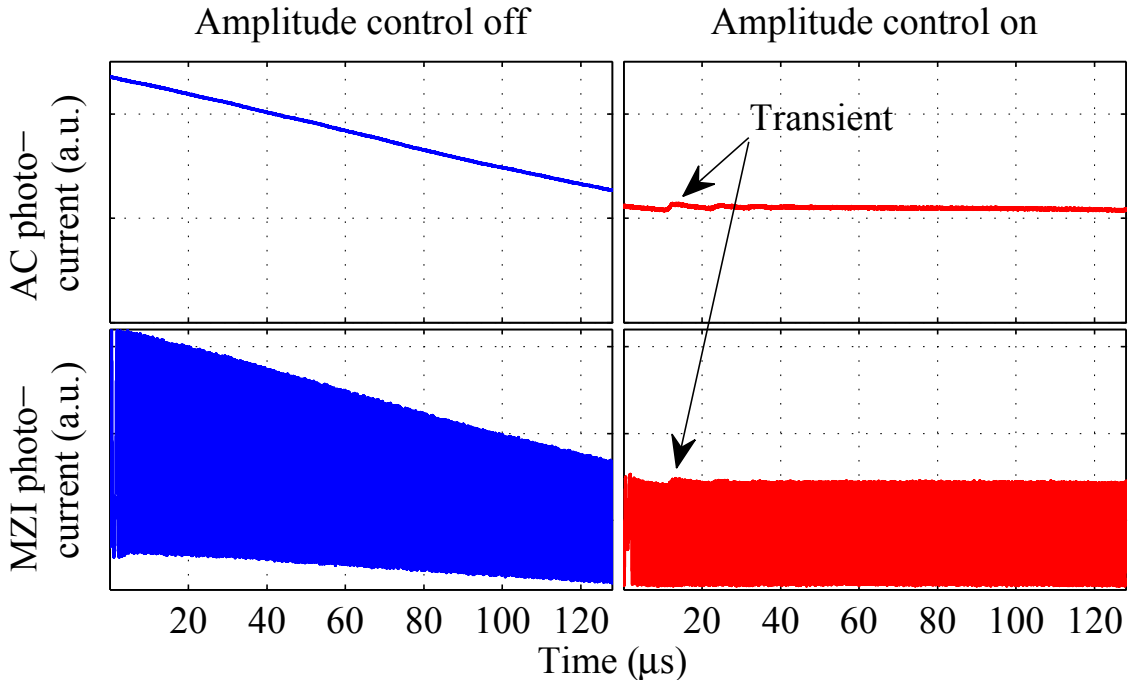

Figure 3.9: Comparison between the off(blue) and on(red) states of the VOA amplitude controller

3.3.2 Amplitude Control

As the SCL current is swept to produce a frequency chirp, the light undergoes undesired amplitude modulation. To overcome this effect, we place an amplitude controller after the SCL. The amplitude controller is a feedback system, shown in figure 3.7, that uses an intensity modulator and a tap photodetector to measure the instantaneous optical intensity, and lock it to a constant value. In our systems we have used two different intensity modulation elements—semiconductor optical amplifiers (SOAs) and variable optical attenuators (VOAs) based on electro-optical ceramics [61]. The SOAs provide optical gain, have GHz-range modulation bandwidths [62], but require temperature control and heat sinking. Furthermore, additional optical isolation is necessary to prevent lasing. VOAs solutions are cheaper and more compact because they do not generate excess heat, but they are also much slower, with sub-MHz modulation bandwidths. Because VOAs are passive devices, they are only practical for use with SCLs that emit sufficiently high optical powers. We use SOAs with VCSEL-based systems, which serves the dual purpose of amplitude control and optical amplification of the weak VCSEL output, and reserve the use VOAs for DFB-based SFLs.

The effect of the SOA-based amplitude controller on a chirped VCSEL input is shown in figure 3.8. The amplitude controller feedback signal is shown in the top panels and the MZI photocurrent is plotted in the bottom panels. When the amplitude controller is turned on, the intensity of the input into the MZI becomes fixed, suppressing the fluctuations in the MZI signal envelope. Corresponding plots for the DFB-VOA combination are shown in figure 3.9. Because the VOA is considerably slower than the SOA, transient effects appear in the beginning of the scan.

3.3.3 Electronics and Commercialization

As part of our collaboration with Telaris Inc., the company has commercialized the optoelectronic SFL. The chirped diode laser (CHDL) system offered by Telaris Inc. is a stand-alone SFL that is controlled by a computer through a USB port. The feedback electronics are implemented on a pair of printed circuit boards (PCBs),

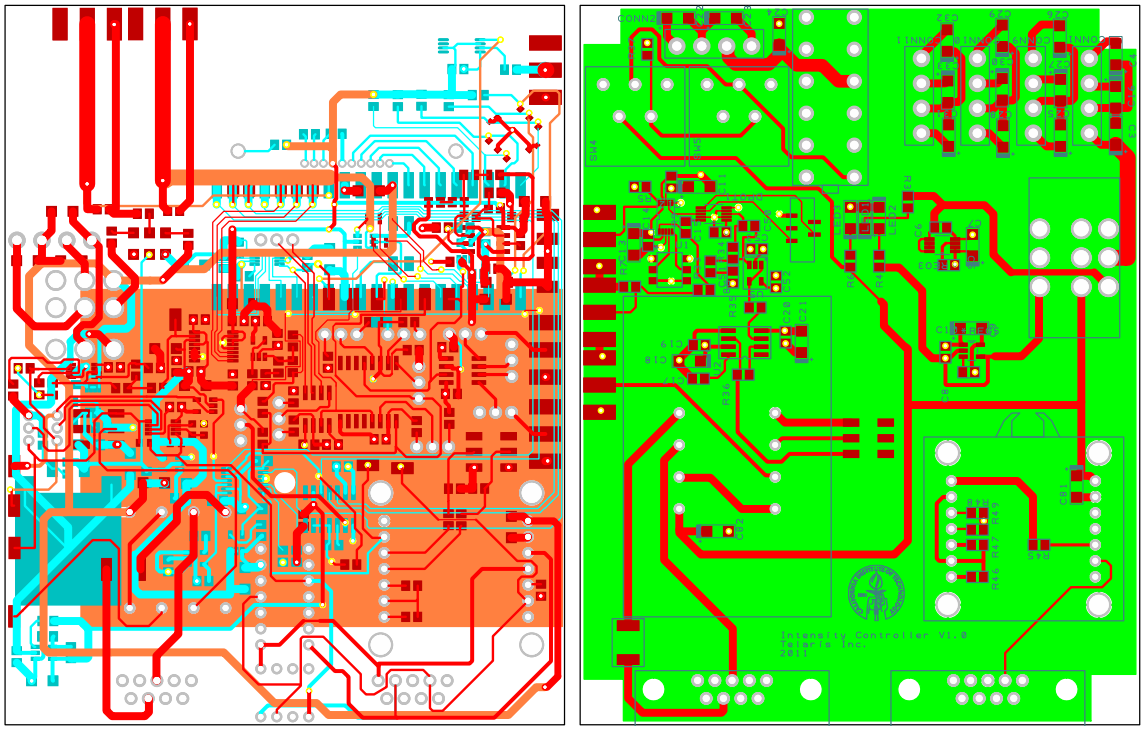

(a) SFL feedback PCB (b) Amplitude controller PCB

Figure 3.10: Optoelectronic SFL printed circuit board layouts

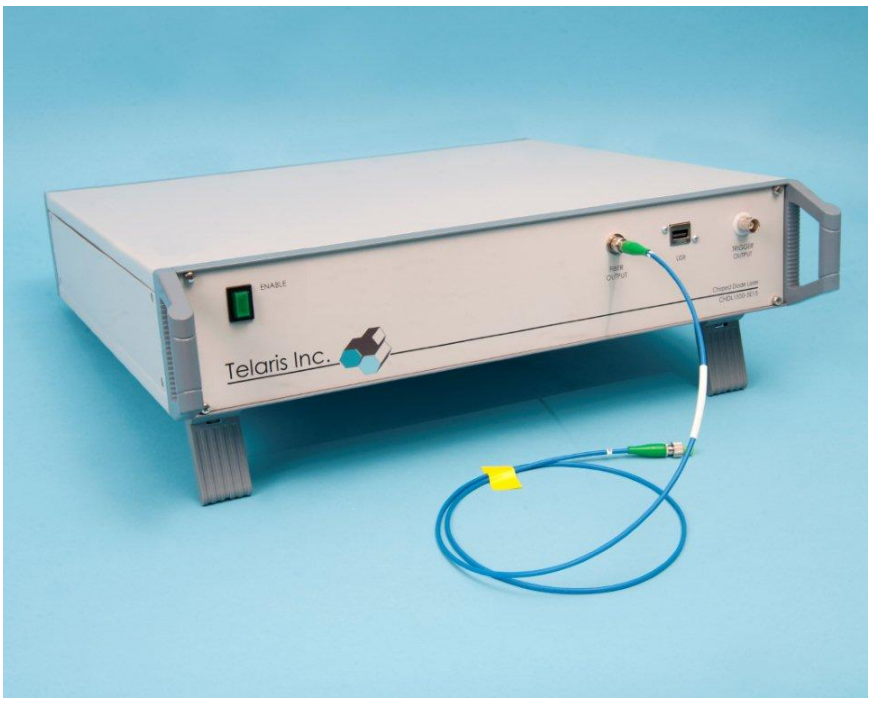

Figure 3.11: The 1550 nm CHDL system.

shown in figure 3.10. The boards include low-noise current sources and temperature controllers for the SCL and the SOA-based amplitude controller, a direct digital synthesis (DDS) chip to provide a frequency-agile reference oscillator, a 1 μs sampling rate digital-to-analog converter to generate predistortion waveforms, an offset-trimmed multiplier, and digital potentiometers to provide control over the various feedback gain and filter parameters. Calculating spectrograms for the predistortion procedure is a computationally-intensive task. Instead, the MZI signal is digitized using a comparator, and its instantaneous frequency is calculated by counting the number of zero-crossings that occur in a specified time window. This hardware-assisted predistortion measurement, along with the simplified algorithm described in section 3.2.3, enables rapid predistortion of the SCL bias current in an embedded environment. The entire system is controlled by an 8-core microcontroller. Parallel cores provide deterministic timing that is necessary for the simultaneous processing of the MZI signal and generation of the predistortion waveform. The system uses an acoustically-isolated fiber MZI to generate the feedback signal. The VCSEL-based 1550 nm CHDL system is shown in figure 3.11, and is capable of generating precisely linear chirps exceeding 500 GHz in bandwidth, at a maximum rate of 10 kHz.

3.4 Experimental Results

3.4.1 Precisely Controlled Linear Chirps

The optoelectronic SFL is turned on by first iterating the predistortion procedure, as described in section 3.2.3, with the MZI feedback gain set to zero. The MZI photocurrent spectra at different steps of this process are shown in figure 3.12. The x-axis has been scaled by the MZI FSR to correspond to the chirp rate ξ. Successive predistortion steps lead to a narrowing of the signal peak at the desired chirp rate. By the 3^{rd} predistortion, the signal peak width has achieved the transform limit $\frac{1}{\tau T}$, and additional predistortion steps reduce the noise pedestal. Once sufficient linearity is achieved with the predistortion, the feedback gain is turned on, and the SFL acquires

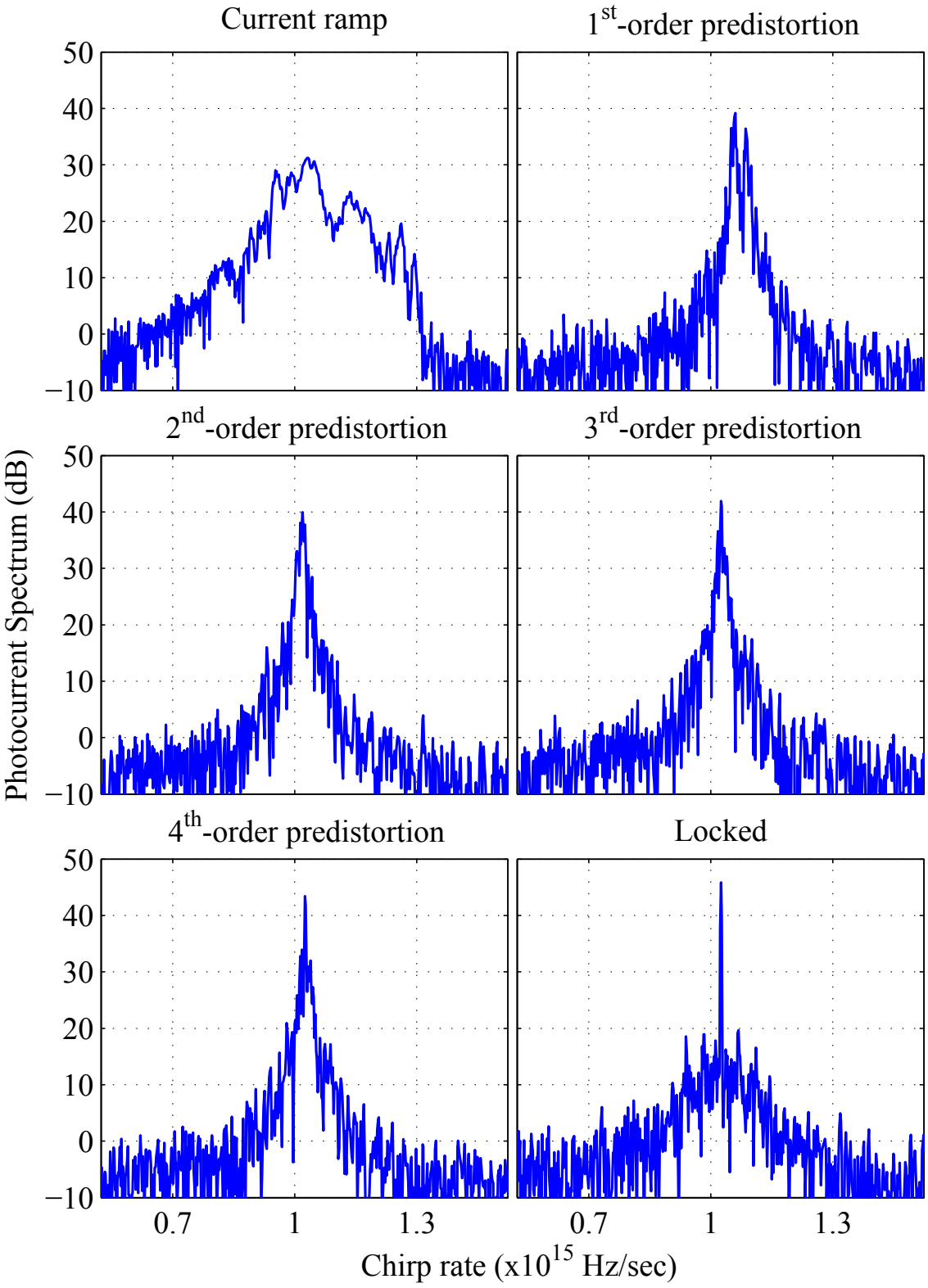

Figure 3.12: MZI photocurrent spectrum during the predistortion process and in the locked state

lock, yielding a constant chirp slope and a fixed starting frequency. The locked spectrum is characterized by a transform-limited peak with a low noise pedestal.

The chirp rate of the optoelectronic SFL is controlled by tuning the frequency of the electronic reference oscillator. The systems that we have built are capable of generating linear chirps with rates that are tunable over a decade. The locked spectra at different chirp rates of an optoelectronic SFL based on a 1550 nm DFB laser are shown in figure 3.13a. Corresponding spectra for a 1550 nm VCSEL system are shown in figure 3.13b, for a 1060 nm DFB system in figure 3.13c, and for a 1060 nm VCSEL system in figure 3.13d. The x-axis in all the plots corresponds to the chirp rate.

3.4.2 Arbitrary Chirps

So far we have focused on precisely linear chirps. The optoelectronic feedback technique can be extended in a straightforward way to generate arbitrary frequency chirps [1]. The predistortion procedure is modified to include time-dependence in the desired chirp rate ξ_d in equation (3.17) and equation (3.18). The integral of $\xi_d(t)$ gives the desired optical frequency vs. time function. Similarly, the locking frequency ω_{REF} becomes a function of time. The locked optical frequency evolution of the SFL will therefore be given by

$$\omega_{SCL}(t) = \frac{1}{\tau}\int_0^t \omega_{REF}(t)dt + \frac{\phi_{REF}}{\tau} + n\frac{2\pi}{\tau}, \tag{3.19}$$

where ϕ_{REF} is again the DC phase of the reference oscillator, and the integer n indexes the family of possible locked behaviors.

We have demonstrated this principle experimentally by generating quadratic and exponential optical frequency chirps using a DFB-based SFL at 1550 nm. For the quadratic chirp, we varied the reference frequency between 1.43 and 4.29 MHz, corresponding to a linear variation of the chirp rate from 50 to 150 GHz/ms. The measured photocurrent spectrogram in figure 3.14 matches the desired chirp characteristic exactly. In the exponential chirp case, we varied the reference frequency according

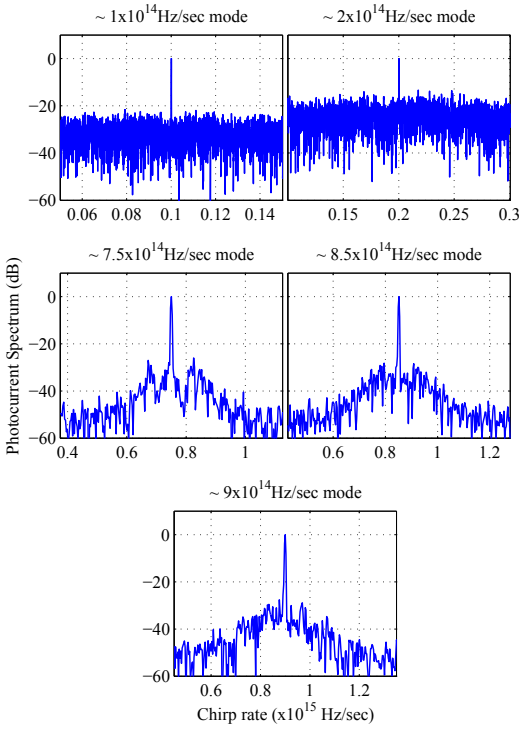

(a) 1550 nm DFB SFL

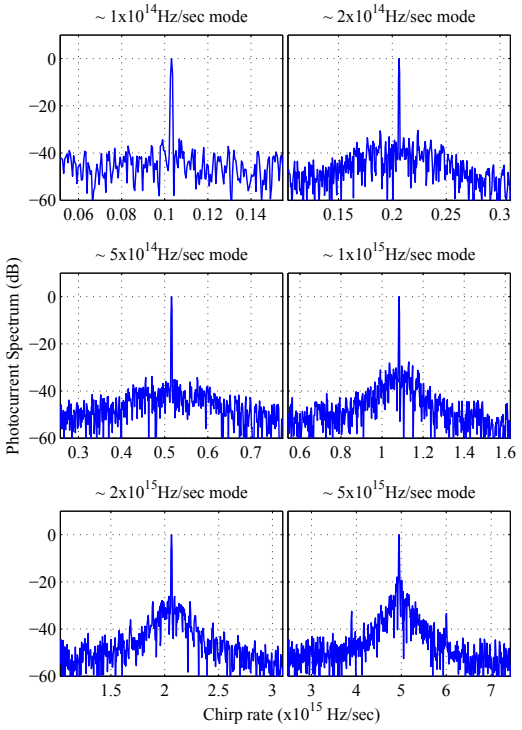

(b) 1550 nm VCSEL SFL

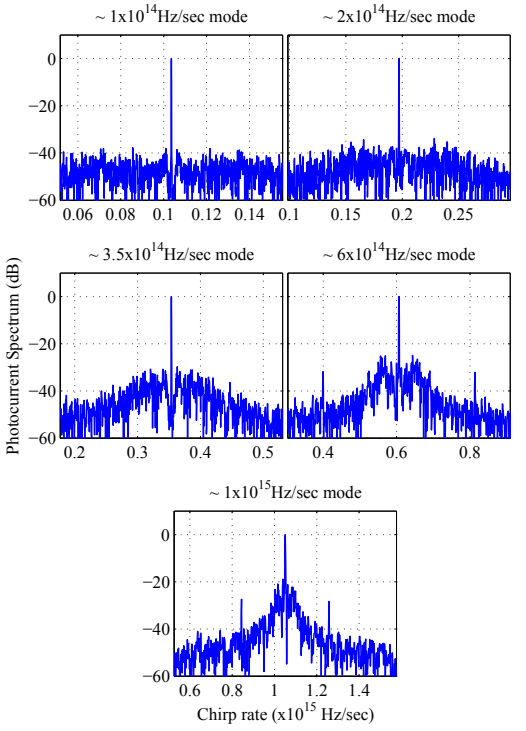

(c) 1060 nm DFB SFL

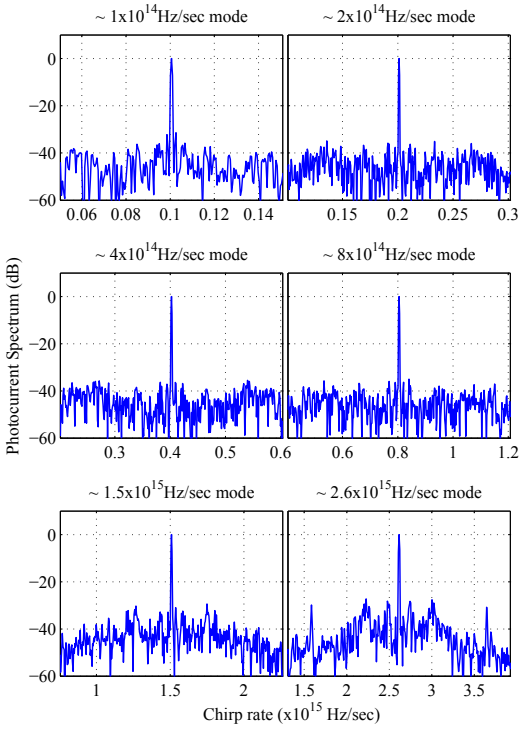

(d) 1060 nm VCSEL SFL

Figure 3.13: Locked MZI spectra of various SFLs for different values of the chirp rate ξ. The x-axis in all the plots corresponds to the chirp rate.

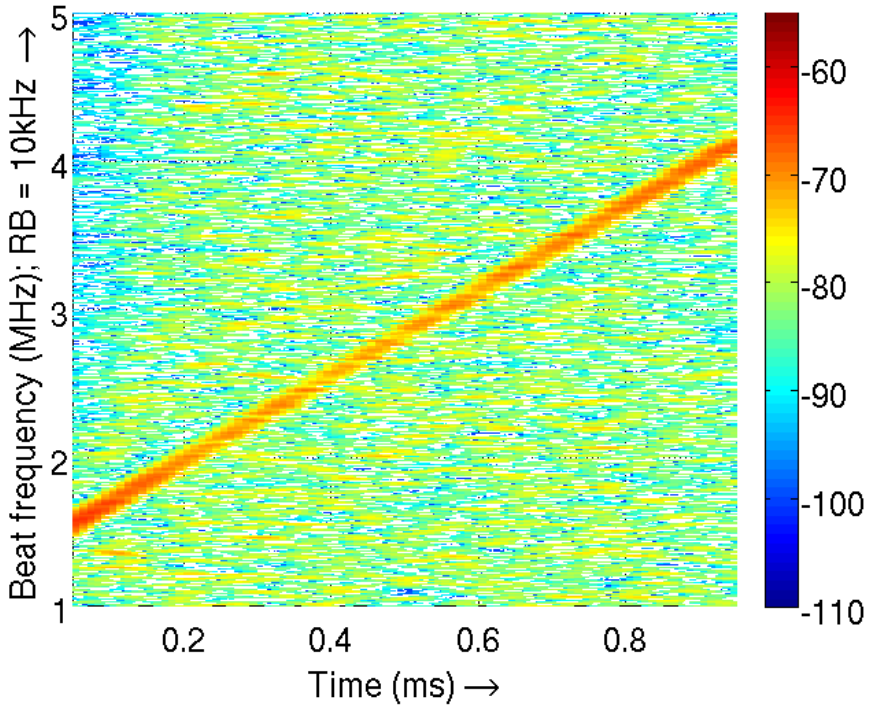

Figure 3.14: Quadratic chirp spectrogram

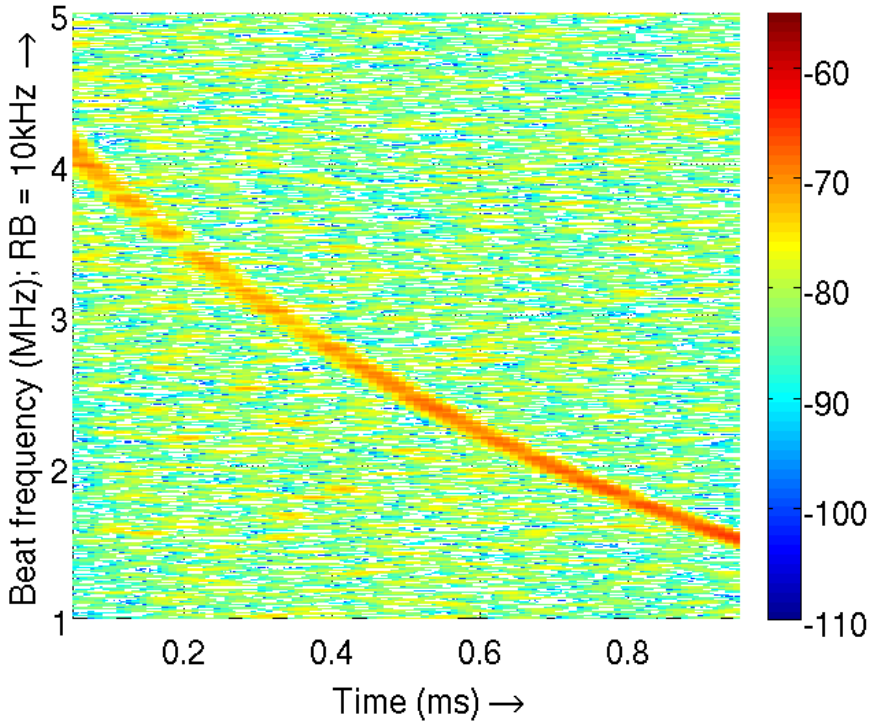

Figure 3.15: Exponential chirp spectrogram

to

$$\omega_{REF}(t) = 2\pi \times (4.29 \text{ MHz}) \times \left(\frac{1.43 \text{ MHz}}{4.29 \text{ MHz}}\right)^{t/(1 \text{ ms})}. \quad (3.20)$$

This corresponds to an exponential decrease of the optical chip rate from 150 to 50 GHz/ms. The measured photocurrent spectrogram is shown in figure 3.15. A combination of bias current predistortion and optoelectronic feedback can therefore be used for arbitrary chirp generation.

3.5 Demonstrated Applications

3.5.1 FMCW Reflectometry Using the Optoelectronic SFL

The development of the optoelectronic SFL was motivated by FMCW reflectometry and its applications in ranging and 3-D imaging (see chapter 2). The free-space depth resolution of an FMCW system is given by equation (2.8), and a bandwidth of 500 GHz corresponds to a free-space resolution of 0.3 mm. For a medium with index of refraction n, the depth resolution is given by

$$\Delta z = \frac{c}{2nB}, \quad (3.21)$$

where B is the chirp bandwidth of the SFL. We demonstrated the use of the VCSEL-based optoelectronic SFL in FMCW reflectometry by imaging acrylic sheets of varying thickness and a refractive index of 1.5 using the experimental configuration of figure 2.2. Reflections from the front and back acrylic surfaces show up as peaks in the FMCW photocurrent spectrum, shown in figure 3.16 for four sheets with nominal thicknesses of (a) 4.29 mm, (b) 2.82 mm, (c) 1.49 mm, and (d) 1.00 mm. The x-axis has been scaled to distance. The measured peak separations agree well with the nominal values. The bandwidth of the SFL was 500 GHz, corresponding to a resolution of 0.2 mm in acrylic. As a result, all of the reflection pairs shown in figure 3.16 are very well resolved.

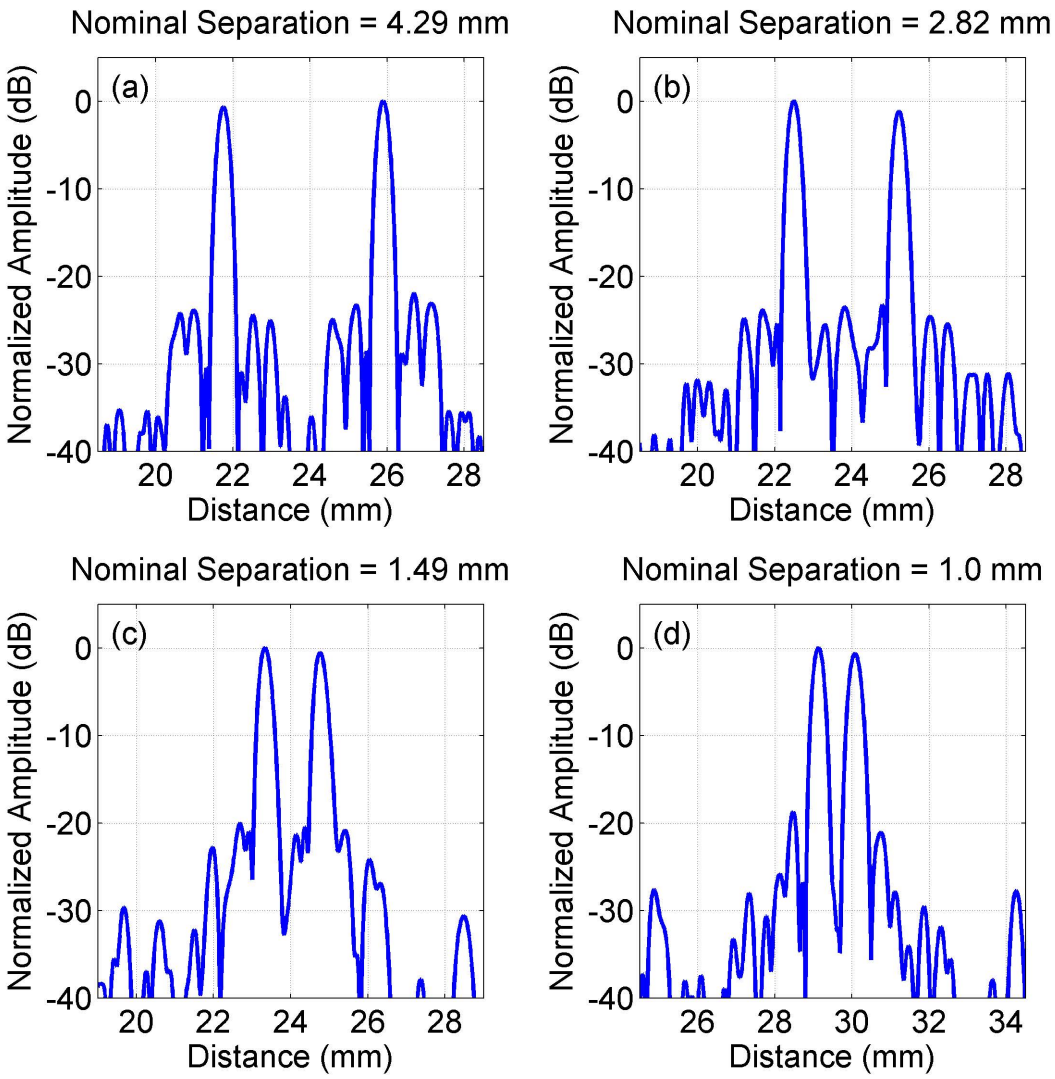

Figure 3.16: FMCW reflectometry of acrylic sheets using the VCSEL-based optoelectronic SFL with a chirp bandwidth of 500 GHz and a wavelength of $\sim$ 1550 nm

3.5.2 Profilometry

The range resolution of an FMCW system describes its ability to tell apart reflections from closely spaced scatterers. In some imaging applications, such as profilometry, it is *a priori* known that there is only a single scatterer. The relevant metric then is not resolution, but accuracy. The accuracy of an FMCW system can be much finer than its resolution, as described in section 2.1.3.5. We demonstrate this by measuring the profile of a United States $1 coin using the VCSEL-based optoelectronic SFL with a chirp bandwidth of 500 GHz at 1550 nm. The coin was mounted on a motorized two-dimensional translation stage. The light was collimated using a gradient-index (GRIN) lens with a beam diameter of 0.5 mm. The depth at a particular transverse location was determined by measuring the strongest photocurrent frequency in a Michelson interferometer with a balanced detector (figure 2.5). The measured profile is shown in figure 3.17. As expected, we were able to record features with depth variations that are much finer than the 0.3 mm axial resolution of a 500 GHz chirp.

3.6 Summary

In this chapter we described the design of the SCL-based optoelectronic SFL. We derived equations that govern its steady-state operation, and introduced an iterative predistortion procedure that relaxes constraints on the optoelectronic feedback and enables locking at high chirp rates. We discussed different SCL platforms and how they motivate the choice of an amplitude control element. We demonstrated closed-loop linear and arbitrary chirps and established the use of the optoelectronic SFL in reflectometry and profilometry applications.

In the next chapter we examine multiple source FMCW (MS-FMCW) reflectometry, a high-resolution optical ranging technique that is enabled by the starting frequency stability and chirp control of the optoelectronic SFL.

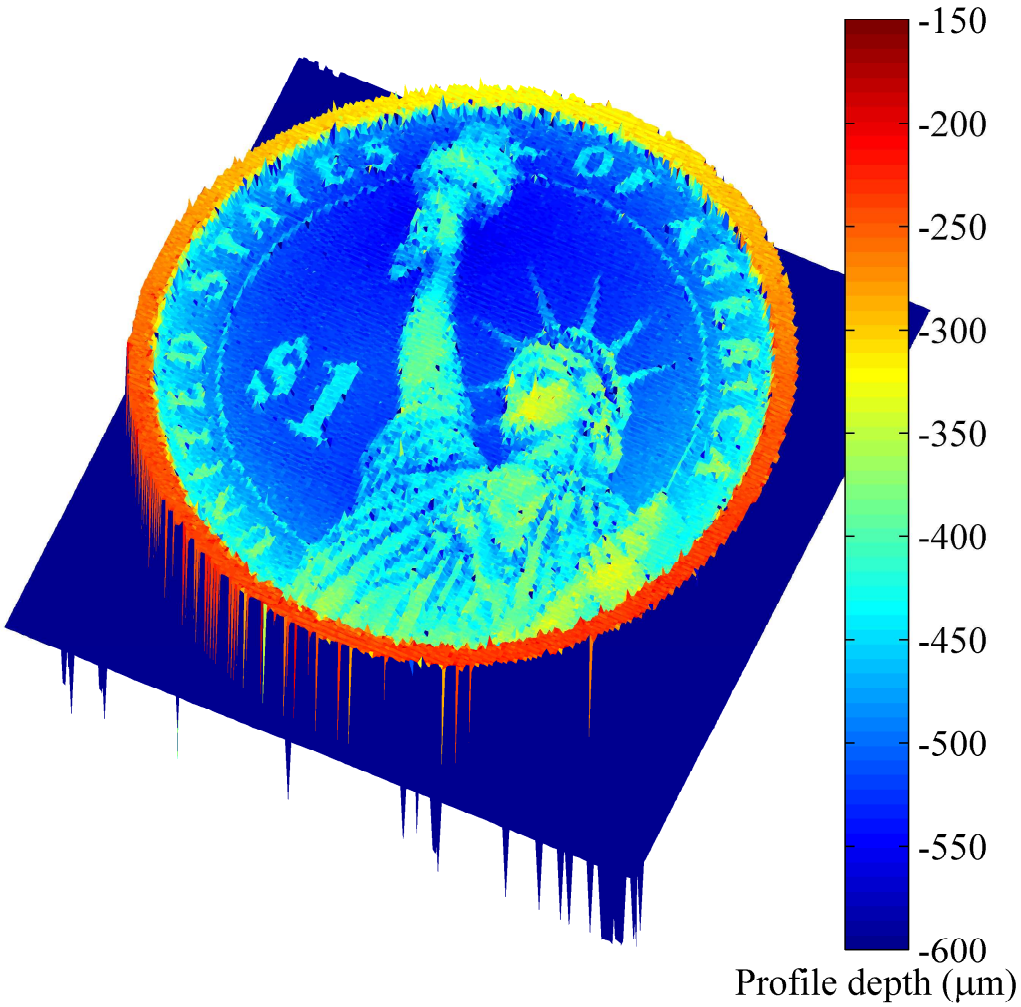

Figure 3.17: Depth profile of a United States $1 coin measured using the VCSEL-based optoelectronic SFL with a chirp bandwidth of 500 GHz and a wavelength of $\sim$ 1550 nm

Chapter 4

Multiple Source FMCW Reflectometry

4.1 Introduction

In this chapter we describe a novel approach aimed at increasing the effective bandwidth of a frequency-modulated continuous-wave (FMCW) ranging system. This is achieved by combining, or stitching, separate swept-frequency lasers (SFLs), to approximate a swept-source with an enhanced bandwidth [13, 14, 19]. The result is an improvement in the range resolution proportional to the increase in the swept-frequency range. This technique bears resemblance to synthetic aperture radar, in which radio frequency (RF) signals collected at multiple physical locations are used to approximate a large antenna aperture, and hence a high transverse resolution. In multiple source FMCW reflectometry, the synthesized aperture is not physical, but instead represents the accessible optical frequency range. This technique is of particular interest in the context of the SCL-based optoelectronic SFL. MS-FMCW leverages narrow SCL linewidths to present a pathway towards long-distance ranging systems with sub-100 μm resolutions.

We start our discussion of MS-FMCW by generalizing the results of chapter 2 to the case of multiple sources. We consider software and hardware implementations of stitching—the action of synthesizing a high-resolution range measurement from multiple source data sets—and present a series of experiments that demonstrate the

MS-FMCW principle. The culmination of this effort is a four-VCSEL system capable of ranging with an effective optical bandwidth of 2 THz, and a corresponding free-space axial resolution of 75 μm.

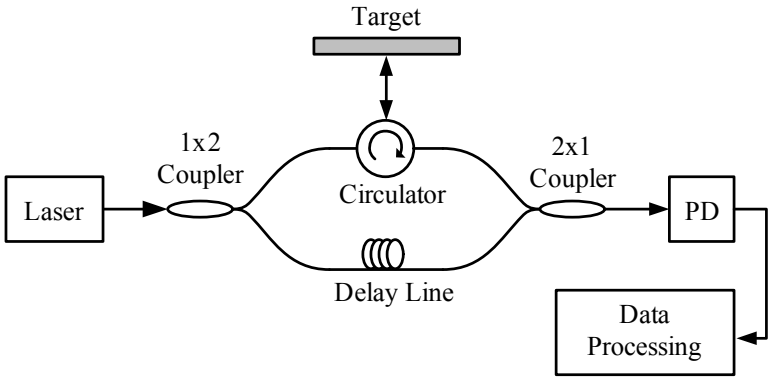

Figure 4.1: Schematic of an FMCW ranging experiment. PD: Photodetector

4.2 Theoretical Analysis

4.2.1 Review of FMCW Reflectometry

We begin our discussion with a brief review of FMCW reflectometry (see chapter 2 for a full discussion). Consider the FMCW ranging experiment shown in figure 4.1. The normalized electric field of the linearly chirped SFL is given by

$$e(t) = \text{rect}\left(\frac{t - T/2}{T}\right)\cos\left(\phi_0 + \omega_0 t + \frac{\xi t^2}{2}\right), \tag{4.1}$$

where T is the scan duration, ξ is the slope of the optical chirp, and ϕ_0 and ω_0 are the initial phase and frequency, respectively. The total frequency excursion is therefore given by $B = \xi T/2\pi$. For a single scatterer with round-trip delay τ and reflectivity R, the ω-domain photocurrent is given by

$$y(\omega) = \sqrt{R}\,\text{rect}\left(\frac{\omega - \omega_0 - \pi B}{2\pi B}\right)\cos\left(\omega\tau - \frac{\xi\tau^2}{2}\right). \tag{4.2}$$

The signal processing consists of calculating the Fourier transform (FT)[1] of $y(\omega)$ with respect to the variable ω, which yields a sinc peak centered at the delay τ.

$$Y(\zeta) = \pi B\sqrt{R}\,\exp\left(-j\frac{\xi\tau^2}{2}\right)\exp\left[-j(\zeta-\tau)(\omega_0+\pi B)\right]\mathrm{sinc}\left[\pi B(\zeta-\tau)\right], \qquad (4.3)$$

where ζ is the independent variable of the FT of $y(\omega)$, and has units of time. $Y(\zeta-\tau)$ is therefore the axial point spread function (PSF) of the FMCW system.

The range resolution is given by the location of the first null of the sinc function in equation (4.3) [37, 39]. This happens at $\zeta = \tau + 1/B$, which corresponds to a free-space range resolution

$$\Delta d = \frac{c}{2B}, \qquad (4.4)$$

where c is the speed of light. An equivalent metric of the resolution of the FMCW system is the full width at half maximum (FWHM) of the sinc function, given by

$$\mathrm{FWHM} \approx \frac{3.79}{\pi B} = \Delta d\frac{7.58}{\pi c} \qquad (4.5)$$

Let us now consider the following view of an FMCW imaging system. The target is characterized by some underlying function of the optical frequency, $y_{\mathrm{target}}(\omega)$, given by

$$y_{\mathrm{target}}(\omega) = \sum_n \sqrt{R_n}\cos\left(\omega\tau_n - \frac{\xi\tau_n^2}{2}\right), \qquad (4.6)$$

where τ_n and R_n are the delays and reflectivities of the multiple reflectors that make up the target. In deriving equation (4.6) we have assumed highly transparent reflectors ($R_n \ll 1$), and ignored interference between reflected beams. The FMCW photocurrent is then given by

$$y(\omega) = a(\omega)y_{\mathrm{target}}(\omega), \qquad (4.7)$$

where $a(\omega)$ is the rectangular window function, as in equation (4.2). The function

[1] In the following analysis we use capital letters to denote the FTs of the corresponding lower-case functions.

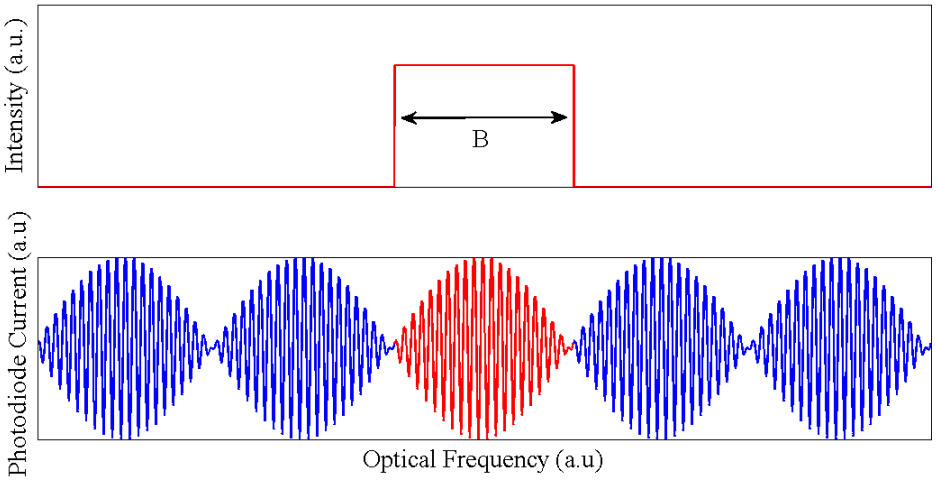

Figure 4.2: Schematic representation of single-source FMCW reflectometry. Top panel: the window function $a(\omega)$ corresponding to a single chirp. Bottom panel: The underlying target function $y_{\text{target}}(\omega)$ (blue) and its portion that is measured during the single sweep (red)

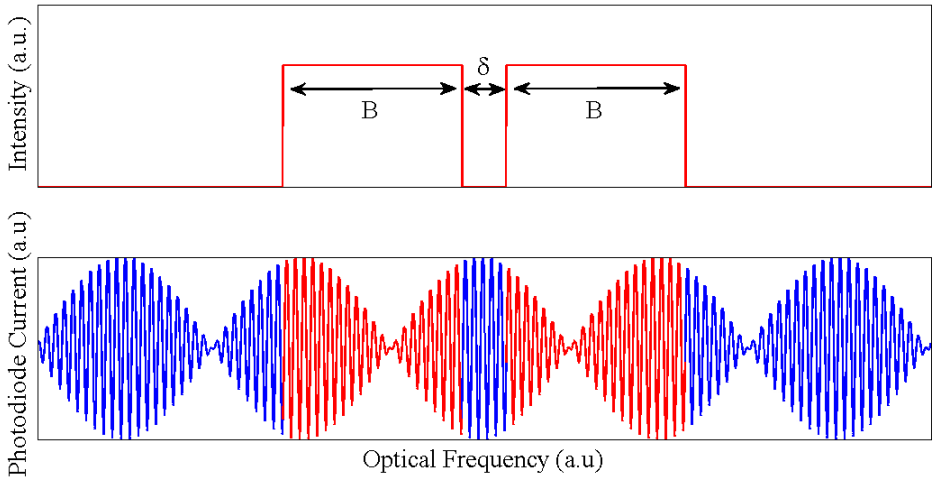

Figure 4.3: Schematic representation of dual-source FMCW reflectometry. Top panel: the window function $a(\omega)$ corresponding to two non-overlapping chirps. Bottom panel: The underlying target function $y_{\text{target}}(\omega)$ (blue) and its portion that is measured during the two sweeps (red)

$y_{\text{target}}(\omega)$ contains all the information about the target, and perfect resolution is obtained if $y_{\text{target}}(\omega)$ is known for all values of the optical frequency ω. The measurement in equation (4.7) gives us partial information about $y_{\text{target}}(\omega)$, collected over the frequency excursion defined by $a(\omega)$, resulting in a nonzero Δd. This single-source measurement is illustrated in figure 4.2.

We next develop the theory of MS-FMCW reflectometry, in which multiple sources sweep over distinct regions of the optical spectrum. The motivation for this approach is that the use of multiple sources allows us to further characterize $y_{\text{target}}(\omega)$. Figure 4.3 shows a schematic representation of a dual-source FMCW measurement. The target information is collected over a larger portion of the optical spectrum, resulting in an increase in the effective B, and a corresponding decrease in Δd.

4.2.2 Multiple Source Analysis

Taking the FT of equation (4.7), and equation (4.6), we arrive at the expression

$$Y(\zeta) = \frac{1}{2}\sum_n \sqrt{R_n}\exp\left(-j\frac{\xi\tau_n^2}{2}\right)A(\zeta-\tau_n), \tag{4.8}$$

which has peaks at $\zeta = \tau_n$. The axial PSF (i.e., the shape of the peaks) is given by the FT $A(\zeta)$ of the window function $a(\omega)$. We model the use of multiple sources with a window function $a_N(\omega)$ that comprises N non-overlapping rectangular sections, as shown in the top panel of figure 4.4a. The approach is easily modified to include overlapping sections. The k-th sweep originates at $\omega_{0,\,k}$, and is characterized by an angular frequency excursion $2\pi B_k$, where $k = 1, \ldots, N$. As illustrated in the middle and bottom panels of figure 4.4a, $a_N(\omega)$ can be decomposed into a rectangular window with width $2\pi\tilde{B} \equiv 2\pi\left[\sum_{k=1}^{N} B_k + \sum_{k=1}^{N-1}\delta_k\right]$, and a set of thin rectangular sections (gaps). Each gap represents the frequency range $2\pi\delta_k$ between the end of the k-th sweep and the beginning of the (k+1)-th sweep, across which no photocurrent is measured. Amplitudes of the ζ-domain FTs of the functions in figure 4.4a are shown in figure 4.4b. We observe that if the gaps are chosen sufficiently small, their effect in the ζ-domain can be treated as a small perturbation of the single sweep of

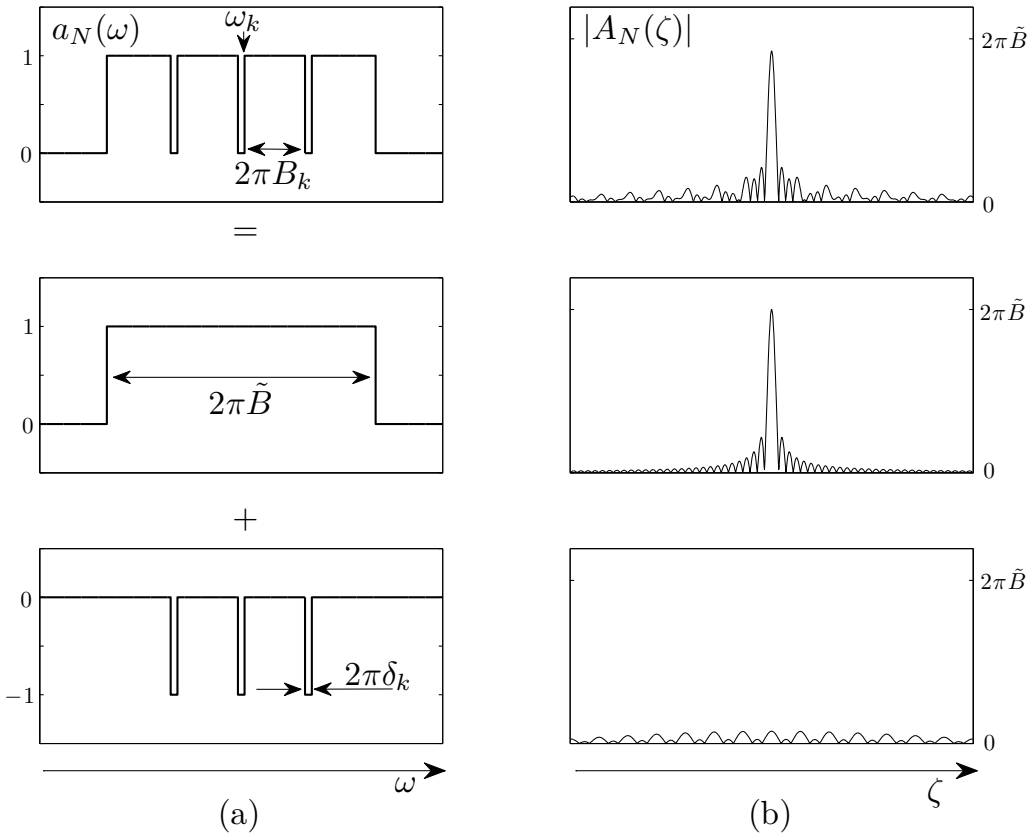

Figure 4.4: Multiple source model. (a)ω-domain description. The top panel shows a multiple source window function $a_N(\omega)$. This function may be decomposed into the sum of a single-source window function (middle panel) and a function that describes the inter-sweep gaps (bottom panel). (b)ζ-domain description. The three figures show the amplitudes of the ζ-domain FTs of the corresponding functions from part (a).

bandwidth $2\pi\tilde{B}$.

Therefore, an N-source sweep is described by

$$a_N(\omega) = \text{rect}\left(\frac{\omega - \omega_{0,1} - \pi\tilde{B}}{2\pi\tilde{B}}\right) - \sum_{k=1}^{N-1} \text{rect}\left(\frac{\omega - \omega_{0,\,k+1} + \pi\delta_k}{2\pi\delta_k}\right) \tag{4.9}$$

in the ω-domain, and by

$$\begin{aligned} A_N(\zeta) = {} & 2\pi\tilde{B}\exp\left[-j\zeta(\omega_{0,1} + \pi\tilde{B})\right]\text{sinc}\left(\zeta\tilde{B}\right) \\ & - 2\pi\sum_{k=1}^{N-1}\delta_k \exp\left[-j\zeta\left(\omega_{0,\,k+1} - \pi\delta_k\right)\right]\text{sinc}(\zeta\delta_k) \end{aligned} \tag{4.10}$$

in the ζ-domain. To find the range resolution we find the first null of equation (4.10). Expanding near $\zeta = 1/\tilde{B}$ and using the approximation $\sum_{k=1}^{N-1}\delta_k \ll \sum_{k=1}^{N} B_k$ yields

$$\zeta_{\text{null}}^{-1} = \left|\tilde{B}\exp\left[-j\zeta_{\text{null}}(\omega_{0,1} + \pi\tilde{B})\right] + \sum_{k=1}^{N-1}\delta_k\exp\left[-j\zeta_{\text{null}}\left(\omega_{0,k+1} - \pi\delta_k\right)\right]\right|. \tag{4.11}$$

Equation (4.11) can be solved numerically to find ζ_{null}. We note that an upper bound on ζ_{null}, and consequently on the range resolution, may be obtained by applying the triangle inequality to equation (4.11), to yield

$$\Delta d_{\text{MS-FMCW}} \leq \frac{c}{2\sum_{k=1}^{N} B_k}. \tag{4.12}$$

The conclusion is that by sweeping over distinct regions of the optical spectrum, we collect enough information about the target to arrive at an range resolution equivalent to the total traversed optical bandwidth, provided that the said bandwidth is much greater than the inter-sweep gaps.

4.2.3 Stitching

We next consider the problem of stitching, that is, synthesizing a measurement with enhanced resolution using photocurrents collected from multiple sweeps. In the pre-

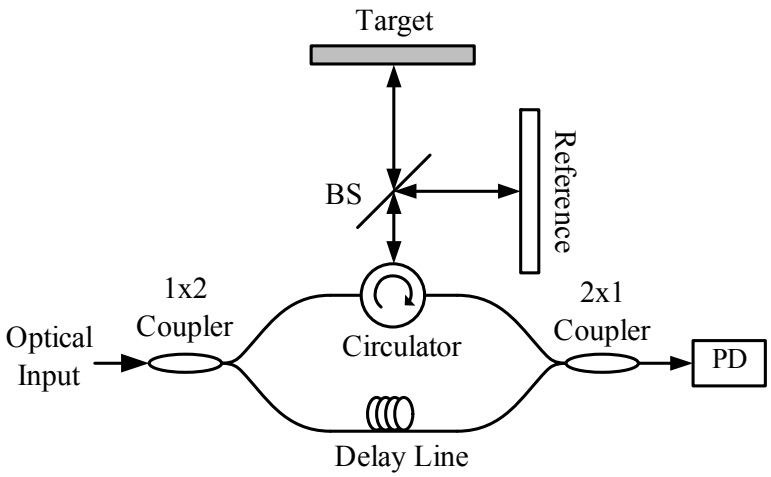

Figure 4.5: Schematic of a multiple source FMCW ranging experiment. A reference target is imaged along with the target of interest, so that the inter-sweep gaps may be recovered. BS: Beamsplitter. PD: Photodetector

ceding sections we have mapped photocurrents from the time domain to the optical frequency domain. Since the optical frequency is linear in time, this mapping involves first scaling the time axis by the chirp slope, and then translating the data to the correct initial frequency. Whereas the rate of each chirp is precisely controlled [1], the starting sweep frequencies are not known with sufficient accuracy. To reflect this uncertainty, we omit the translation step, so that the data collected during the k-th scan is given by

$$y_k(\omega) = \text{rect}\left(\frac{\omega - \pi B_k}{2\pi B_k}\right) y_{\text{target}}(\omega + \omega_{0,k}). \tag{4.13}$$

The stitched measurement, given by $y_{\text{stitched}} = a_N(\omega) y_{\text{target}}(\omega)$, can be written in terms of functions $y_k(\omega)$ using equation (4.9):

$$y_{\text{stitched}}(\omega) = \sum_{k=1}^{N} y_k(\omega - \omega_{0,k}). \tag{4.14}$$

The magnitude of the FT of equation (4.14) may be used for target recognition, and is given by

$$|Y_{\text{stitched}}(\zeta)| = \left| \sum_{k=1}^{N} \exp\left[-j2\pi\zeta \sum_{l=1}^{k-1} (B_l + \delta_l)\right] Y_k(\zeta) \right|. \tag{4.15}$$

The uncertainty in the starting frequencies manifests itself as an uncertainty in the inter-sweep gaps. To recover the gaps, we use a known reference target along with the target of interest, as shown in figure 4.5. By analyzing the data collected from the reference target, we are able to extract the parameters δ_k, and stitch together the target of interest measurement, according to equation (4.15).

To develop a gap recovery algorithm, we examine a two-sweep system with a single gap δ. The case of more than two sources may then be treated by applying this algorithm to adjacent sweeps in a pairwise manner. For simplicity we consider sweeps of equal slopes ξ, durations T, and therefore, bandwidths B. Suppose the known reference target consists of a single reflector with reflectivity R_a, located at the delay τ_a. The experiment of figure 4.5 generates two photocurrents, one for each sweep, of the form of equation (4.2). The initial photocurrent phase depends on the starting frequency of the corresponding sweep, and will change as the inter-sweep gap varies. Therefore, by considering the phase difference between the two photocurrents, we can calculate the value of the gap. Formally, let us evaluate the FT of the k-th photocurrent, at the maximum of the reference target peak. Using equation (4.6) and equation (4.13),

$$Y_k(\tau_a) = \pi B_k R_a \exp\left[-j\xi\tfrac{\tau_a^2}{2} + j\omega_{0,k}\tau_a\right], \quad k = 1, 2. \tag{4.16}$$

The ratio of the two expressions in equation (4.16) yields the phase difference between the photocurrents:

$$\psi_a \equiv \frac{Y_1(\tau_a)}{Y_2(\tau_a)} = \exp\left[-j2\pi\tau_a(B+\delta)\right]. \tag{4.17}$$

Given the reference reflector delay τ_a and the frequency excursion B, the gap may be found using

$$\arg\left[\exp(j2\pi\tau_a B)\psi_a\right] = -2\pi\tau_a\delta. \tag{4.18}$$

The phase of a complex number can only be extracted modulo 2π, so that equation (4.18) can only be used to recover δ with an ambiguity of $1/\tau_a$. Therefore, the gap needs to be known to within $1/\tau_a$ before equation (4.18) may be applied. Using a

grating-based optical spectrum analyzer would yield the gap value with an accuracy of a few GHz, and we therefore need $1/\tau_a \gtrsim 10$ GHz. The nonzero linewidth of the source generates errors in the phase measurement ψ_a in equation (4.17) (see section 2.1.3.4). According to equation (4.18), the corresponding error in the gap calculation is inversely proportional to τ_a, and a large τ_a is therefore necessary to calculate δ accurately.

To overcome this issue, we use two reflectors τ_a and τ_b, and express the gap size as a function of the reflector separation. We define two phase factors

$$\psi_n \equiv \frac{Y_1(\tau_n)}{Y_2(\tau_n)}, \quad n = a, b \tag{4.19}$$

and calculate the two reflector-analog of equation (4.18):

$$\arg\left\{\exp\left[j2\pi(\tau_a - \tau_b)B\right]\frac{\psi_a}{\psi_b}\right\} = -2\pi(\tau_a - \tau_b)\delta. \tag{4.20}$$

From equation (4.20), $1/|\tau_a - \tau_b|$ can be chosen to be > 10 GHz to determine the value of δ. The error in this calculation is proportional to $1/|\tau_a - \tau_b|$. The accuracy of the gap calculation can now be improved by using equation (4.18), which yields a new value of δ with a lower error proportional to $1/\tau_a$. Depending on system noise levels, more stages of evaluation of δ using more than two reference reflectors may be utilized to achieve better accuracy in the calculations.

A potential MS-FMCW system architecture employing the stitching technique is shown in figure 4.6. The optical sources are multiplexed and used to image a target and a reference, as discussed above. The optical output is demultiplexed and measured using a set of photodetectors to generate the photocurrents of equation (4.13). The reference data is processed and used to stitch a target measurement with improved resolution. The multiplexing may be performed in time or optical frequency, or a combination of the two. The real power of the MS-FMCW technique then lies in its scalability. One envisions a system that combines cheap off-the-shelf SCLs to generate a swept-frequency ranging measurement that features an excellent

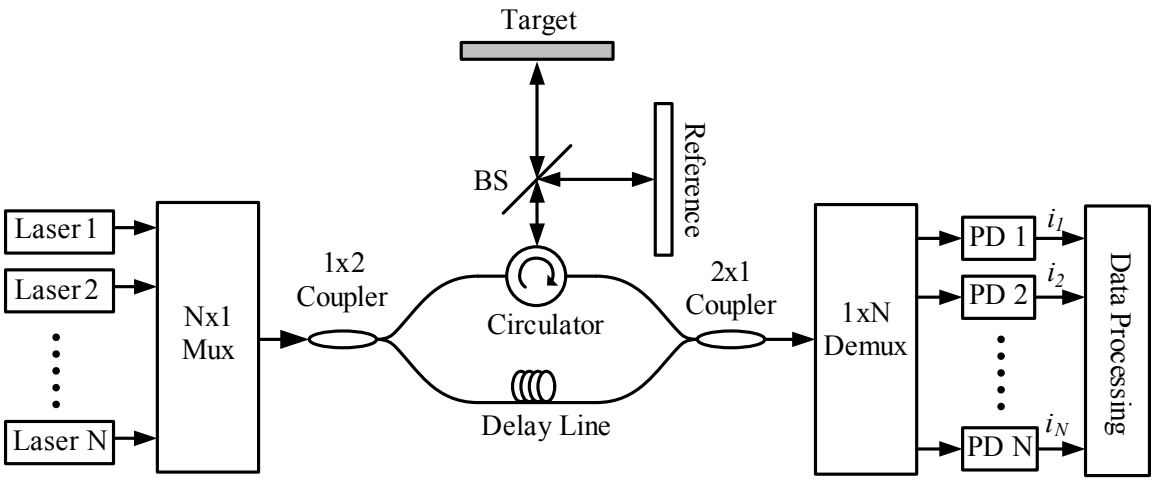

Figure 4.6: Proposed multiple source FMCW system architecture. BS: Beamsplitter. PD: Photodetector

combination of range resolution, scan speed, and imaging depth.

4.3 Experimental Demonstrations

4.3.1 Stitching of Temperature-Tuned DFB Laser Sweeps

Our first demonstration of the MS-FMCW technique was based on a 1550 nm DFB optoelectronic SFL (see chapter 3). The source generated a highly linear chirp with a bandwidth of 100 GHz and a scan time of 1 ms. We used the configuration of figure 4.5 with a two reflector reference characterized by $1/|\tau_a - \tau_b| \sim 10$ GHz (~ 3 cm free-space separation). This reference was chosen to accommodate the accuracy with which the gaps are initially known (~ 1 GHz). We tuned the SCL temperature through two set points to generate two 100 GHz sweeps with different starting frequencies. Optical spectra of the two sweeps (blue and red) are shown in figure 4.7. Even though it looks like the sweeps have significant overlap in optical frequency, the end of one is actually aligned to the beginning of the other. The perceived overlap is due to the nonzero width of the analyzer PSF, shown in black.

These sweeps were launched sequentially into the experiment, and the corresponding photocurrents were recorded. Applying the two-step procedure described in sec-

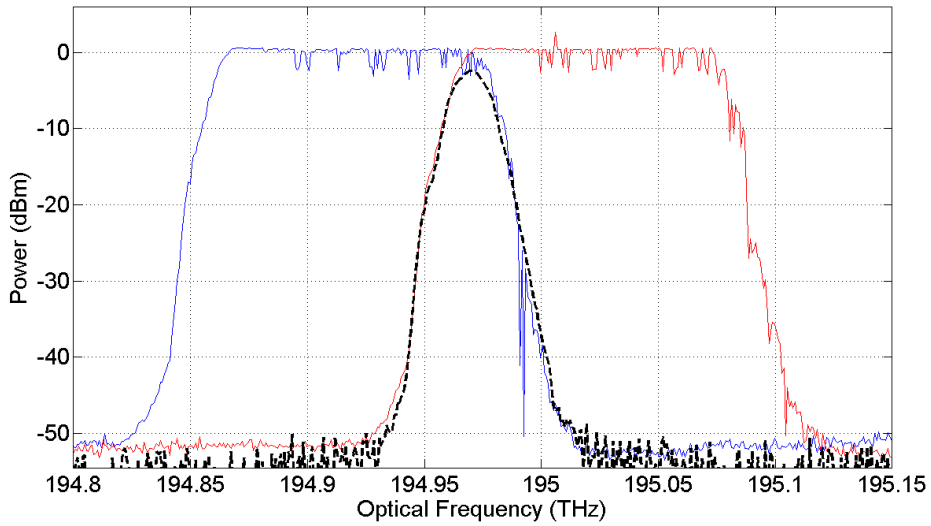

Figure 4.7: Optical spectra of the two DFB sweeps (blue and red) and the optical spectrum analyzer PSF (black)

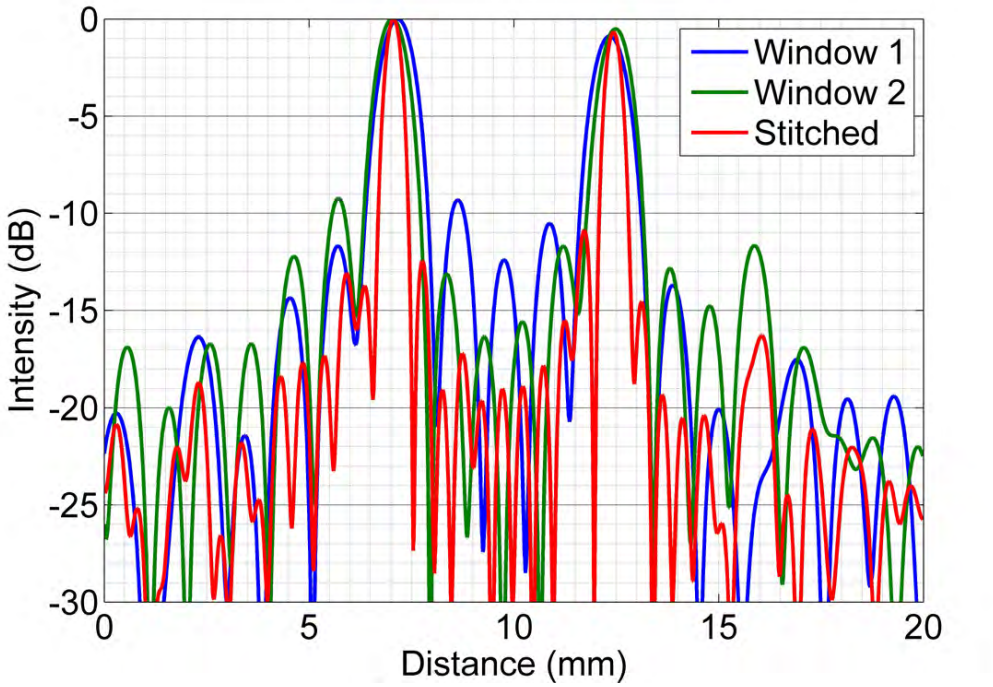

Figure 4.8: Single-sweep and stitched two-sweep photocurrent spectra of a dual reflector target with a separation of 5.44 mm. No apodization was used.

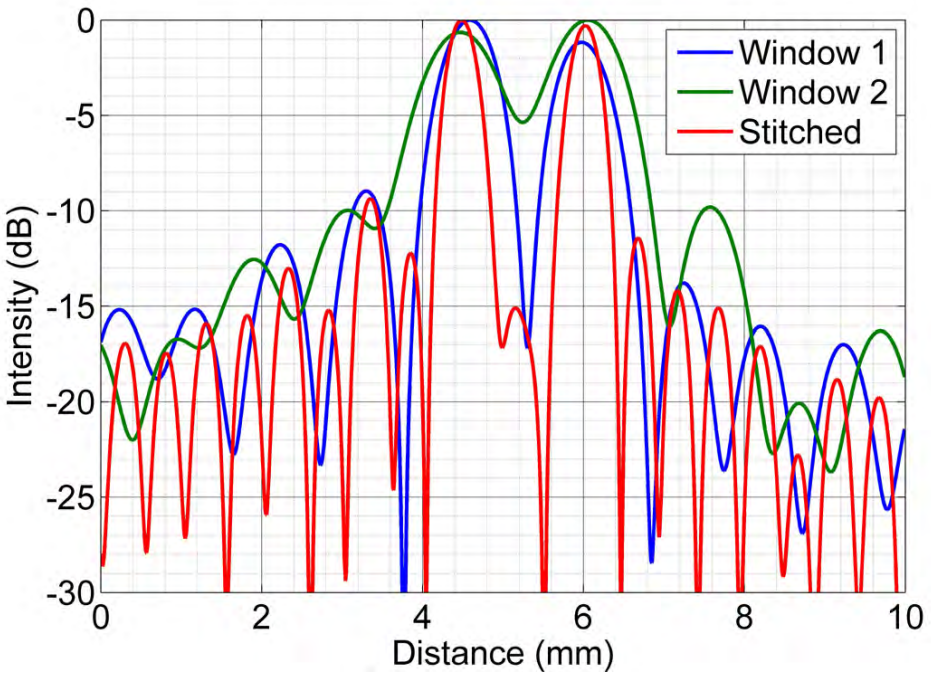

Figure 4.9: Single-sweep and stitched two-sweep photocurrent spectra of a dual reflector target with a separation of 1.49 mm. No apodization was used.

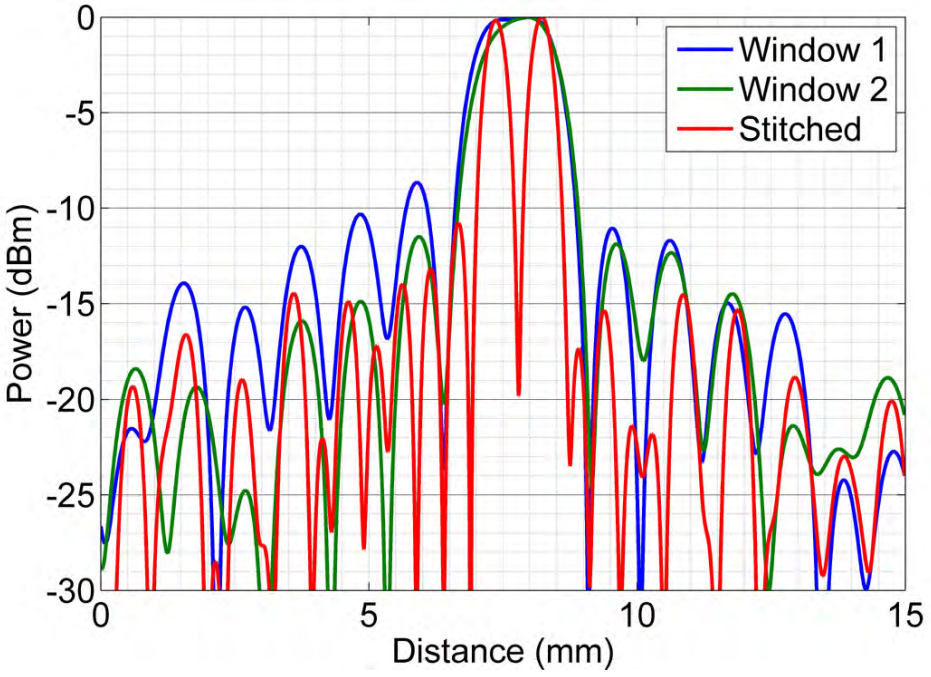

Figure 4.10: Single-sweep and stitched two-sweep photocurrent spectra of a dual reflector target with a separation of 1.00 mm (a microscope slide). No apodization was used.

tion 4.2.3, we recovered the gaps, and stitched the photocurrent spectra using equation (4.15). To characterize the range resolution of the system, we imaged slabs of transparent material (acrylic and glass). Reflections from the two slab interfaces were recorded for three slab thicknesses: 5.44 mm, 1.49 mm, and 1.00 mm (glass microscope slide). Figure 4.8, figure 4.9, and figure 4.10 show the ζ-domain photocurrent spectra for the three cases. The x-axis has been rescaled to correspond to distance in a material with refractive index 1.5, i.e., acrylic and glass. Each of the three figures shows the single-sweep spectra (blue and green), as well as the stitched spectrum (red). The FWHM of the peaks in the stitched plots is half of the FWHM of the peaks in the single-sweep plots, as predicted by equation (4.5). Figure 4.10 is of particular interest because the two peaks in the single-scan spectrum, corresponding to reflections from the two microscope slide facets, are barely resolved. This is consistent with the theoretical range resolution in glass of 1 mm for a 100 GHz sweep. The stitched curve shows two prominent peaks, demonstrating our improved ability to resolve two closely spaced targets.

By using more aggressive temperature and current tuning, we were able to extend the number of sweeps to three, and observe a threefold improvement in range resolution. The single-scan and stitched photocurrent spectra of a single reflector are shown in figure 4.11a. The single reflector spectra allows us to reliably measure the improvement in the FWHM of the axial PSF. The FWHMs are 12.17 ps and 4.05 ps for the single and multiple source cases, respectively. Using equation (4.5) we calculate the free-space range resolutions to be 1.51 mm and 500 μm. The threefold range resolution enhancement is consistent with equation (4.12). The improvement in resolution again allows us to resolve the two reflections from the 1 mm glass microscope slide in figure 4.11b. The measured peak separation of 10 ps is the round-trip delay between the two slide facets, and indeed corresponds to a glass thickness of 1 mm.

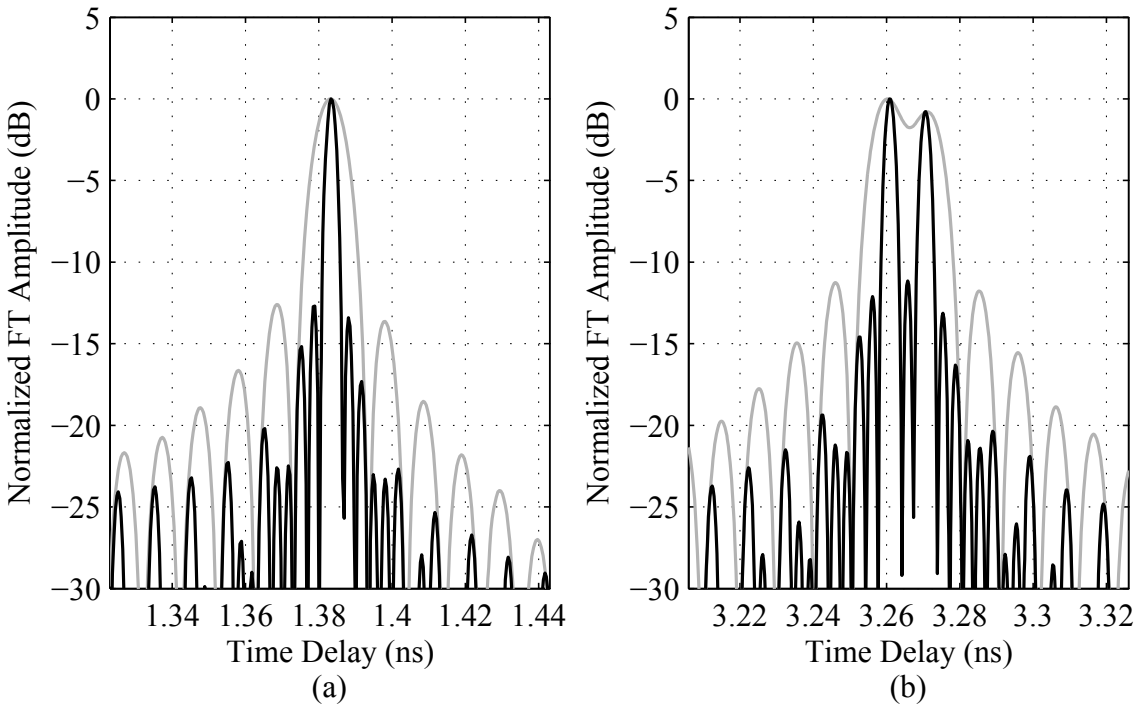

Figure 4.11: The gray and black curves correspond to single-sweep and stitched three-sweep photocurrent spectra, respectively. No apodization was used. (a) Single reflector spectrum. (b) Glass slide spectrum. The peaks correspond to reflections from the two air-glass interfaces. The slide thickness is 1 mm.

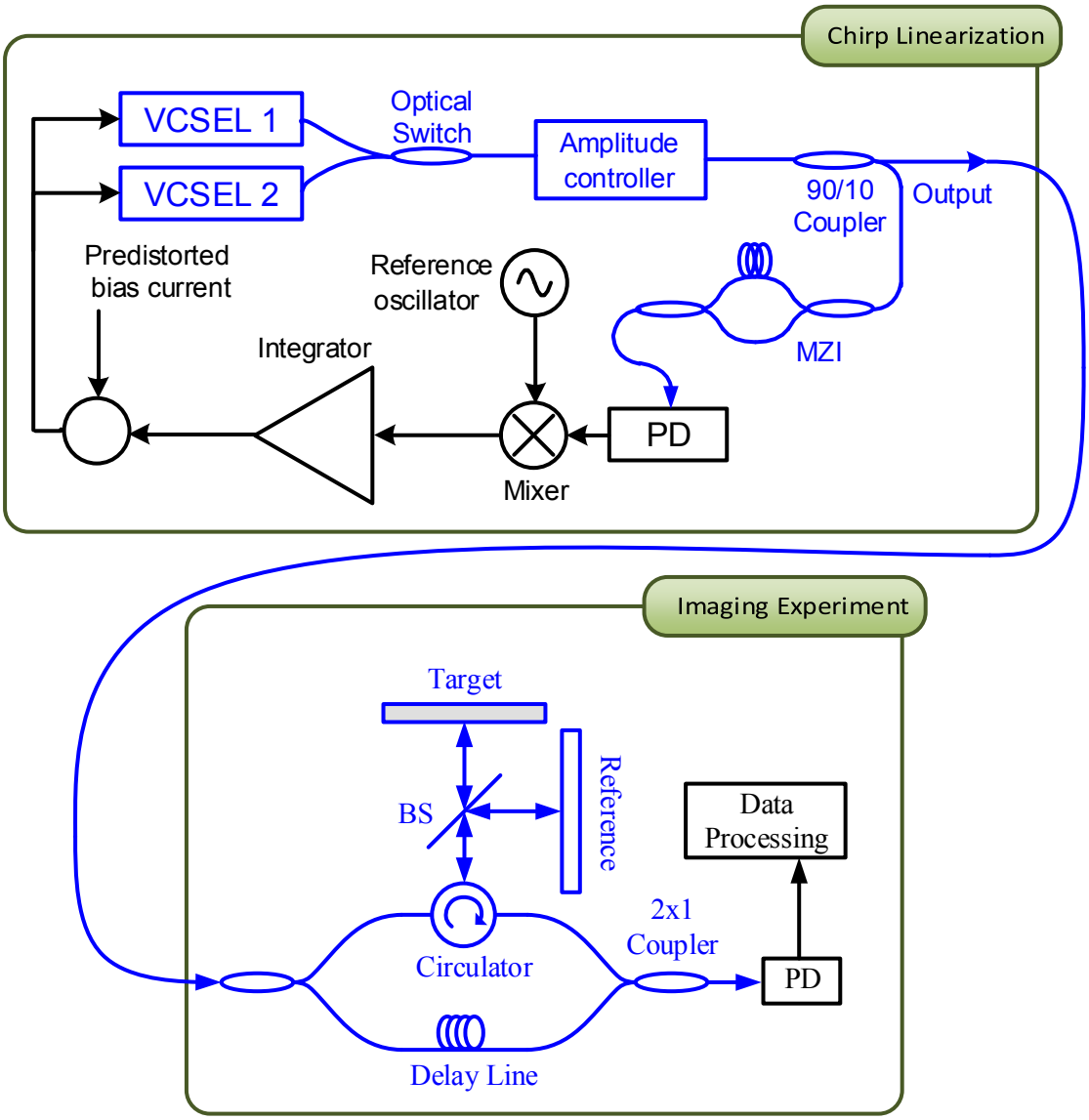

Figure 4.12: Dual VCSEL FMCW reflectometry system diagram. The feedback loop ensures chirp stability. A reference target is used to extract the inter-sweep gaps. PD: Photodiode, BS: Beamsplitter

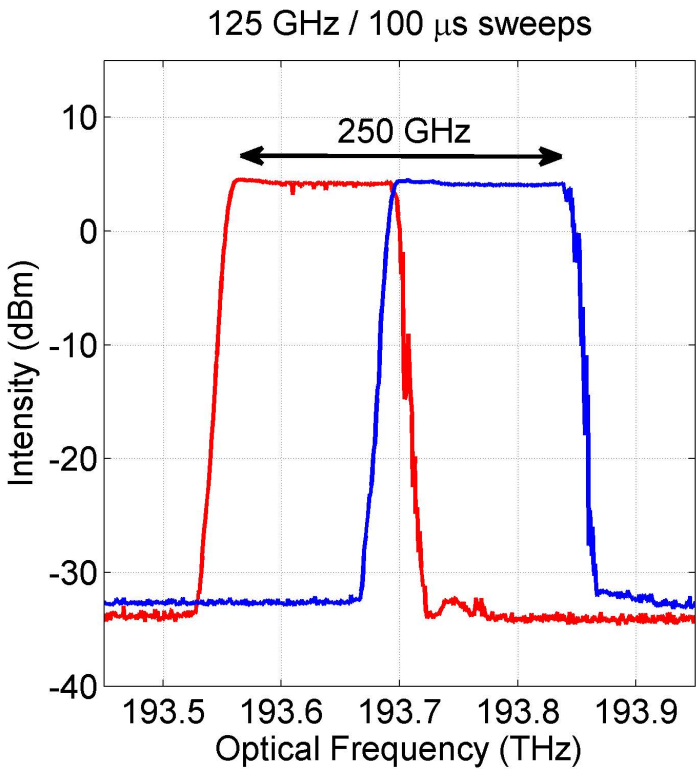

Figure 4.13: Optical spectra of the two VCSEL sweeps in the 250 GHz experiment

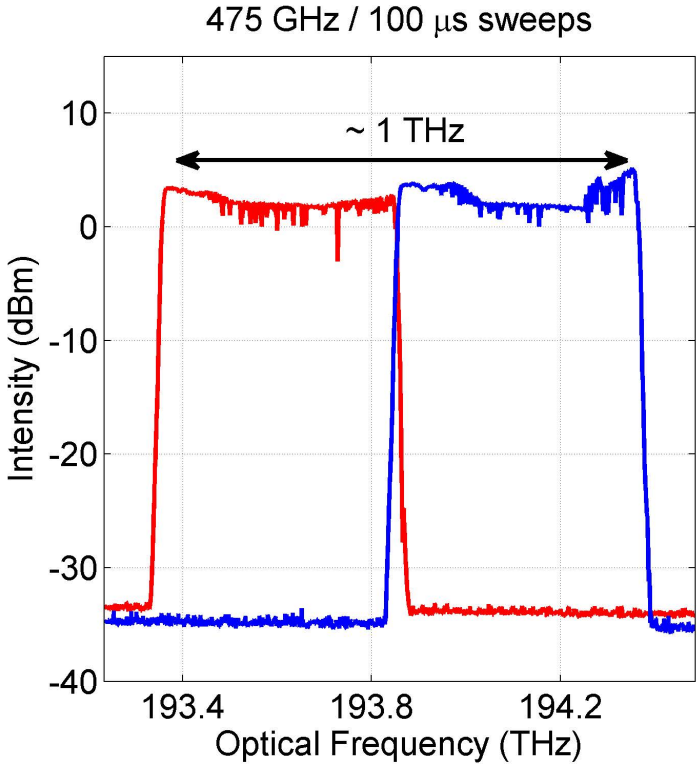

Figure 4.14: Optical spectra of the two VCSEL sweeps in the ~ 1 THz experiment

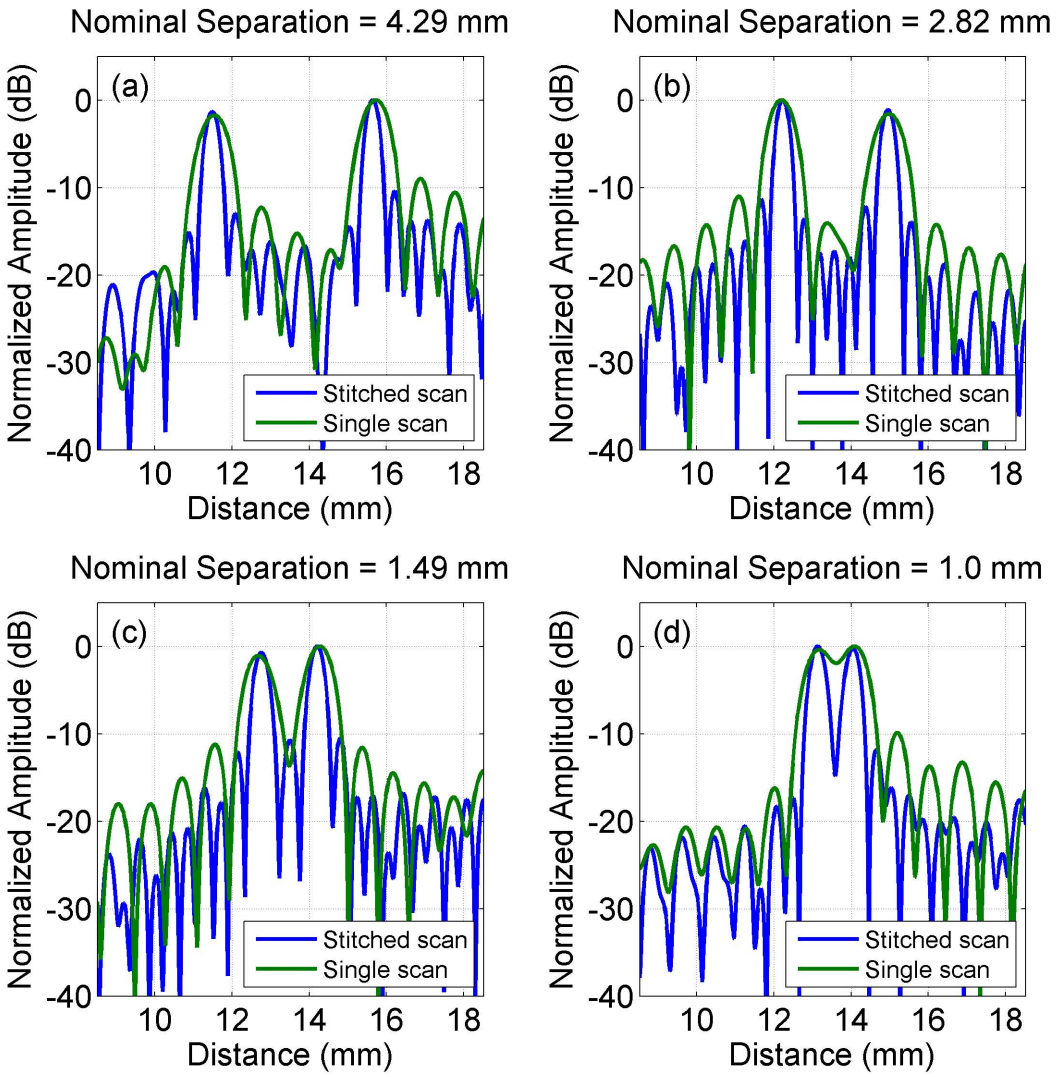

Figure 4.15: Single-sweep and stitched two-sweep photocurrent spectra of dual reflector targets with various separations. The total chirp bandwidth is 250 GHz. No apodization was used.

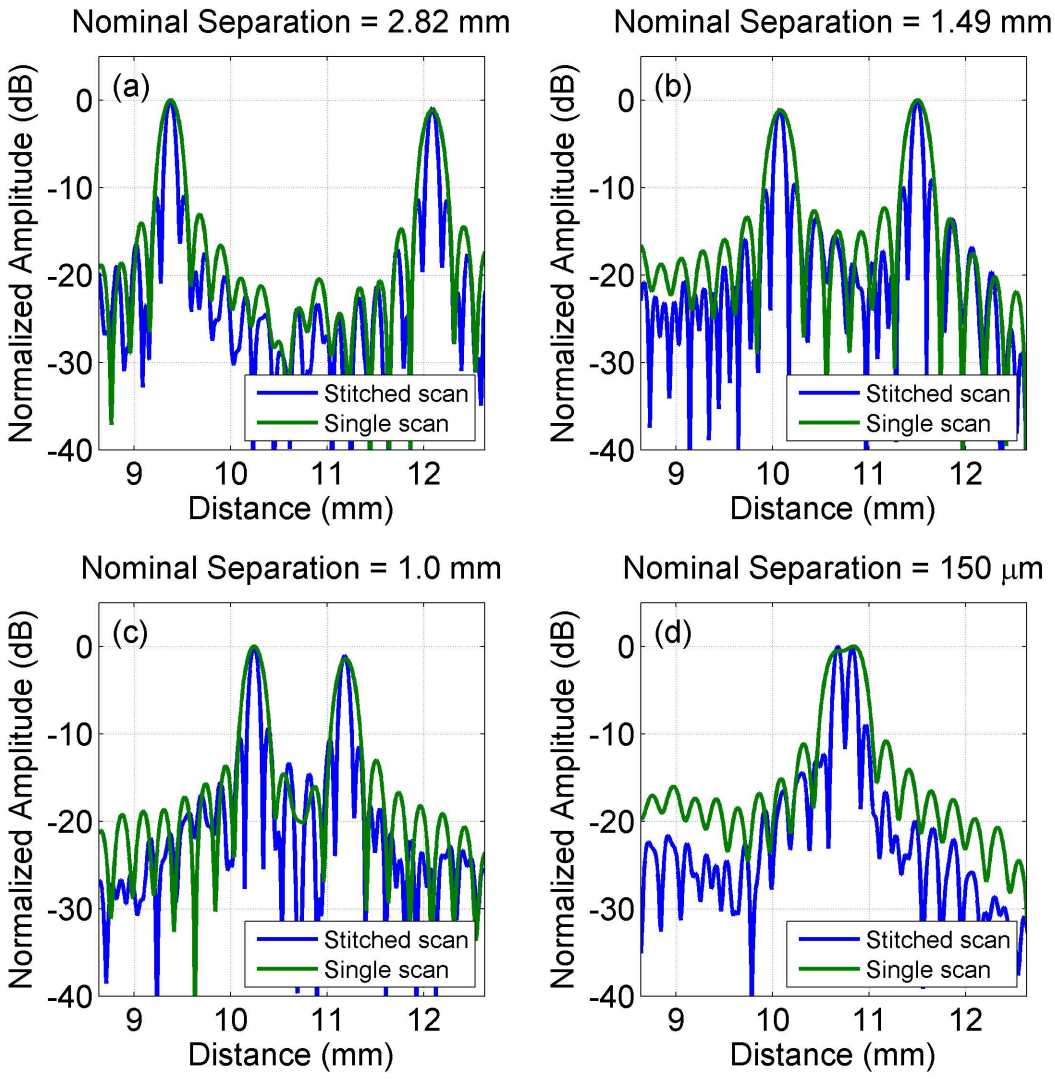

Figure 4.16: Single-sweep and stitched two-sweep photocurrent spectra of dual reflector targets with various separations. The total chirp bandwidth is ~ 1 THz. No apodization was used.

4.3.2 Stitching of Two VCSELs

In the current section we describe the next phase of our MS-FMCW experiments—the stitching of two commercial VCSELs at 1550 nm. When compared to DFB lasers, VCSELs offer increased tunability, a faster chirp rate, as well as a significant cost reduction (see section 3.3.1).

In the proof-of-principle DFB experiment we used a single laser and tuned its temperature through multiple setpoints to generate up to three sweeps. The SCL temperatures needed to equilibrate before data collection, and as a result, the system scan time was about ten minutes. In this experiment, we used two VCSELs and an optomechanical switch in a feedback loop to form an optoelectronic SFL, as shown in figure 4.12. The switch selects a particular VCSEL, and the feedback imposes a perfectly linear chirp. Each VCSEL completed its chirp in 100 μs, but the total scan time was limited by the switch to about 20 ms.

We started our experiment with conservative tuning of 125 GHz per channel. The temperatures of the VCSELs were tuned to align their optical spectra to each other, as shown in figure 4.13. As before, we included a reference target to aid in the gap recovery procedure. Figure 4.15 compares single-source and stitched axial scans of acrylic and glass slabs of varying thicknesses. As expected, the stitched scans have a higher axial resolution, as evidenced by both the reduced FWHM of the axial PSF, as well as our ability to resolve the surfaces of the 1 mm glass slide in figure 4.15d.

We continued our experiment with more aggressive temperature and current tuning, which yielded 475 GHz of optical bandwidth per channel, with a total chirp bandwidth of just under 1 THz, as shown in figure 4.14. This bandwidth corresponds to a free-space axial resolution of $\sim$ 150 μm, and a glass resolution of $\sim$ 100 μm. Two-target axial scans are shown in figure 4.16. As before, stitching the photocurrents narrowed the axial PSF. The thinnest target we used was a glass microscope coverslip with a nominal thickness of 150 μm, which showed up as a single broad peak in the single sweep, but was resolved into two reflections in the stitched scan.

4.3.3 Hardware Stitching of Four VCSELs

Previous stitching experiments relied on a simultaneous measurement of a multi-reflector reference target to determine the inter-sweep gaps. Our next stitching experiment relied on the optoelectronic SFL to control the starting sweep frequencies of each channel. We used four 1550 nm VCSEL-based optoelectronic SFLs in the configuration of figure 4.17. The electric fields of each channel were added using a 4×1 fiber coupler. Each VCSEL was chirped 500 GHz in 100 μs, and then turned off. We allocated 25 μs between adjacent channel time slots to allow the previous laser to turn off, and the next laser to turn on. The total scan time was therefore 500 μs.

As described in section 3.2.2, locked states of the optoelectronic SFL form a family of linear chirps, separated by the loop MZI FSR in optical frequency. These locked states are shown schematically in red in figure 4.19. A locked SFL (shown in black) aligns itself to the state that most closely matches its free-running chirp. Tuning the SCL temperature and initial sweep current can therefore be used to shift the SFL to a particular locked state. We used an MZI with a relatively large FSR of 9.6 GHz to lock the VCSELs. As a result, the SFLs locked to the same state from scan to scan, generating precisely repeatable linear chirps. Moreover, because the SFLs used the same MZI, it was possible to tune all four channels to the same locked state, as shown in the blue curve in figure 4.19.

The combination of repeatable chirps and the ability to lock the SFLs to the same chirped state obviates the gap recovery procedure that was necessary in previous iterations of our MS-FMCW systems. The stitching is therefore essentially performed by the SFL hardware, which enables real-time processing of the MS-FMCW photocurrents. We used a coarse 80.2 GHz FSR MZI to tune the SCL temperatures and ensure that the SFLs are locked to the same chirped state. This MZI was used purely for calibration at start-up, and the acquisition of the coarse MZI signal was not necessary to process the MS-FMCW measurement.

Each channel in the hardware stitching system generated a 500 GHz sweep, for a total chirp bandwidth of 2 THz, as shown in figure 4.18. This corresponds to a

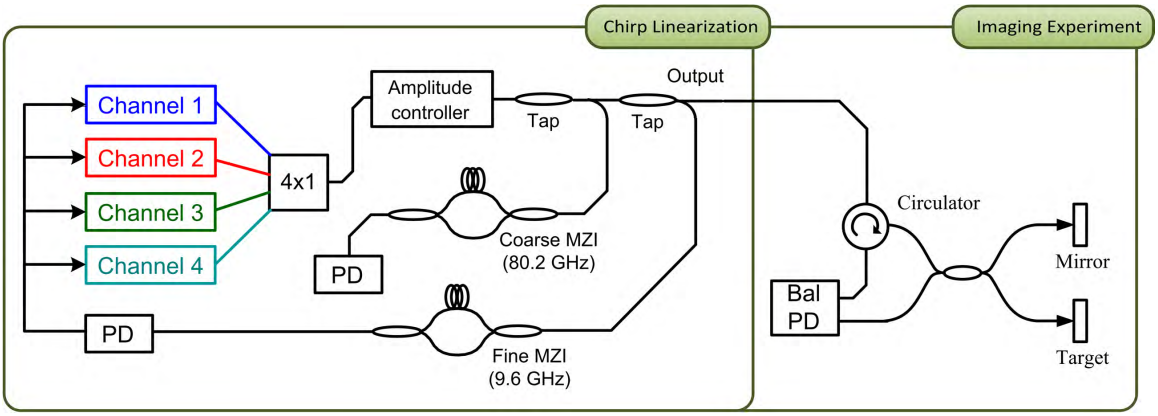

Figure 4.17: Four channel 2 THz hardware stitching experiment

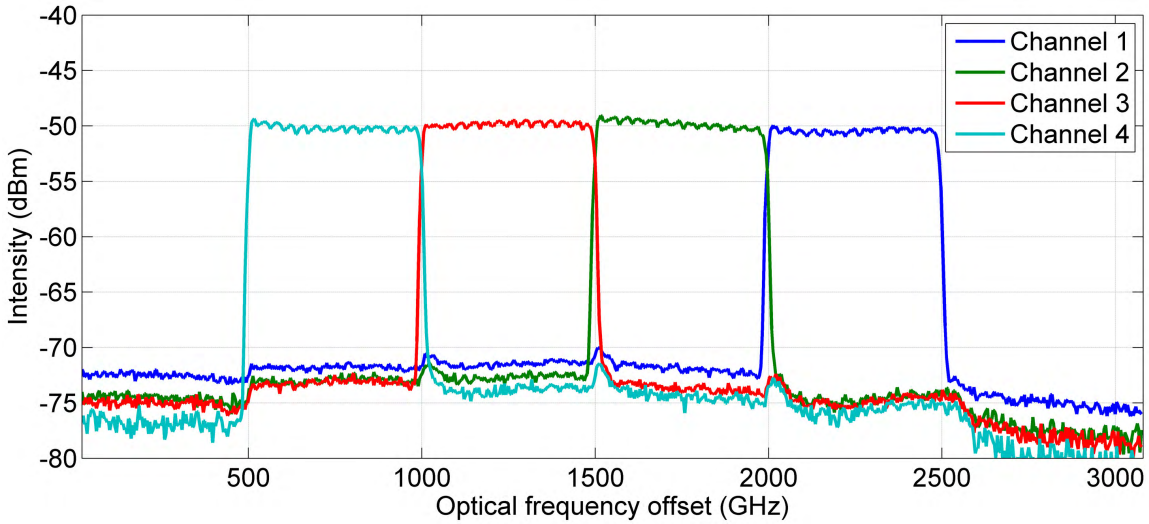

Figure 4.18: Optical spectra of the four 1550 nm VCSEL sweeps in the 2 THz hardware stitching experiment

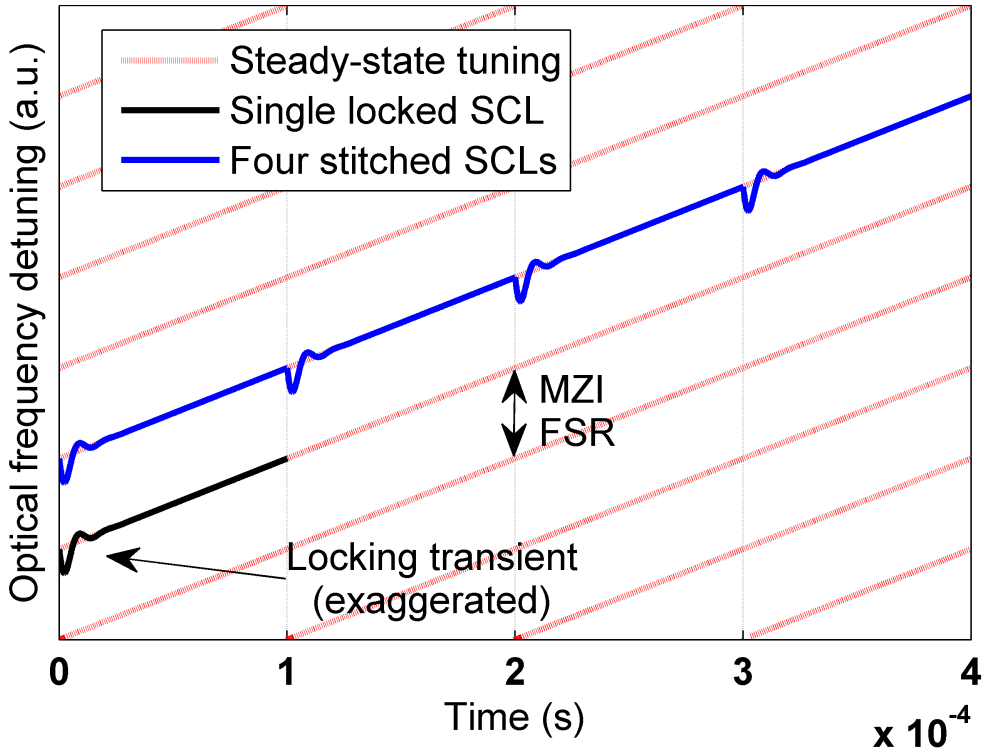

Figure 4.19: Schematic representation of a family of locked states (red) of the opto-electronic SFL. In lock, the SCL (black) follows the locked state that most closely matches its free-running chirp. In hardware stitching, temperatures and currents are tuned so that all the MS-FMCW channels operate in the same locked state (blue).

range resolution of 75 μm in free space, and 50 μm in glass. We imaged a 150 μm glass microscope coverslip that was suspended above a metal surface. The time-domain stitched photocurrent is shown in the top panel of figure 4.20. The curve was generated by measuring the photocurrent during each channel's time slot, and appending the four data sets to each other. The SFL hardware enables perfect real-time stitching, and we therefore observe a continuous time-domain curve. Single-sweep (black) and stitched (red) photocurrent spectra are shown in the bottom panel of figure 4.20. The x-axis is scaled to correspond to distance in glass. The time-domain photocurrents were apodized with a Hamming window before calculating the FT. The windowing suppressed the sinc sidebands seen in previously calculated photocurrent spectra, at the cost of broadening the PSF by a factor of 1.37. The Hamming-broadened glass resolutions are therefore 274 μm for the single-sweep, and 68.5 μm for the stitched measurement.

In the single-sweep photocurrent spectrum we observe two broad peaks, one due to reflections from the coverslip, and the other one due to a reflection from the metal surface underneath. In the stitched spectrum, the front and back coverslip surfaces are perfectly resolved, and the peak due to the metal surface is narrowed by a factor of four.

4.4 Summary

We have analyzed and demonstrated a novel variant of the FMCW optical imaging technique. This method combines multiple lasers that sweep over distinct but adjacent regions of the optical spectrum, in order to record a measurement with increased effective optical bandwidth and a corresponding improvement in the range resolution. The MS-FMCW technique is highly scalable and is a promising approach to realize a wide-bandwidth swept-frequency imaging system that inherits the speed and coherence of the SCL.

We have described the various phases of our experimental work on MS-FMCW. We started with a single DFB proof-of-concept experiment that relied on temperature tuning to generate three sweeps of 100 GHz each, for a total chirped bandwidth of 300 GHz. Because the laser temperature had to equilibrate between sweeps, the system scan time was about 10 minutes. We then moved on to a two-source VCSEL-based system with a bandwidth of 500 GHz per channel, and a total chirp bandwidth of 1 THz. We used an optomechanical switch to select the particular VCSEL channel, which limited the minimum scan time to about 20 ms. The last MS-FMCW iteration took advantage of the starting frequency control of the optoelectronic SFL to essentially perform real-time stitching in hardware. We used four VCSEL channels, and turned them on one at a time. Each VCSEL chirped 500 GHz in 100 μs, with a total chirp bandwidth of 2 THz and a scan time of 500 μs.

These results demonstrate the possibility of high-resolution depth imaging, e.g., optical coherence tomography, in a SCL-based platform with no moving parts.

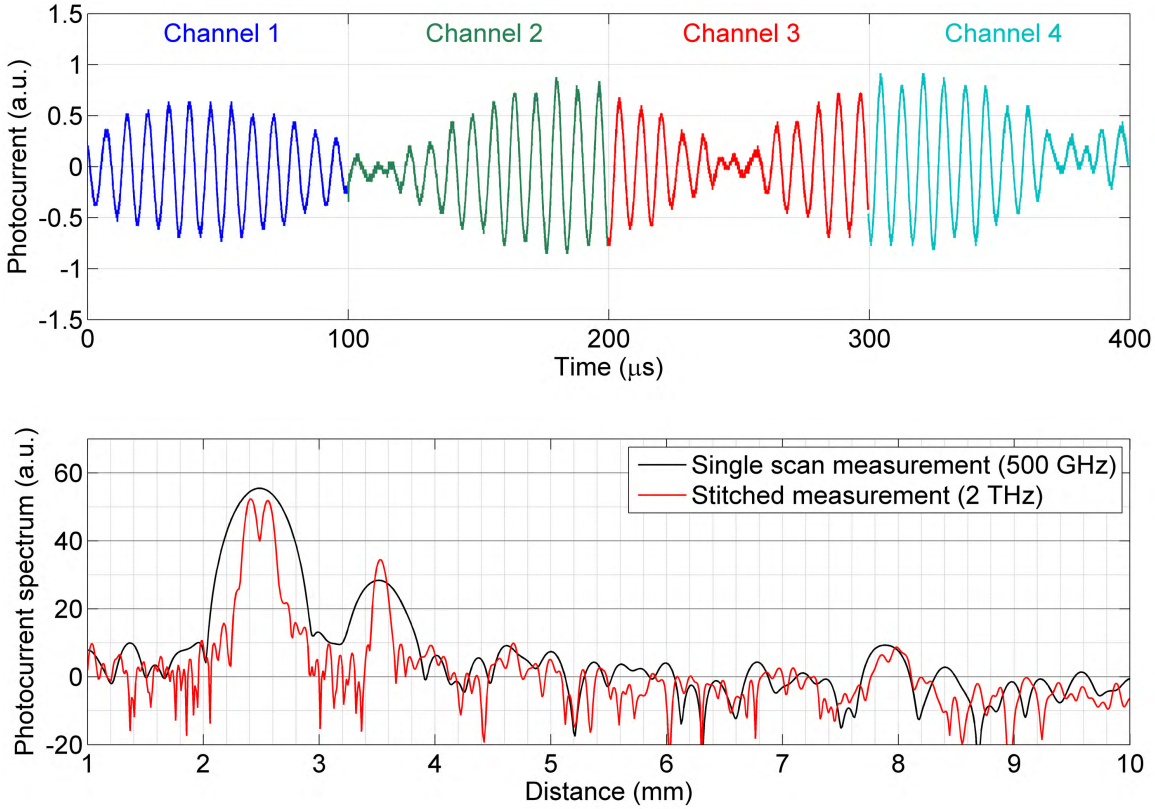

Figure 4.20: Top panel: time-domain stitched photocurrent in the hardware stitching experiment. Bottom panel: Single-sweep (black) and stitched four-sweep (red) photocurrent spectra of a 150 μm glass microscope coverslip suspended above a metal surface. The spectra are apodized with a Hamming window. The total chirp bandwidth is 2 THz.

Chapter 5

The Tomographic Imaging Camera

5.1 Introduction

So far in our discussion of 3-D imaging we have focused on the retrieval of depth information from a single location in the transverse plane. One way to acquire a full 3-D data set is through mechanical raster-scanning of the laser beam across the object space. The acquisition time in such systems is ultimately limited by the scan speed, and for very high resolution datasets (> 1 transverse mega pixel) is prohibitively slow.

Rapid 3-D imaging is of crucial importance in *in vivo* biomedical diagnostics [21, 26] because it reduces artifacts introduced by patient motion. In addition, a high-throughput, non-destructive 3-D imaging technology is necessary to meet the requirements of several new industrial developments. The emerging fields of 3-D printing and manufacturing [27] will require high-precision and cost-effective 3-D imaging capabilities. Advances in 3-D tissue engineering, such as synthetic blood vessels [28], synthetic tendons [29], and synthetic bone tissue [30], require high-resolution 3-D imaging for tissue monitoring and quality control. To ensure higher physiological relevance of drug tests, the pharmaceutical industry is moving from two-dimensional (2-D) to 3-D cell cultures and tissue models, and high-throughput 3-D imaging will be used as a basic tool in the drug development process [31]. To date, no imaging technology exists that meets these industrial demands.

In this chapter we describe our development of a conceptually new, 3-D tomographic imaging camera (TomICam) that is capable of robust, large field of view,

and rapid 3-D imaging. We develop the TomICam theory and demonstrate its basic principle in a proof-of-concept experiment. We also discuss the application of compressive sensing (CS) to the TomICam platform. CS is an acquisition methodology that takes advantage of signal structure to compress and sample the information in a single step. It is of particular interest in applications involving large data sets, such as 3-D imaging, because compression reduces the volume of information that is recorded by the sensor, effectively speeding up the measurement. We use a series of numerical simulations to demonstrate a reduction in the number of measurements necessary to acquire sparse scatterer information with CS TomICam.

5.1.1 Current Approaches to 3-D Imaging and Their Limitations

A generic FMCW 3-D imaging system has two important components: an SFL for ranging and a technique to translate the one-pixel measurement laterally in two dimensions to capture the full 3-D scene. The basic principle of FMCW ranging is illustrated in figure 5.1. The optical frequency of a single-mode laser is varied linearly with time, with a slope ξ. The output of the laser is incident on a target sample and the reflected signal is mixed with a part of the laser output in a photodetector (PD). If the relative delay between the two light paths is τ, the PD output is a sinusoidal current with frequency $\xi\tau$. The distance to the sample is determined by taking a Fourier transform of the detected photocurrent. Reflections from multiple scatterers at different depths result in separate frequencies in the photocurrent.

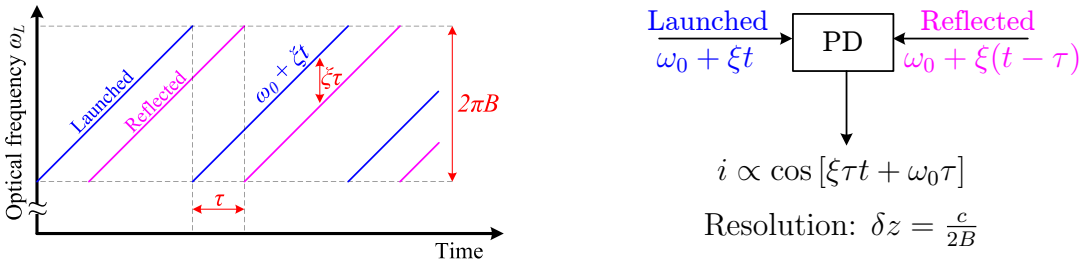

Figure 5.1: Principle of FMCW imaging with a single reflector

The important metrics of an SFL are first, the sweep linearity—a highly linear source reduces the data-processing overhead—and, second, the total frequency excursion, B, which determines the axial (z) resolution (see figure 5.1 and equation (5.3)). State-of-the-art SFL sources for biomedical and other imaging applications are typically mechanically-tuned external-cavity lasers where a rotating grating tunes the lasing frequency [26, 48, 63]. Excursions in excess of 10 THz, corresponding to axial resolutions of about 10 μm [26, 48] have been demonstrated for biomedical imaging applications. Fourier-domain mode locking (FDML) [64] and quasi-phase continuous tuning [65] have been developed to further improve the tuning speed and lasing properties of these sources. However, all these approaches suffer from complex mechanical embodiments that lead to a high system cost and limit the speed, linearity, coherence, size, reliability, and ease of use of the SFL.

Detectors for 3-D imaging typically rely on mechanical scanning of a single-pixel measurement across the scene [66], as shown schematically in figure 5.2a. The combination of high lateral resolution (< 10 μm) and large field of view (> 1 cm), requires scanning over millions of pixels, resulting in slow acquisition. The mechanical nature of the beam scanning is unattractive for high-throughput, industrial applications, due to a limited speed and reliability. It is therefore desirable to eliminate the requirement for beam scanning, and obtain the information from the entire field of view in one shot. This is possible using a 2-D array of photodetectors and floodlight illumination. However, in a high-axial-resolution system, each detector in the array measures a beat signal $\xi\tau$ in the MHz regime. A large array of high speed detectors therefore needs to operate at impractical data rates ($\sim$THz) and is prohibitively expensive. For this reason, full-field FMCW imaging systems have been limited to demonstrations with extremely slow scanning rates [25, 66] or expensive small arrays [67].

A further limitation of FMCW imaging is the need to process the photodetector information. This processing typically consists of taking a Fourier transform of the photocurrent at each lateral (x, y) position. In applications requiring real-time imaging, e.g., autonomous navigation [68], it is desirable to minimize the amount of processing overhead.

An ideal FMCW 3-D imaging system will therefore consist of a rapidly tuned SFL with a large frequency sweep and a detection technique that is capable of measuring the lateral extent of the object in one shot. The system will be inexpensive, robust, and contain no moving parts. The TomICam platform achieves these goals through its use of low-cost low-speed detector arrays. It takes advantage of the linearity and starting frequency stability of the optoelectronic SFL (see chapter 3), as well as our development of SFLs at wavelengths compatible with off-the-shelf silicon cameras (1060 nm and 850 nm). Moreover, TomICam is inherently compatible with novel compressive acquisition schemes [69], which leads to further increases in the acquisition speed.

Various other approaches to 3-D imaging have been described in literature, and recent work is summarized in table 5.1. Broadly speaking, the depth information is obtained using time-of-flight (TOF) or FMCW techniques. Transverse imaging is obtained either by mechanical scanning or using a full-field detector array. In some embodiments, compressive sensing ideas are used to reduce the number of measurements necessary to obtain the full 3-D image. TOF ranging systems illuminate the sample with a pulsed light source, and measure the arrival time of the reflected pulse(s) to obtain depth information. As a result, the axial resolution of TOF systems is limited by the pulse-width of the optical source, as well as the bandwidth of the detector. Ongoing TOF experiments rely on expensive femto/pico-second mode-locked lasers and/or acquisition systems with large bandwidths ($\simeq$ 10s of GHz), in order to achieve sub-cm axial resolution [17]. Transverse imaging is typically achieved using mechanically scanned optics [16]. Full-field imaging systems using specially designed demodulating pixels have also been demonstrated; however, these systems have significantly lower axial resolution ($\simeq$ 10s of cm) and a limited unambiguous depth of range [70].

FMCW ranging has many advantages over the TOF approach, since it eliminates the need for narrow optical pulses or accurate high-speed optical detectors and electronics (see chapter 2). Very high resolution systems (< 10 μm) have been demonstrated, and have found many applications, e.g., swept-source optical coherence

	Technology	Axial resolution	Transverse imaging	Hardware requirement	Limitations	Compressive sensing
TOF	TOF-LIDAR [16]	$\simeq$ 2 cm	Mechanical scanning	Mode-locked laser, fast electronics	Slow scanning, moving parts, expensive components, limited resolution	Not used in cited work
	Single-pixel TOF-LIDAR [17]	$\simeq$ 1 cm	Spatial light modulator, single pixel detector	Mode-locked laser, fast electronics, SLM	Expensive components, limited resolution	Used to convert the single-pixel data into a 3D model
	Lock-in TOF [70]	10s of cm	Lock-in pixel CCD	Specially engineered lock-in pixel CCD	Poor resolution, limited lock-in CCD size	Not used
FMCW	SS-OCT/CS-OCT [71]	1–10 μm	Mechanical scanning	External cavity chirped laser with moving parts, slow detector	Slow scanning, moving parts, bulky and fragile	Used to reduce scan time
	TomICam	10–100 μm	CCD/CMOS array	Optoelectronic SFL (no moving parts), standard CCD/CMOS sensor	Floodlight illumination (higher power)	Reduced acquisition time and power

Table 5.1: Recent 3-D camera embodiments

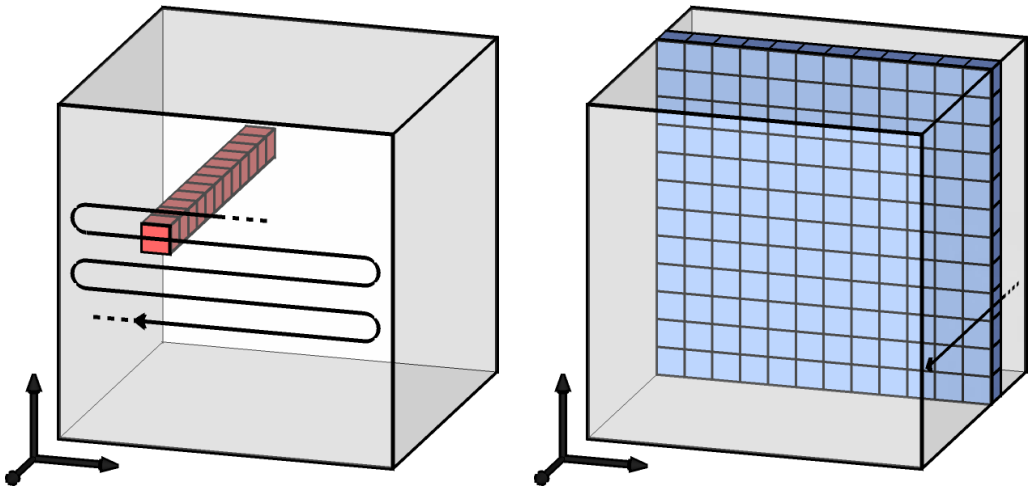

(a) (b)

Figure 5.2: (a) Volume acquisition by a raster scan of a single-pixel FMCW measurement across the object space. (b) Volume acquisition in a TomICam system. 3-D information is recorded one transverse slice at a time. The measurement depth is chosen electronically by setting the frequency of the modulation waveform.

tomography [71].

The TomICam approach is unique, in that it combines the high resolution of FMCW ranging, along with full-field imaging using a detector array, thereby eliminating any mechanical beam scanning optics. Moreover, it does not require specially engineered detectors pixels, unlike the lock-in TOF lidar [70], making it more versatile and scalable. Specifically, state-of-the art lock-in CCDs are limited to tens of thousands of pixels, while standard low-speed CMOS/CCD sensors with tens of mega pixels are commercially available. The TomICam technique therefore has significant advantages over other state-of-the-art high-resolution 3-D imaging modalities.

5.1.2 Tomographic Imaging Camera

In its basic implementation, the TomICam acquires an entire 2-D (x, y) tomographic slice at a fixed depth z, as shown in figure 5.2b. A full 3-D image is obtained by a set of measurements where the axial (z) location of the 2-D slice is tuned electronically.

An intuitive description of the TomICam principle is shown in figure 5.3. The conventional FMCW measurement in figure 5.3a produces peaks in the photocurrent

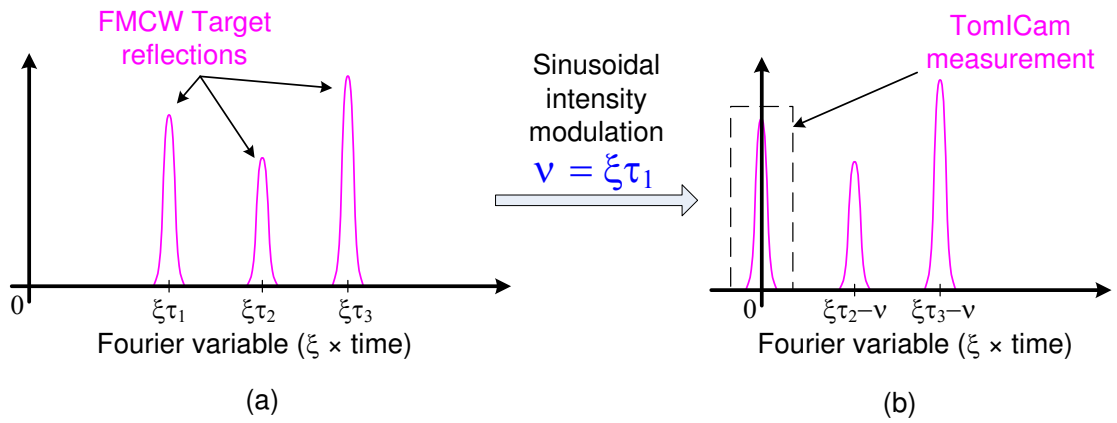

Figure 5.3: (a)Spectrum of the FMCW photocurrent. The peaks at frequencies $\xi\tau_1$, $\xi\tau_2$, and $\xi\tau_3$, where ξ is the chirp rate, correspond to scatterers at τ_1, τ_2, and τ_3. (b) The beam intensity is modulated with a frequency $\xi\tau_1$, shifting the signal spectrum, such that the peak due to a reflector at τ_1 is now at DC. This DC component is measured by a slow integrating detector.

spectrum, each peak corresponding to a scatterer at a particular depth (z) within the sample. If a sinusoidal modulation is imposed on the optical intensity, and hence on the photocurrent, the spectrum is shifted towards DC. In figure 5.3b, the DC component of the shifted spectrum is measured by a slow detector (e.g., a pixel in a CCD or CMOS array). The entire spectrum is recovered by changing the modulation frequency over several scans. This scheme supplants the need for computing the Fourier transform and thus effects a reduction in system complexity. Inherent compatibility with compressive sensing further reduces the number of measurements necessary to reconstruct the full 3-D scene.

In the following sections we develop the formalism necessary to describe the TomICam principle and its extension with compressive sensing.

5.1.2.1 Summary of FMCW Reflectometry

A detailed description of the FMCW ranging system is presented in chapter 2. Here, we briefly summarize the FMCW analysis to set the scene for TomICam. Consider the FMCW experiment shown in figure 5.4a. We analyze the response of this system under excitation by an SFL with a linear frequency sweep, $\omega(t) = \omega_0 + \xi t$. We assume that the sample comprises a set of scatterers with reflectivities R_n and round-

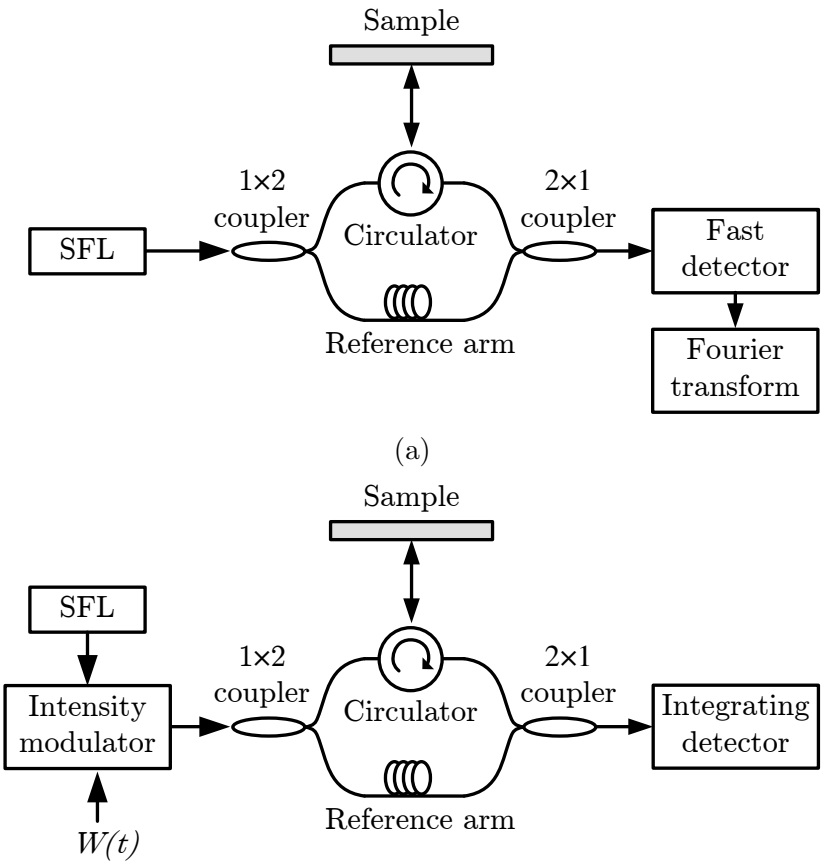

Figure 5.4: (a) Single-pixel FMCW system. The interferometric signal is recorded using a fast photodetector, and reflector information is recovered at all depths at once. (b) Single-pixel TomICam. The beam intensity is modulated with a sinusoid, and the interferometric signal is integrated using a slow detector. This gives one number per scan, which is used to calculate the reflector information at a particular depth, determined by the modulation frequency.

trip delays τ_n; and that these delays are smaller than the laser coherence time, so that any phase noise contribution can be neglected. The normalized photocurrent is equal to the time-averaged intensity of the incident beam (see chapter 2),

$$\begin{aligned} i_{\mathrm{FMCW}}(t) &= \left\langle \left| e(t) + \sum_n \sqrt{R_n}\, e(t-\tau_n) \right|^2 \right\rangle \\ &= \mathrm{rect}\left(\frac{t - T/2}{T}\right) \sum_n \sqrt{R_n} \cos\left[(\xi\tau_n)t + \omega_0\tau_n - \frac{\xi {\tau_n}^2}{2}\right], \end{aligned} \tag{5.1}$$

where T is the scan duration, ξ is the slope of the optical chirp, ϕ_0 and ω_0 are the initial phase and frequency, respectively, and only the cross terms were retained for simplicity. The total frequency excursion of the source (in Hz) is therefore given by $B = \xi T/2\pi$. A Fourier transform of this photocurrent results in a map of scatterers along the direction of beam propagation (e.g., figure 5.3a). The strength of a scatterer at some delay τ is given by the intensity of the Fourier transform of equation (5.1), evaluated at a frequency $\nu = \xi\tau$:

$$\left|Y\left(\nu = \xi\tau\right)\right|^2 = \left| \int_0^T \exp\left[j(\xi\tau)t\right] i_{\mathrm{FMCW}}(t) dt \right|^2. \tag{5.2}$$

By the Fourier uncertainty relation, the resolution of this measurement is inversely proportional to the integration time T. The spatial resolution is, therefore, given by

$$\Delta z = \frac{c}{2}\frac{2\pi}{\xi}\frac{1}{T} = \frac{c}{2B}, \tag{5.3}$$

where c is the speed of light.[1]

5.1.2.2 TomICam Principle

The key idea behind TomICam is that the Fourier transform required for FMCW data processing may be performed in hardware using an integrating photodetector, e.g. a pixel in a CCD or CMOS imaging array. To this end, we modify the basic FMCW experiment to include an intensity modulator, as shown in figure 5.4b. The

[1] The scatterer range is given by $z = c\tau/2$.

integrating detector is reset at the beginning of every sweep, and sampled at the end. For a given modulation signal $W(t)$, the beat signal at the detector is given by

$$y_W(t) \propto W(t)\ i_{\mathrm{FMCW}}(t). \tag{5.4}$$

The value sampled at the output of the integrating detector is therefore given by

$$Y_W = \int_0^T W(t)\ i_{\mathrm{FMCW}}(t)dt, \tag{5.5}$$

where Y_W is the TomICam measurement corresponding to an intensity modulation waveform $W(t)$, and we assumed an overall system gain of 1 for simplicity. The TomICam measurement therefore amounts to projecting the FMCW photocurrent of equation (5.1) onto a basis function described by the modulation $W(t)$.

We consider two modulations: $W_C = \cos[(\xi\tau)t]$, and $W_S = \sin[(\xi\tau)t]$, which correspond to the cosine and sine transforms.

$$Y_{W_C}(\tau) = \int_0^T \cos[(\xi\tau)t]\ \ i_{\mathrm{FMCW}}(t)dt \tag{5.6}$$

$$Y_{W_S}(\tau) = \int_0^T \sin[(\xi\tau)t]\ \ i_{\mathrm{FMCW}}(t)dt \tag{5.7}$$

Equation (5.2) may therefore be written as:

$$|Y(\nu = \xi\tau)|^2 = |Y_{W_C}(\tau) + j * Y_{W_S}(\tau)|^2 = |Y_{W_C}(\tau)|^2 + |Y_{W_S}(\tau)|^2. \tag{5.8}$$

The scatterer strength at a delay τ is calculated using two consecutive scans. The strength of the TomICam platform lies in its ability to generate depth scans using low-bandwidth integrating detectors, making possible the use of a detector array, such as a CMOS or CCD camera. A possible extension to a 2-D integrating detector array is shown in figure 5.5. Each element in the array performs a TomICam measurement at a particular lateral (x, y) location, as described above. The TomICam platform

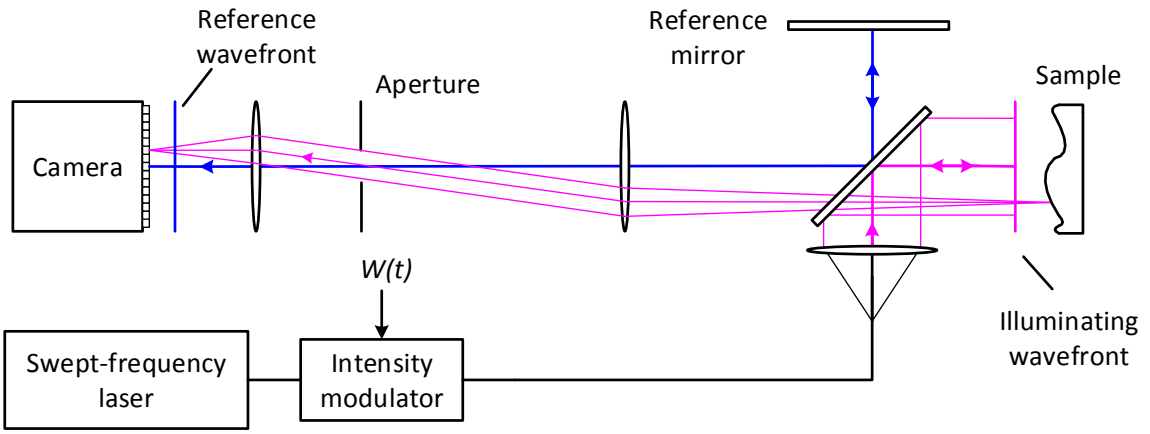

Figure 5.5: A possible TomICam configuration utilizing a CCD or CMOS pixel array in a Michelson interferometer. Each transverse point (x, y) at a fixed depth (z) in the object space is mapped to a pixel on the camera. The depth (z) is tuned electronically by adjusting the frequency of the modulation waveform $W(t)$.

therefore has the following important features:

- A full tomographic slice is obtained in a time that is only limited by the chirp duration. This is orders of magnitude faster than a raster-scanning solution, and enables real-time imaging of moving targets.
- The depth of the tomographic slice is controlled by the electronic waveform $W(t)$, so that the entire 3-D sample space can be captured without moving parts.
- It leverages the integrating characteristic of widely available inexpensive CCD and CMOS imaging arrays to substantially reduce signal processing overhead.
- It is scalable to a large number of transverse pixels with no increase in acquisition or processing time.
- The TomICam platform is not limited to sinusoidal modulations $W(t)$, making it inherently suitable for compressive sensing, as described in section 5.2.

5.1.2.3 TomICam Proof-of-Principle Experiment

In order to verify the equivalence of FMCW and TomICam measurements, we have performed a proof-of-principle experiment, shown schematically in figure 5.6. We

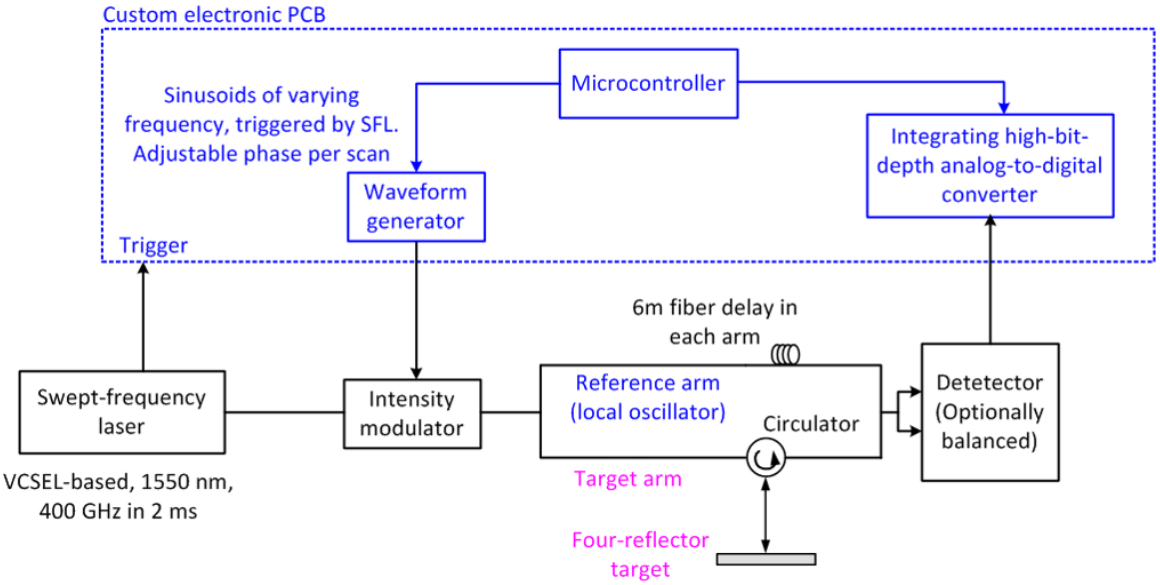

Figure 5.6: Schematic diagram of the TomICam proof-of-principle experiment. A slow detector was modeled by a fast detector followed by an integrating analog-to-digital converter. The detector signal was sampled in parallel by a fast oscilloscope, to provide a baseline FMCW depth measurement.

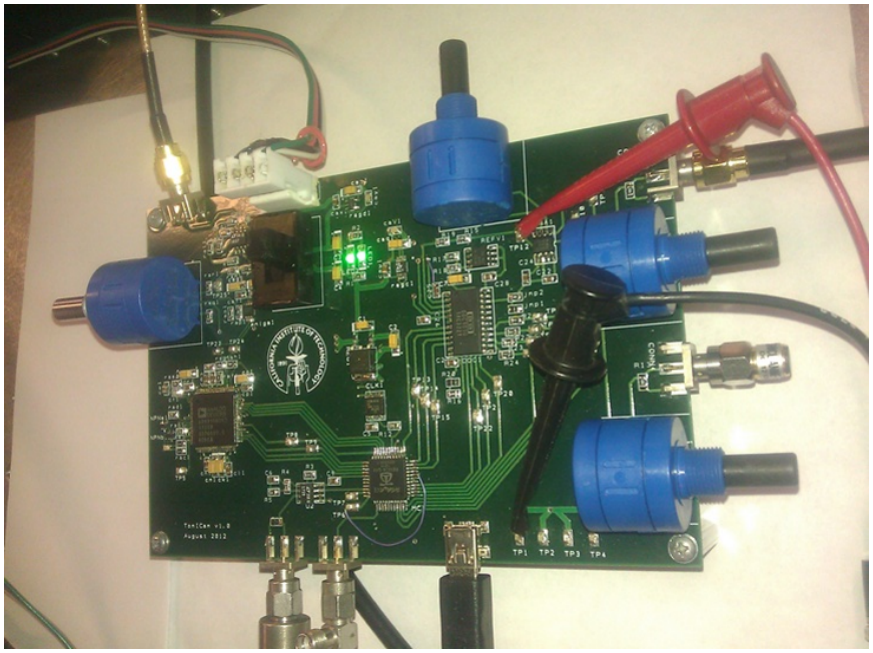

Figure 5.7: The custom PCB used in the TomICam experiment. Implemented functionality includes triggered arbitrary waveform generation and high-bit-depth acquisition of an analog signal.

used the 1550 nm VCSEL-based optoelectronic SFL, described in section 3.4.1, which produced a precisely linear chirp with a swept optical bandwidth of 400 GHz, and a scan time of 2 ms. The beam was modulated using a commercially available lithium niobate intensity modulator.

The necessary electronic functionality, including an arbitrary waveform generator, an integrating high-bit-depth analog-to-digital converter, and a microcontroller, was implemented on a PCB, shown in figure 5.7. The waveform generator was used to provide sine and cosine waveforms of different frequencies to the intensity modulator. The amplitude of these waveforms was apodized by a Hamming window, which suppressed the sinc sidebands associated with a rectangular apodization. The integrating analog-to-digital converter recorded a single number per scan. The microcontroller was used to coordinate the waveform generation and signal acquisition. The photodetector output was also sampled on a high-speed oscilloscope in order to provide a baseline FMCW measurement.

We used a sample comprising two acrylic slabs. Reflections from the air-acrylic and acrylic-air interfaces were recorded and the results are shown in figure 5.8. The red curve is the intensity of the Fourier transform of the FMCW photocurrent. The blue curve is constructed by varying the frequencies of the modulation waveforms $W_C(t)$ and $W_S(t)$, and applying equation (5.8). As expected, the two curves are practically identical.

We note that a copy of the signal, scaled in frequency by a factor of $\frac{1}{3}$, shows up in the TomICam spectrum in figure 5.8. This ghost replica is due to a third-order nonlinearity exhibited by our intensity modulator, and can be resolved through the use of a linear intensity modulator. An example of such a modulator is the amplitude controller based on an semiconductor optical amplifier in a feedback loop, described in section 3.3.2.

We characterize the dynamic range of our system by performing FMCW and TomICam measurements on a fiber Mach-Zehnder interferometer (MZI). We introduce optical attenuation in one of the MZI arms, and measure the signal SNR. The results for unbalanced and balanced acquisition in FMCW and TomICam configura-

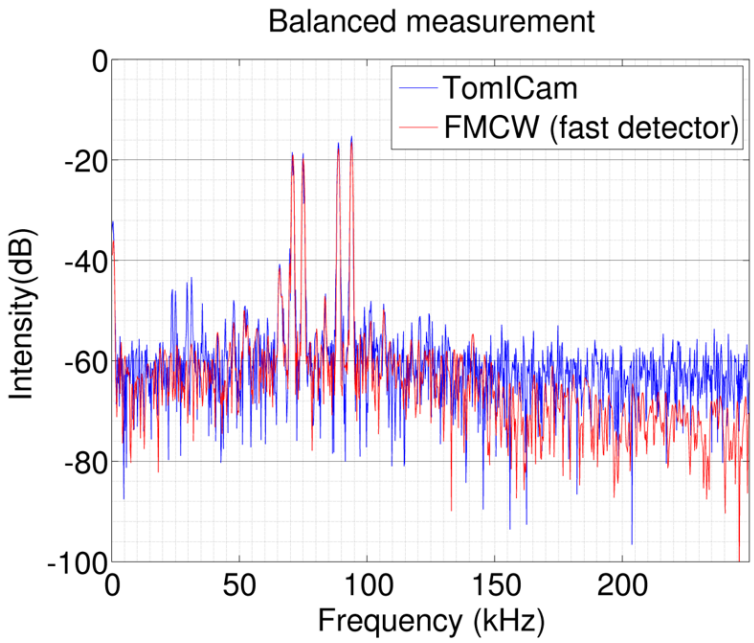

Figure 5.8: Comparison between FMCW (red) and TomICam (blue) depth measurements. The two are essentially identical except for a set of ghost targets at $\frac{1}{3}$ of the frequency present in the TomICam spectrum. These ghosts are due to the third-order nonlinearity of the intensity modulator used in this experiment.

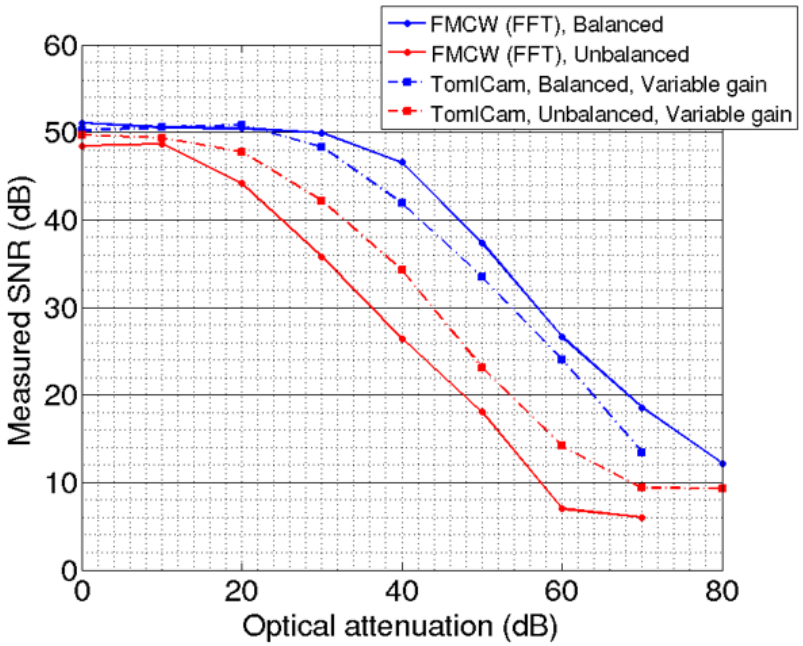

Figure 5.9: Characterization of the FMCW and TomICam dynamic range. The signal-to-noise ratio was recorded as a function of attenuation in one of the interferometer arms. At low attenuations, the SNR saturates due to SFL phase noise and residual nonlinearity.

tions are shown in figure 5.9. The dynamic range of our system, defined as the ratio of the strongest to weakest measurable target reflectivity, is about ~ 80 dB. For low attenuation, i.e., large reflectivities, the SNR is limited by the laser coherence and residual chirp nonlinearity, saturating at a (path-length mismatch dependent) value of ~ 50 dB. The fiber mismatch used in this experiment was about 40 mm.

5.2 Compressive Sensing

The total number of tomographic slices, N, used in a 3-D image reconstruction is given by the axial extent, L_z, of the target divided by the axial resolution, Δz. We note that most real life targets are sparse in the sense that they have a limited number of scatterers, k, in the axial direction. The acquisition of $N \gg k$ slices to form the 3-D image is therefore inefficient. In this section, we investigate the use of compressive sensing (CS) in conjunction with the TomICam platform in order to obtain the 3-D image with many fewer than N measurements. This has the potential to reduce the image acquisition time and the optical energy requirement of the TomICam by orders of magnitude.

5.2.1 Compressive Sensing Background

We briefly state the salient features of CS [69]. Consider a linear measurement system of the form:

$$\mathbf{y} = \mathbf{A}\mathbf{x} \qquad \mathbf{A} \in \mathbb{C}^{m \times N}, \mathbf{x} \in \mathbb{C}^{N}, \mathbf{y} \in \mathbb{C}^{m}, \tag{5.9}$$

where the vector $\mathbf{x}$ is the signal of interest, and the vector $\mathbf{y}$ represents the collected measurements. The two are related by the measurement matrix $\mathbf{A}$. The case of interest is the highly under-determined case, $m \ll N$. The system therefore possesses infinitely many solutions. Nevertheless, CS provides a framework to uniquely recover $\mathbf{x}$, given that $\mathbf{x}$ is sufficiently sparse, and the measurement matrix $\mathbf{A}$ satisfies certain properties such as restricted isometry and incoherence [69]. The intuition behind CS

is to perform the measurements in a carefully chosen basis where the representation of the signal $\mathbf{x}$ is not sparse. The signal is then recovered by finding the sparsest $\mathbf{x}$ that is consistent with the measurement in equation (5.9). Specifically, the recovery is accomplished by solving a convex minimization problem:

$$\begin{aligned} &\text{minimize} && \|\mathbf{x}\|_1 \\ &\text{subject to} && \mathbf{A}\mathbf{x} = \mathbf{y}, \end{aligned} \tag{5.10}$$

where $\|\mathbf{x}\|_1$ denotes the l_1 norm of $\mathbf{x}$. The use of the l_1 norm promotes sparse solutions, while maintaining convexity of the minimization problem, resulting in a tractable computation time. Success of recovery depends on the number of measurements m, the sparsity level of $\mathbf{x}$, and the properties of the measurement matrix $\mathbf{A}$. This approach is of particular interest due to continuous advances in computational algorithms that improve the reconstruction speed [72].

5.2.2 TomICam Posed as a CS Problem

Fundamentally, the FMCW imaging technique converts the reflection from a given depth in the z direction to a sinusoidal variation of the detected photocurrent at a frequency that is proportional to the depth. Scatterers from different depths thus result in a photocurrent with multiple frequency components. In its basic implementation (section 5.1.2.2), the TomICam uses a single-frequency modulation of the beam intensity to determine one of these possible frequency components. Full image acquisition requires N measurements ($N = L_z/\Delta z$), determined by the axial resolution of the swept-frequency source. When the number of axial scatterers—and hence the number of frequency components in the photocurrent—is sparse, the CS framework enables image acquisition with a smaller number of measurements.

We first show that the TomICam is inherently suited to compressive imaging and that different types of measurements may be easily performed with almost no modification to the system. We recast equation (5.5) in a form more suitable for the discussion of CS. We assume that there are N possible target locations with

corresponding delays $\tau_n,\ n = 0, 1, \ldots, (N-1)$ and target reflectivities R_n. These target locations are separated by the axial resolution: $\tau_n = n/B$. We assume that the target is k-sparse so that only k of the N possible reflectivities are nonzero. The time axis is discretized to N points given by $t_h = \frac{hT}{N}, h = 0, 1, \ldots (N-1)$. Equation (5.5) can now be written as

$$y = \sum_{h=0}^{N-1} \sum_{n=0}^{N-1} W(t_h) \frac{\sqrt{R_n}}{N} \cos\left(\xi \tau_n t_h + \omega_0 \tau_n\right). \tag{5.11}$$

Each TomICam measurement therefore yields a single value y for a particular $W(t_h)$ (per pixel in the lateral plane), as given by equation (5.11). Note that a sinusoidal variation of $W(t_h)$ yields the reflectivity at a particular axial depth, and a tomographic slice is obtained using a detector array, as described in section 5.1.2.2.

In this section, we will explore other intensity modulation waveforms $W(t_h)$ that are compatible with the CS framework to reduce the number of scans in the axial dimension. We extend the discussion to include m measurements indexed by s, i.e., we will use m different intensity modulation waveforms $W_s(t_h)$ to obtain m distinct measurements y_s. Equation (5.11) can be simplified to give

$$\begin{aligned} y_s &= \sum_{h=0}^{N-1} \sum_{n=0}^{N-1} W_s\left(\frac{hT}{N}\right) \cdot \frac{1}{\sqrt{N}} \exp\left(-j\frac{2\pi hn}{N}\right) \cdot \sqrt{\frac{R_n}{N}} \exp\left(-j\frac{\omega_0}{B} n\right) \\ &= \sum_{h=0}^{N-1} \sum_{n=0}^{N-1} W_{sh} \cdot F_{hn} \cdot x_n, \end{aligned} \tag{5.12}$$

where $W_{sh} \equiv W_s\left(\frac{hT}{N}\right),\ F_{hn} \equiv \frac{1}{\sqrt{N}} \exp\left(-j\frac{2\pi hn}{N}\right),\ x_n \equiv \sqrt{\frac{R_n}{N}} \exp\left(-j\frac{\omega_0}{B} n\right)$, and it is understood that the measurements correspond to the real part of the right hand side. Rewriting equation (5.12) in matrix notation, we obtain:

$$\mathbf{y} = \mathbf{WFx}, \tag{5.13}$$

where $\mathbf{x}$ is the k-sparse target vector of length N, $\mathbf{y}$ is the vector containing the m TomICam measurements, $\mathbf{F}$ is the $N \times N$ unitary Fourier matrix, and $\mathbf{W}$ is the $m \times N$

matrix that comprises the m intensity modulation waveforms $W_s(t_h)$.

Since $\mathbf{W}$ is electrically controlled, a variety of measurement matrices can therefore be programmed in a straightforward manner. Each TomICam measurement y_s is obtained by multiplying the optical beat signal with a unique modulation waveform $W_s(t_h)$ and integrating over the measurement interval. If the modulation waveforms are chosen appropriately, the measurement matrix can be made to satisfy the crucial requirements for CS, i.e., the restricted isometry property and incoherence [69]. This ensures that the information about the target—which is sparse in the axial dimension—is "spread out" in the domain in which the measurement is performed, and a much smaller number of measurements is therefore sufficient to successfully recover the complete image.

5.2.3 Robust Recovery Guarantees

We now consider two possibilities for $\mathbf{W}$ that yield a measurement matrix capable of robust signal recovery. These represent straightforward implementations of CS TomICam imaging.

5.2.3.1 Random Partial Fourier Measurement Matrix

A random partial Fourier matrix of size $m \times N$ is generated by selecting m rows at random from the $N \times N$ Fourier matrix $\mathbf{F}$. This operation is accomplished by a binary matrix $\mathbf{W}$ that has a single nonzero entry in each row. The location of the nonzero entry is chosen randomly without replacement. For this class of matrices, robust signal recovery is guaranteed whenever the number of measurements satisfies [73]

$$m \geq Ck \log(N/\epsilon), \tag{5.14}$$

where k is the signal sparsity, $1-\epsilon$ is the probability of recovery, and C is a constant of order unity.

In the TomICam implementation, a random partial Fourier measurement corresponds to pulsing the intensity modulator during the linear chirp, so that only a single

optical frequency is delivered to the target per scan, leaving a lot of dead time. As a result, the optoelectronic SFL is not the most ideal laser candidate, and other sources that can provide rapid random frequency access, such as sampled grating SCLs, are more suitable [74]. In these devices, the cavity mirrors are formed using a pair of sampled gratings, each of which has multiple spectral reflection bands. Current tuning of the mirror sections is used to make these reflection bands overlap, forming a single band whose position may be varied over a broad spectral range. Further, a phase section current is applied to align a Fabry-Pérot cavity mode to the middle of the band in order to optimize lasing properties. Simultaneously tuning all three sections enables broadband frequency access, approaching 5 THz at 1550 nm [75].

5.2.3.2 Gaussian or Sub-Gaussian Random Measurement Matrix

This class of matrix has the property that any entry A_{ij} in the matrix $\mathbf{A}$ is randomly chosen from independent and identical Gaussian or sub-Gaussian distributions. In this case, robust signal recovery is guaranteed for

$$m \geq Ck \log (N/k), \tag{5.15}$$

where k is the signal sparsity, and C is a constant of order unity. Moreover, the same result also applies to a measurement matrix that is a product of a Gaussian or sub-Gaussian random matrix and a unitary matrix. Since $\mathbf{F}$ is unitary, a Gaussian random matrix $\mathbf{W}$ results in robust signal recovery when equation (5.15) is satisfied [76]. The measurements obtained using a Gaussian matrix $\mathbf{W}$ may be interpreted as a collection of conventional TomICam measurements where each measurement queries all possible depths with different weights.

We want the failure rate ϵ to be much less than unity, while the sparsity level k is at least unity. Therefore, the Gaussian random matrix requires fewer measurements than the random partial Fourier matrix for correct recovery.

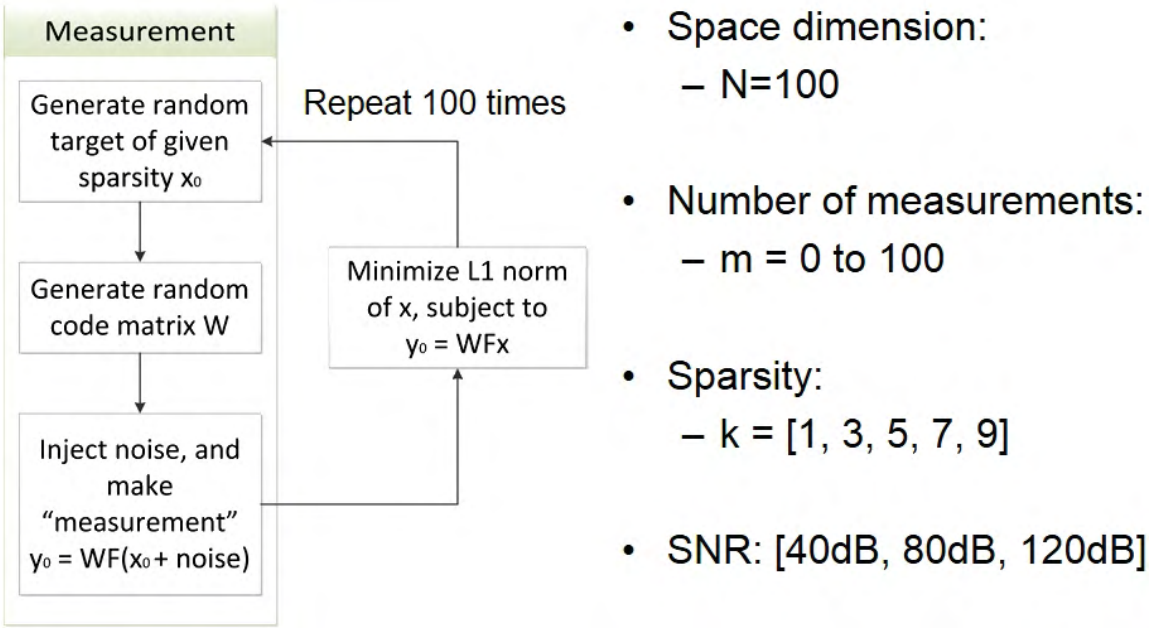

Figure 5.10: Flow diagram and parameters of the CS TomICam simulation

5.2.4 Numerical CS TomICam Investigation

Because the partial Fourier matrix is not well-suited for the TomICam platform, we continue our investigation with the Gaussian random matrix in mind. We evaluate the performance of a compressively-sampled TomICam through a series of numerical simulations. The simulation steps and parameters are summarized in figure 5.10.

We consider a signal space with dimension $N = 100$, and generate a random target signal $\mathbf{x_0}$ of a given sparsity. We generate a Gaussian random matrix W of size $m \times N$, where m is the number of measurements. We then make a noisy measurement

$$\mathbf{y_0} = \mathbf{WF}(\mathbf{x_0} + \mathbf{x_n}), \tag{5.16}$$

where $\mathbf{x_n}$ is a randomly generated noise vector. We define the SNR as the ratio of the signal and noise energies,

$$\text{SNR} \equiv \frac{\|\mathbf{x_0}\|_2}{\|\mathbf{x_n}\|_2}. \tag{5.17}$$

We then proceed to solve the convex minimization problem in equation (5.10), which yields the recovered signal $\mathbf{x}$. We define the signal-to-error ratio (SER) as the ratio of

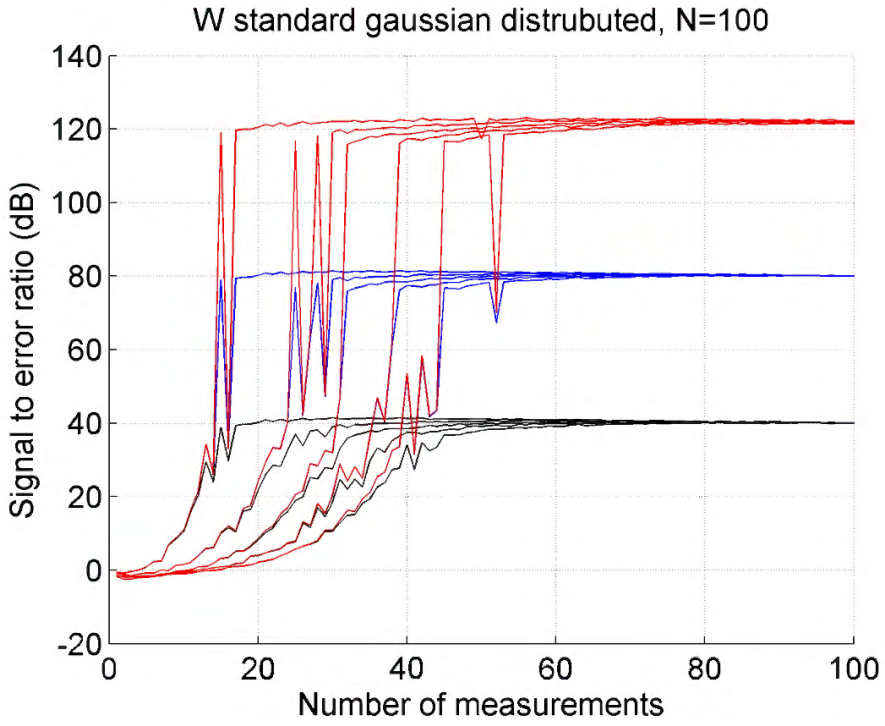

Figure 5.11: SER curves for a CS simulation with a Gaussian random matrix

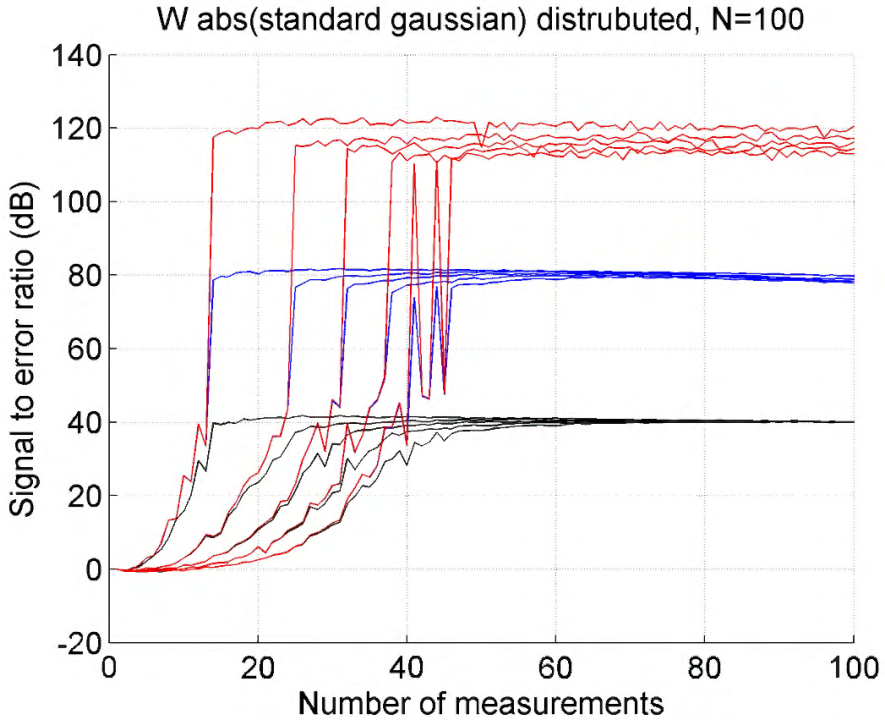

Figure 5.12: SER curves for a CS simulation with a waveform matrix given by the absolute value of a Gaussian random matrix

the energy of the recovered signal to the energy of the difference between the recovered and the original signals.

$$\text{SER} \equiv \frac{\|\mathbf{x}\|_2}{\|\mathbf{x} - \mathbf{x_0}\|_2}. \tag{5.18}$$

We repeat this procedure 100 times and record the average SER. We consider $0 < m < 100$, and simulate 100 reconstructions for each value of m, resulting in a curve of SER vs. m. We generate 15 such a curves by considering five sparsity levels $k = [1, 3, 5, 7, 9]$, and three noise levels SNR $= [40\text{dB}, 80\text{dB}, 120\text{dB}]$.

These curves are plotted in figure 5.11, with the 120 dB SNR shown in red, 80 dB in blue, and 40 dB in black. We expect that for a small number of measurements, the reconstructions will fail, yielding a zero SER. Once the number of measurements satisfies equation (5.15), the reconstruction will essentially always succeed, yielding an SER that is approximately equal to the SNR. This is the pattern that we see in figure 5.11. The curves corresponding to the different sparsity levels are in order, with the sparsest case achieving the transition in SER at the lowest number of measurements. We observe that ~ 50 measurements are necessary to recover a 9-sparse target, which corresponds to a factor of two compression, when compared to conventional sampling.

We note that a Gaussian random matrix has negative entries, and is therefore not physical (we can only modulate the beam intensity with a positive waveform). To fix this, we investigate numerically random matrices that contain only positive entries. SER curves for $\mathbf{W}$ given by the absolute value of a Gaussian random matrix are shown in figure 5.12. The qualitative behavior of the curves is unchanged from the random Gaussian case.

A passive intensity modulator can only provide a modulation between 0 and 1, and we therefore examine a waveform matrix $\mathbf{W}$ with entries that are uniformly distributed between 0 and 1. The SER curves for this case are shown in figure 5.13, and follow the trend of the previous simulations.

Realistic intensity modulators have a finite extinction ratio, meaning they cannot be used to turn the beam completely off. Moreover, it may be desirable to operate the

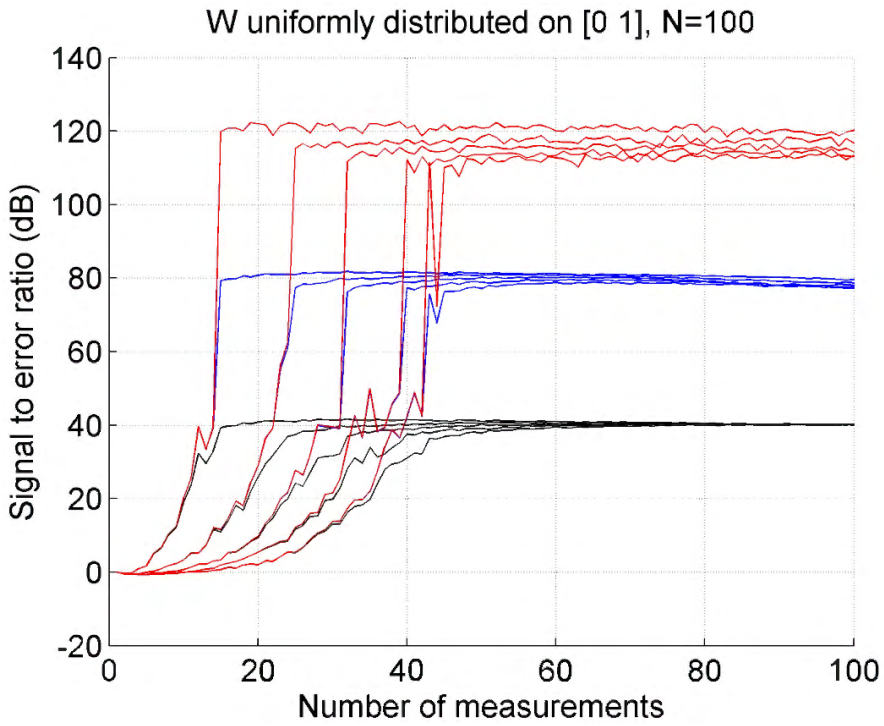

Figure 5.13: SER curves for a CS simulation with a waveform matrix whose entries are uniformly distributed between 0 and 1

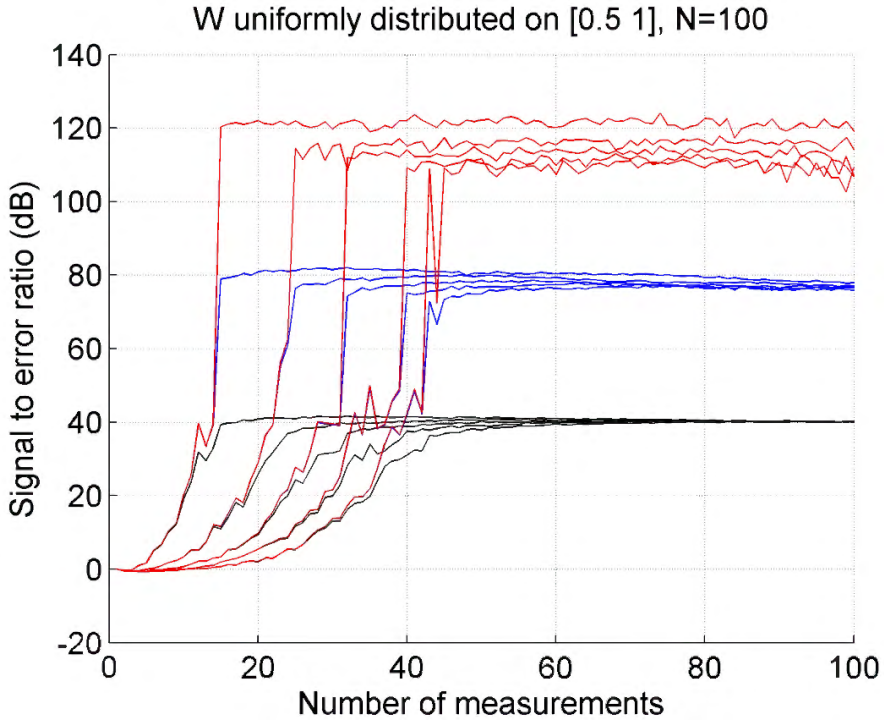

Figure 5.14: SER curves for a CS simulation with a waveform matrix whose entries are uniformly distributed between 0.5 and 1

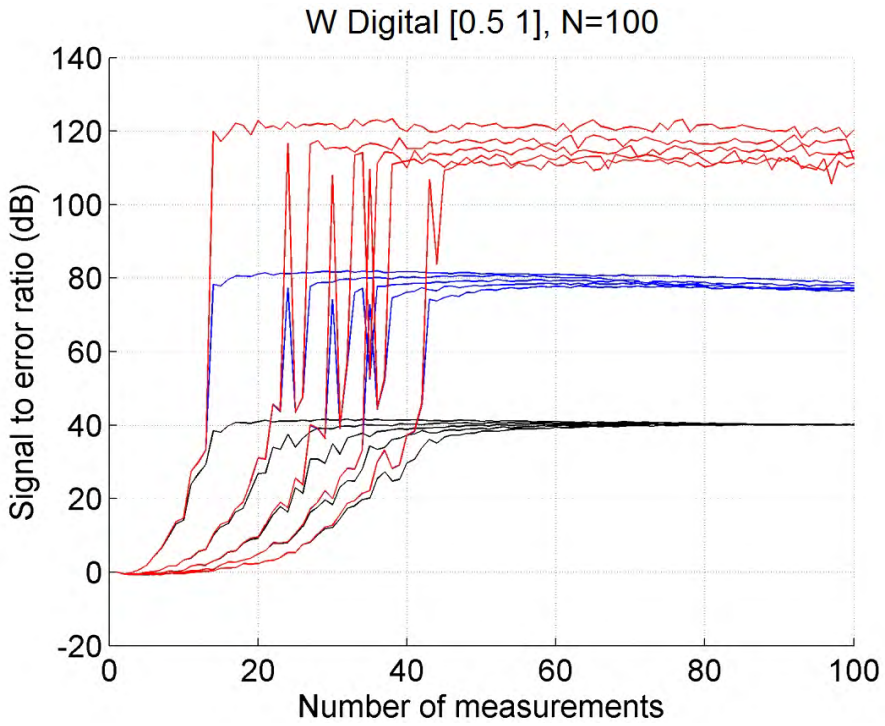

Figure 5.15: SER curves for a CS simulation with a waveform matrix whose entries take on the values of 0.5 or 1 with equal probabilities

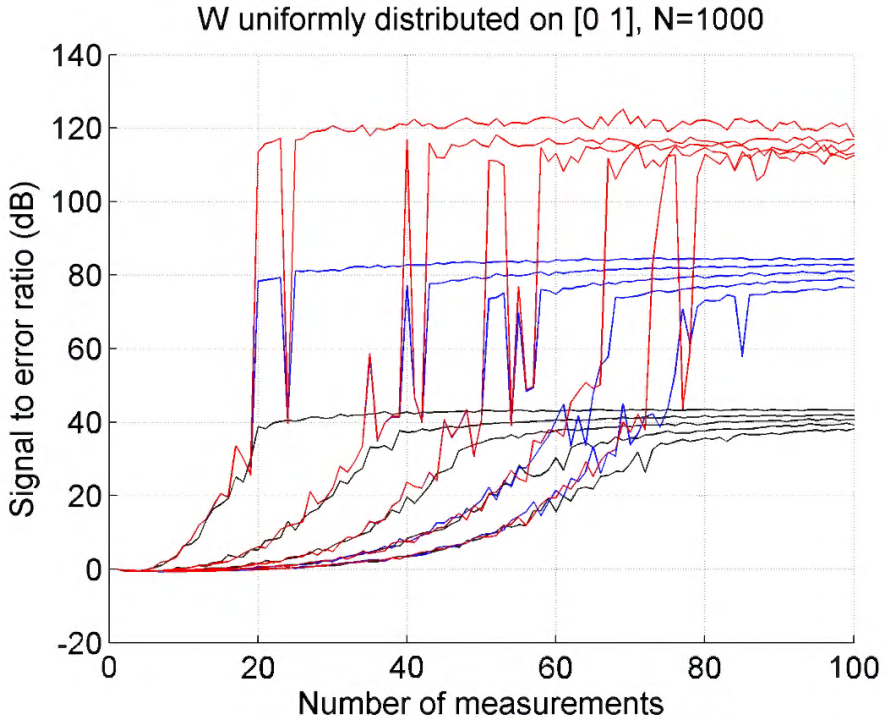

Figure 5.16: SER curves for an $N = 1000$ CS simulation with a waveform matrix whose entries are uniformly distributed between 0.5 and 1

intensity modulator away from the zero point to keep its response as linear as possible. To account for this possibility we ran the simulation using a waveform matrix $\mathbf{W}$ with entries that are uniformly distributed between 0.5 and 1. Again, the transition trends for the SER curves, shown in figure 5.14 remain essentially unchanged.

The waveform generator has a finite bit depth, and we consider, as an extreme case, only two modulation levels—0.5 and 1—which corresponds to a waveform matrix $\mathbf{W}$ whose entries can equal either of the modulation levels with equal probabilities. The SER curves for this simulation are shown in figure 5.15, and again demonstrate the same behavior.

For our final simulation we increased the dimension of the space to 1000, and used a waveform matrix $\mathbf{W}$ with entries that are uniformly distributed between 0 and 1. The SER curves for this simulation are shown in figure 5.16. We observe that ~ 80 measurements are necessary to recover a 9-sparse target, which corresponds to greater than $10\times$ compression, when compared to conventional sampling.

5.3 Summary

In this chapter we described the basic tomographic imaging camera principle, and demonstrated single-pixel TomICam ranging in a proof-of-concept experiment. The TomICam uses a combination of electronically tuned optical sources and low-cost full-field detector arrays, completely eliminating the need for moving parts traditionally employed in 3-D imaging. This new imaging modality could be useful in a variety of established and emerging disciplines, including lidar [18], profilometry [22], biometrics [25], biomedical diagnostics [21, 26], 3-D manufacturing [27], and tissue engineering [28–31].

We also discussed the application of compressive sensing to the TomICam platform, and performed a series of numerical simulations. These simulations show that a factor of 10 reduction in the number of measurements is possible with CS if the number of depth bins is about 1000. Future implementations of TomICam will benefit from the development of high frame rate, high pixel count silicon CCD and CMOS

cameras, rapidly-tunable semiconductor lasers [77], efficient compressive sensing algorithms, and continuous advances in computing performance. As a result, TomICam has the potential to push 3-D imaging functionality well beyond the state of the art.

Chapter 6

Phase-Locking and Coherent Beam Combining of Broadband Linearly Chirped Optical Waves

6.1 Introduction

Optical phase-locking has found various applications in the fields of optical communication links [52, 78–81], clock generation and transmission [82, 83], synchronization and recovery [84, 85], coherence cloning [7], coherent beam combining (CBC) and optical phased arrays [8, 86–91], and optical frequency standards [92, 93], to name a few. In these applications, electronic feedback is used to precisely synchronize the phases of two optical waves. With a few notable exceptions [34, 94], prior demonstrations of phase-locking and synchronization have been performed using nominally monochromatic optical waves. In this chapter we describe our work on the phase-locking of optical waves whose frequencies are swept rapidly with time and over large chirp extents. The phase-locking of optical waves with arbitrary frequency chirps is a difficult problem in general. However, precisely linear chirps, such as the ones generated by the optoelectronic SFL (see chapter 3) can be phase-locked with very high efficiency using a frequency shifter. The main application of this result is the simultaneous stimulated Brillouin scattering (SBS) suppression and coherent combining of high-power fiber amplifiers. Other potential applications include electronic beam steering for lidar and 3-D imaging systems.

We begin our discussion by reviewing CBC approaches to the generation of high-power continuous-wave optical beams. We proceed to describe the basic principle behind phase-locking of linearly chirped optical waves, and present theoretical analyses of chirped-wave phase-locking in homodyne and heterodyne configurations. We demonstrate heterodyne phase-locking of chirped optical waves and implement a passive-fiber CBC system [10, 11]. We conclude with a description of our recent CBC experiment with two erbium-doped fiber amplifier (EDFA) channels [12]. The work described in this chapter was performed in collaboration with Jeffrey O. White's group at the United States Army Research Laboratory.

6.2 Coherent Beam Combining

The output power of optical fiber amplifiers is usually limited by SBS. Advances in the design of the geometry and doping profiles of active fiber have enabled increases in the SBS threshold power [95–97]. Further increases in the SBS threshold of a single amplifier can be obtained by broadening the linewidth of the seed laser through phase or frequency modulation [32,33]. A separate approach to achieving high optical powers is the coherent beam combining of the outputs of multiple laser or amplifier elements [8, 86–90].

The efficiency of a CBC scheme depends on the matching of the relative amplitudes, phases, polarizations and pointing directions of the multiple emitters in the array [86, 98, 99]. Phase synchronization of the array elements is a particularly difficult challenge, which in the past has been addressed with various approaches, including evanescent wave and leaky wave coupling of emitters [100, 101], common resonator arrays [102, 103], and phase-locking through optoelectronic feedback [8, 90]. In optoelectronic feedback systems, the phase error between the combined beams is measured and fed back to a phase actuator, such as an electro-optic phase modulator [87], acousto-optic frequency shifter [90], or a fiber stretcher [34, 89].

Kilowatt-level systems have been demonstrated [33] and rely on the simultaneous suppression of SBS in high-power fiber amplifiers and the CBC of multiple amplifier

channels. The path-length mismatch between array elements in an amplifier CBC system has to be much smaller than the seed coherence length, in order to prevent de-phasing due to incoherence. The traditional approach to SBS suppression relies on a broadening of the seed linewidth, and therefore a reduction of its coherence length. As a result, SBS suppression in high-power fiber amplifier CBC systems requires precise channel path-length matching. Recently, Goodno et al. [33] have demonstrated the phase-locking of a 1.4 kW fiber amplifier. This power level was achieved by increasing the SBS threshold using a modulated seed source with a linewidth of $\sim$ 21 GHz. Efficient power combining was only possible with precise path-length matching of active fibers to sub-mm accuracy. Further increases in the power output of a single amplifier will require even broader seed linewidths, and path-length matching to within $\sim$ 10s of μm will be necessary. Weiss et al. [34] have recently demonstrated that coherent combining can still be achieved using a novel feedback loop that senses the path-length mismatch and corrects it using a fiber stretcher.

In this chapter we explore an architecture capable of SBS suppression and coherent beam combining without stringent mechanical path-length matching requirements [10–12]. Our approach is to use a rapidly chirped ($> 10^{14}$ Hz/s) swept-frequency laser (SFL) seed to reduce the effective length over which SBS occurs [35, 36]. The advantage of this approach is that path-length matching requirements are relaxed due to the long coherence length (several meters) of semiconductor laser based SFLs. In the following section we describe the basic principle of phase-locking of linearly chirped optical waves using acousto-optic frequency shifters (AOFSs) to compensate for static and dynamic optical path-length differences. We proceed with an analysis of homodyne and heterodyne optical phase-locked loop (OPLL) configurations, and present results of proof-of-concept experiments that demonstrate phase-locking, coherent combining, and electronic phase control in chirped-wave passive-fiber systems.

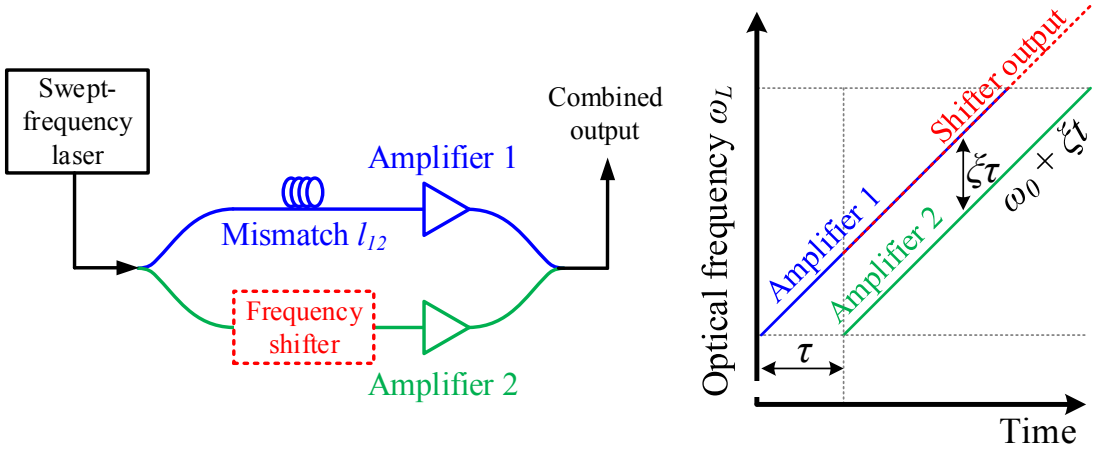

Figure 6.1: Intuitive description of chirped-seed amplifier coherent beam combining. A path-length mismatch between amplifier arms results in a frequency difference at the combining point, and can therefore be compensated using a frequency shifter placed before amplifier 2.

6.3 Phase-Locking of Chirped Optical Waves

The basic concept of phase-locking multiple chirped-seed amplifiers (CSAs) in a master oscillator power amplifier (MOPA) configuration is depicted in figure 6.1 [10, 11]. A SFL is used to generate a linear chirp, with an instantaneous optical frequency given by

$$\omega_L(t) = \omega_{L,0} + \xi t, \;\; 0 \leq t \leq T, \tag{6.1}$$

where $\omega_{L,0}$ is the initial optical frequency, ξ is the sweep rate, and T is the sweep time. The SFL is split into multiple amplifier seeds which then undergo amplification and recombination to form a high-power beam. A difference in the lengths of the fiber amplifiers 1 and 2 result in a frequency difference $\xi l_{12}/c$ at the locking point, where l_{12} is the path-length mismatch and c is the speed of light. An acousto-optic frequency shifter (AOFS) is placed in one of the arms to correct this frequency difference. For a linear chirp of $\frac{\xi}{2\pi} = 10^{15}$ Hz/s and a path-length mismatch of 10 cm in fiber, the required frequency shift is 500 kHz, which is well within the dynamic range of AOFSs. An optical phase-locked loop is formed by recording an interference signal between the two arms on a photodetector and feeding it back to the AOFS, as shown in figure 6.2 and figure 6.4. In lock, the AOFS synchronizes the optical phases and corrects

the fixed path-length mismatches as well as the dynamic length fluctuations arising from vibrations and temperature drift. The loop bandwidth determines the fastest fluctuation frequency that is suppressed, and previous work using AOFSs and single-frequency seeds has shown that sufficient bandwidths can be achieved for efficient combining of fiber amplifier outputs [90].

SBS suppression in high-power amplifiers scales with the chirp rate [35,36]. Therefore, we limit our attention to SFLs with perfectly linear chirps, in order to ensure that uniform SBS suppression is obtained throughout the duration of the frequency sweep. Moreover, a linear chirp enables path-length mismatches to be corrected by a constant frequency shift, as described above. Deviations from chirp linearity are corrected using a feedback loop, as long as these deviations are small and at frequencies within the loop bandwidth. It is therefore desirable that the chirp be close to perfectly linear, particularly at high chirp rates ξ, in order to relax the requirements on the frequency tuning range of the AOFS and the bandwidth of the feedback loop. We note that it should be possible to further extend the phase-locking approach to other sweep profiles, by using a time-varying frequency shift to compensate for the time-varying slope of the optical frequency chirp, e.g., using the iterative algorithm of section 3.2.3 to pre-distort the AOFS bias signal.

6.3.1 Homodyne Phase-Locking

We first consider the homodyne phase-locking configuration shown in figure 6.2. The output of an optoelectronic SFL is split into two arms using a fiber splitter. The goal of the experiment is to phase-lock the outputs of the two arms by feeding back the error signal generated using a 2×2 fiber coupler and a balanced detector. The bias frequencies and phase shifts of the two AOFSs are denoted by ω_1, ω_2 and ϕ_1, ϕ_2. The differential delay between the first and second arms is denoted by τ_{12}. We also introduce a common delay τ_d to model the long fiber length inside an optical amplifier. The feedback loop is very similar to a typical phase-locked loop [51], and can be analyzed accordingly. We define the DC loop gain K_{DC} as the product of the

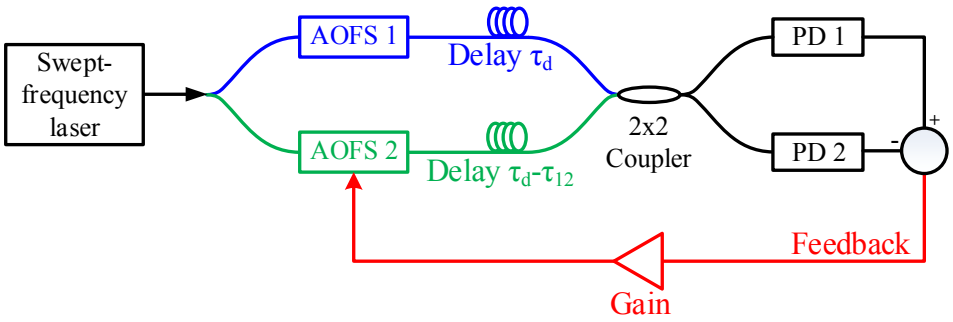

Figure 6.2: Passive-fiber chirped-wave optical phase-locked loop in the homodyne configuration. PD: Photodetector

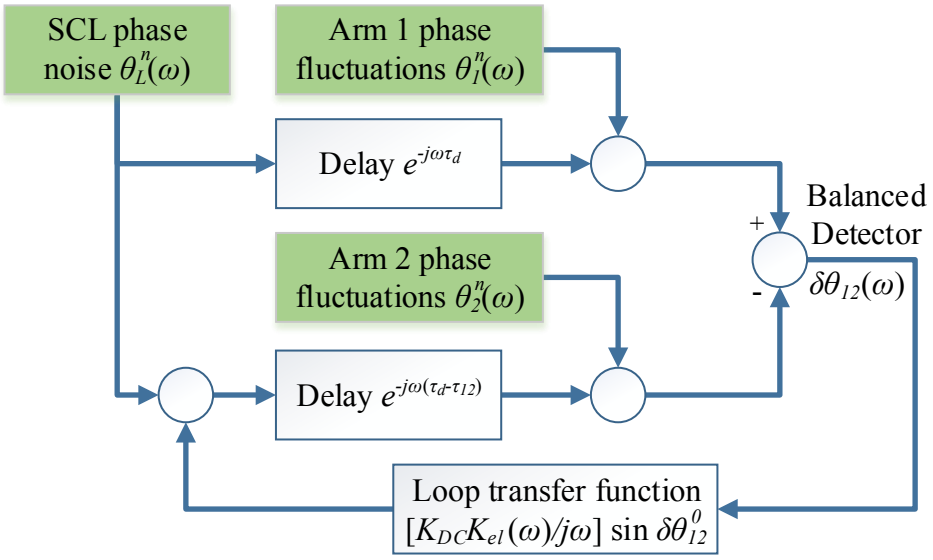

Figure 6.3: Small-signal frequency-domain model of the homodyne chirped-wave optical phase-locked loop. The model is used to study the effect noise and fluctuations (green blocks) on the loop output variable $\delta\theta_{12}(\omega)$.

optical power in each arm (units: W), and the gains of the balanced detector (V/W), loop amplifier (V/V), and frequency shifter (rad/s/V). Let the SFL optical frequency be given by equation (6.1), and let us denote the optical phases of the two arms at the coupler by $\theta_1(t)$ and $\theta_2(t)$. The optical phase difference between the two arms is given by

$$\begin{aligned}\theta_{12}(t) &\equiv \theta_1(t) - \theta_2(t) \\ &= (\omega_{L,0} + \omega_1)(t - \tau_d) + \frac{\xi}{2}(t - \tau_d)^2 + \phi_1 - (\omega_{L,0} + \omega_2)(t + \tau_{12} - \tau_d) \\ &- \frac{\xi}{2}(t + \tau_{12} - \tau_d)^2 - \phi_2 - \int_0^{t+\tau_{12}-\tau_d} K_{DC} \cos\theta_{12}(u)du = \\ &= \Delta\omega_{fr}(t - \tau_d) - (\omega_2 + \omega_{L,0})\tau_{12} - \frac{\xi\tau_{12}^2}{2} + \phi_{12} - \int_0^{t+\tau_{12}-\tau_d} K_{DC} \cos\theta_{12}(u)du,\end{aligned} \tag{6.2}$$

where $\Delta\omega_{fr} \equiv \omega_1 - \omega_2 - \xi\tau_{12}$ is the free-running frequency difference between the two arms, and $\phi_{12} \equiv \phi_1 - \phi_2$. The final term in equation (6.2) represents the phase shift due to the feedback to the AOFS, which is the integral of the frequency shift. The steady-state solution θ_{12}^0, obtained by setting the time derivative of $\theta_{12}(t)$ to 0, is given by

$$\theta_{12}^0 = \cos^{-1}\left(\frac{\Delta\omega_{fr}}{K_{DC}}\right). \tag{6.3}$$

We use this result to rewrite equation (6.2),

$$\theta_{12}(t) = \Delta\omega_{fr}(t + \tau_{12} - \tau_d) + \theta_{12}^0 - \int_0^{t+\tau_{12}-\tau_d} K_{DC} \cos\theta_{12}(u)du. \tag{6.4}$$

In lock, the optical phases of the two arms differ by θ_{12}^0, and there is no frequency difference.

Next, we linearize the loop about its steady-state solution in order to study dynamic behavior and the effect of fluctuations. We denote the phase noise and residual nonlinearity of the SFL by $\theta_L^n(t)$, and the phase noise introduced in the two arms by $\theta_1^n(t)$ and $\theta_2^n(t)$, which include noise contributions from the AOFSs and fluctuations in the optical path lengths. We introduce $\delta\theta_{12}(t)$, the small-signal fluctuation of $\theta_{12}(t)$

about the steady state, so that

$$\theta_{12}(t) = \theta_{12}^0 + \delta\theta_{12}(t). \tag{6.5}$$

We plug equation (6.5) into equation (6.4), and expand about the steady-state point (equation (6.3)). Solving for $\delta\theta_{12}(t)$, we arrive at

$$\delta\theta_{12}(t) = \theta_{12}^n(t) + \theta_L^n(t-\tau_d) - \theta_L^n(t+\tau_{12}-\tau_d) + K_{DC}\sin\theta_{12}^0 \int_0^{t+\tau_{12}-\tau_d} \delta\theta_{12}(u)du, \tag{6.6}$$

where $\theta_{12}^n(t) \equiv \theta_1^n(t) - \theta_2^n(t)$. Taking the Fourier transform of both sides of equation (6.6), we arrive at a frequency-domain description of the small-signal fluctuations,

$$\begin{aligned}\delta\theta_{12}(\omega) = \theta_{12}^n(\omega) + \theta_L^n(\omega)\left[e^{-j\omega\tau_d} - e^{-j\omega(\tau_d-\tau_{12})}\right] \\ + \frac{K_{DC}K_{el}(\omega)\sin\theta_{12}^0}{j\omega} e^{-j\omega(\tau_d-\tau_{12})}\delta\theta_{12}(\omega),\end{aligned} \tag{6.7}$$

where $K_{el}(\omega)$ is the frequency-dependent gain of the loop electronics. This frequency-domain model is shown schematically in figure 6.3. The solution of equation (6.7) is given by

$$\delta\theta_{12}(\omega) = \frac{\theta_{12}^n(\omega)}{1+K(\omega)} + \frac{\theta_L(\omega)\left[e^{-j\omega\tau_d} - e^{-j\omega(\tau_d-\tau_{12})}\right]}{1+K(\omega)}, \tag{6.8}$$

where

$$\begin{aligned}K(\omega) &\equiv -\frac{K_{DC}K_{el}(\omega)\sin\theta_{12}^0}{j\omega} e^{-j\omega(\tau_d-\tau_{12})} \\ &= \frac{K_{DC}K_{el}(\omega)\sqrt{1-\left(\frac{\Delta\omega_{fr}}{K_{DC}}\right)^2}}{j\omega} e^{-j\omega(\tau_d-\tau_{12})}\end{aligned} \tag{6.9}$$

is the total frequency-dependent feedback gain, and we picked the negative root in calculating $\sin\theta_{12}^0$ in order to achieve negative feedback.

In our experiments, loop bandwidths have been limited to the sub-MHz range by the AOFS frequency modulation response, and we therefore restrict our attention to the Fourier frequency range below $\sim$ 10 MHz. Typical values of τ_{12} are in the ns

range, so $\omega\tau_{12} \lesssim 10^{-2}$, and we can expand equation (6.8) and equation (6.9) near $\omega\tau_{12} = 0$, yielding

$$\delta\theta_{12}(\omega) = \frac{\theta_{12}^{n}(\omega)}{1 + K(\omega)} - j\omega\tau_{12}\frac{\theta_L(\omega)e^{-j\omega\tau_d}}{1 + K(\omega)}, \text{ and} \tag{6.10}$$

$$K(\omega) = \frac{K_{DC}K_{el}(\omega)\sqrt{1 - \left(\frac{\Delta\omega_{fr}}{K_{DC}}\right)^2}}{j\omega}e^{-j\omega\tau_d}. \tag{6.11}$$

According to equation (6.10), phase fluctuations in the fiber are reduced by a factor $1 + K(\omega)$ in the locked state. For frequencies within the loop bandwidth, $K(\omega) \gg 1$, and significant noise suppression is obtained. The second term describes the effect of the SFL phase noise and residual chirp nonlinearity. The system behaves like a frequency discriminator with gain τ_{12}, and the feedback again suppresses the measured frequency noise by the factor $1 + K(\omega)$. It is clear that a small differential delay τ_{12} and an SFL with a highly linear chirp and low phase noise minimize the phase error in the loop.

The homodyne phase-locking approach described above has a few shortcomings.

1. The value of the steady-state phase θ_{12}^0 can only be adjusted (within the range $[0, \pi]$) by varying the bias frequency shifts ω_1 and ω_2; this is not optimal since it adversely impacts loop gain and therefore performance.

2. The desired operating point for in-phase beam combining is $\theta_{12}^0 \approx 0$; however, according to equation (6.9), the loop gain contains the factor $\sin\theta_{12}^0$, and the loop therefore loses lock as this operating point is approached. It is desirable that the loop be locked at quadrature $\theta_{12}^0 = \pi/2$, maximizing the gain.

3. Finally, it is not straightforward to scale this approach to multiple phase-locked arms.

These problems are all addressed by adopting a heterodyne phase-locking architecture, as described in the next section.

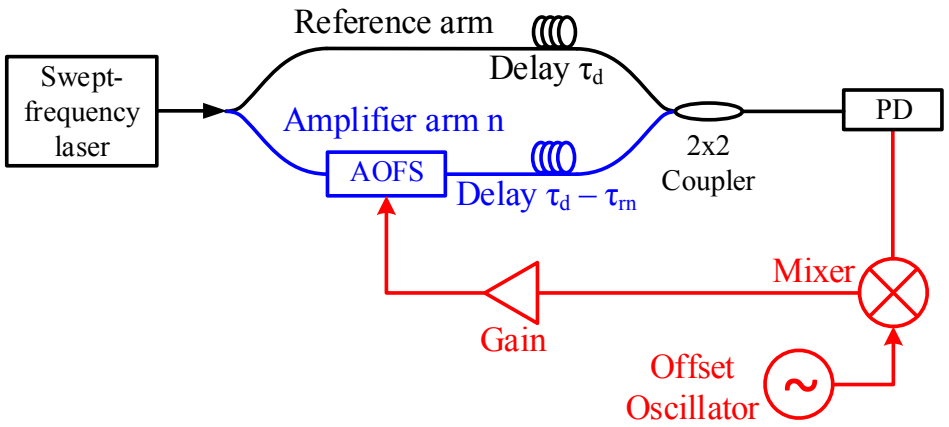

Figure 6.4: Passive-fiber chirped-wave optical phase-locked loop in the heterodyne configuration. PD: Photodetector

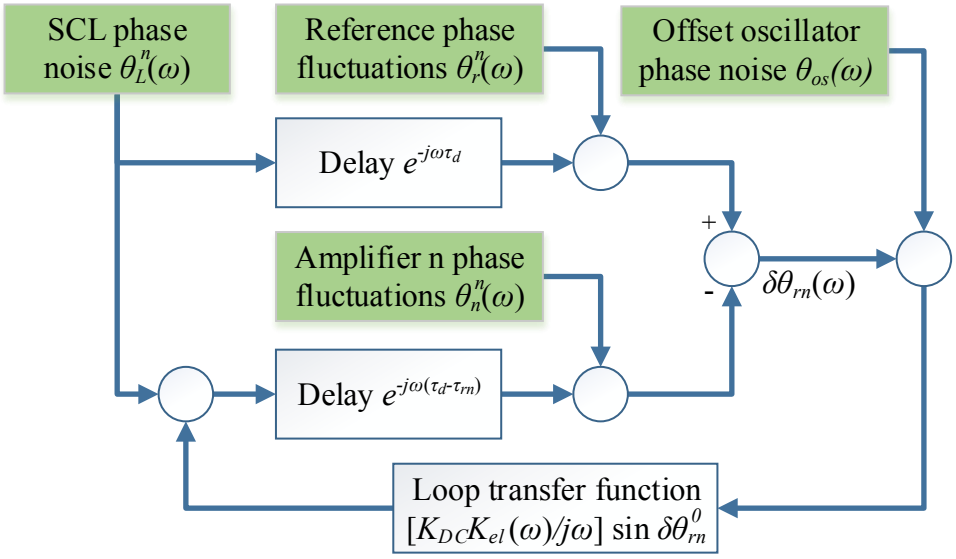

Figure 6.5: Small-signal frequency-domain model of the heterodyne chirped-wave optical phase-locked loop. The model is used to study the effect noise and fluctuations (green blocks) on the loop output variable $\delta\theta_{rn}(\omega)$.

6.3.2 Heterodyne Phase-Locking

In a heterodyne chirped-seed CBC experiment, the SFL output is split into a reference and multiple amplifier arms. The goal of the experiment is to lock the phases of all the amplifier arms to the reference, at an offset frequency ω_{os}. The heterodyne OPLL formed between the reference and the n-th amplifier is shown in figure 6.4. The bias frequency and phase shift of the AOFSs is denoted by ω_n and ϕ_n. The differential delay between the reference and amplifier arms is denoted by τ_{rn}, and we again introduce a common delay τ_d. The optical phase difference between the two arms is given by

$$\begin{aligned}\theta_{rn}(t) = (-\omega_n - \xi\tau_{rn})(t-\tau_d) - (\omega_n + \omega_{L,0})\tau_{rn} - \frac{\xi\tau_{rn}^2}{2} - \phi_n \\ - \int_0^{t+\tau_{rn}-\tau_d} K_{DC}\cos\left[\theta_{rn}(u) + \omega_{os}u + \theta_{os,n}\right] du,\end{aligned} \tag{6.12}$$

where $\theta_{os,n}$ is the phase of the offset oscillator in the n-th OPLL. The steady-state solution $\theta_{rn}^0(t)$, obtained by setting the time derivative of the mixer phase $\theta_{rn}(t) + \omega_{os}t + \theta_{os}$ to 0, is given by

$$\theta_{rn}^0(t) = -\omega_{os}t - \theta_{os,n} + \cos^{-1}\left(\frac{\Delta\omega_{fr}}{K_{DC}}\right), \tag{6.13}$$

where $\Delta\omega_{fr} = \omega_{os} - \omega_n - \xi\tau_{rn}$. We use this result to rewrite equation (6.12),

$$\theta_{rn}(t) = \Delta\omega_{fr}(t + \tau_{rn} - \tau_d) + \theta_{rn}^0(t) - \int_0^{t+\tau_{rn}-\tau_d} K_{DC}\cos\left[\theta_{rn}(u) + \omega_{os}u + \theta_{os,n}\right] du. \tag{6.14}$$

If we acquire lock at a zero free-running frequency difference, the steady-state optical phase difference between the $n = 1$ and $n = 2$ amplifier arms is given by

$$\theta_{12}^0 = \theta_{r2}^0(t) - \theta_{r1}^0(t) = \theta_{os,1} - \theta_{os,2} \equiv \theta_{os,12}. \tag{6.15}$$

The steady-state phase difference between the two amplifier arms can now be controlled electronically by setting the relative offset oscillator phase $\theta_{os,12}$. Loop oper-

ation off quadrature is therefore no longer required. The electronic phase control is also important for beam-steering and phase-controlled optical apertures.

Next, we linearize the loop about its steady-state solution. We denote the phase noise introduced in the reference and amplifier arms by $\theta_r^n(t)$ and $\theta_n^n(t)$, and offset oscillator phase noise by $\theta_{os,n}^n(t)$. We introduce $\delta\theta_{rn}(t)$, the small-signal fluctuation of $\theta_{rn}(t)$ about the steady state, so that

$$\theta_{rn}(t) = \theta_{rn}^0(t) + \delta\theta_{rn}(t). \tag{6.16}$$

We plug equation (6.16) into equation (6.14), and expand about the steady-state point (equation (6.13)). Solving for $\delta\theta_{rn}(t)$, we arrive at

$$\begin{aligned}\delta\theta_{rn}(t) = {} & \theta_{rn}^n(t) + \theta_L^n(t-\tau_d) - \theta_L^n(t+\tau_{rn}-\tau_d) \\ & - K_{DC}\sqrt{1-\left(\frac{\Delta\omega_{fr}}{K_{DC}}\right)^2}\int_0^{t+\tau_{rn}-\tau_d}\left[\delta\theta_{rn}(u) + \theta_{os,n}^n(t)\right]du.\end{aligned} \tag{6.17}$$

When locked at quadrature, the frequency-domain description of the small-signal fluctuations is given by

$$\delta\theta_{rn}(\omega) = \theta_{rn}^n(\omega) - j\omega\tau_{rn}e^{-j\omega\tau_d}\theta_L^n(\omega) - K(\omega)\left[\delta\theta_{rn}(\omega) + \theta_{os,n}^n(\omega)\right], \tag{6.18}$$

where

$$K(\omega) \equiv \frac{K_{DC}K_{el}(\omega)\sqrt{1-\left(\frac{\Delta\omega_{fr}}{K_{DC}}\right)^2}}{j\omega}e^{-j\omega(\tau_d-\tau_{rn})}, \tag{6.19}$$

and we have introduced the frequency-dependent electronic gain $K_{el}(\omega)$. This small-signal model is shown schematically in figure 6.5. The solution of equation (6.18) is given by

$$\delta\theta_{rn}(\omega) = \frac{\theta_{rn}^n(\omega)}{1+K(\omega)} - j\omega\tau_{rn}\frac{\theta_L(\omega)e^{-j\omega\tau_d}}{1+K(\omega)} - \frac{K(\omega)\theta_{os,n}^n(\omega)}{1+K(\omega)}. \tag{6.20}$$

As in the homodyne case, for frequencies within the loop bandwidth, the OPLL reduces the phase error due to fiber fluctuations and SFL phase noise by a factor $1+K(\omega)$. The factor multiplying the offset phase noise term $\theta_{os,n}^n(\omega)$ goes to 1 for

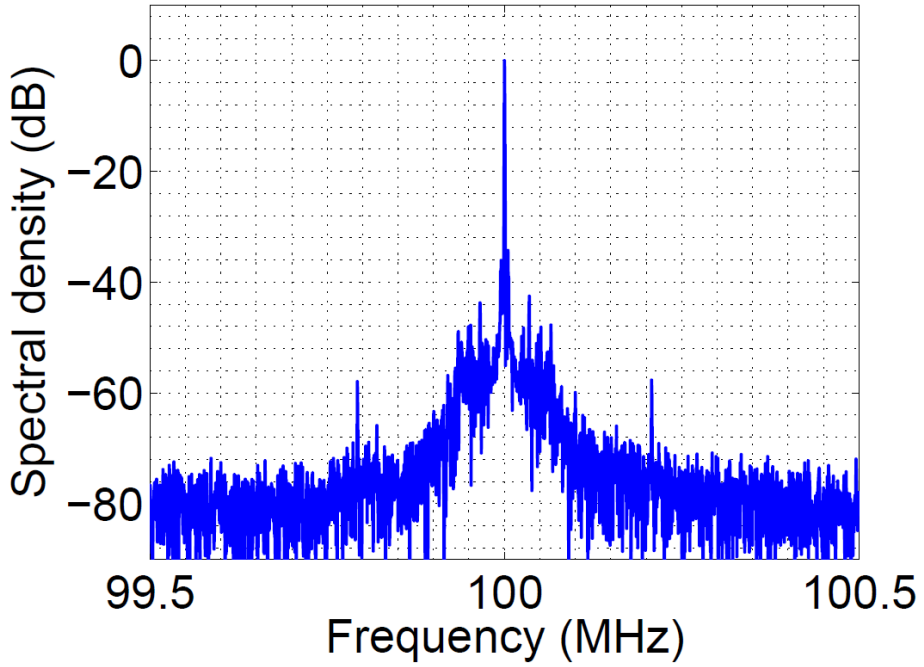

Figure 6.6: Locked-state Fourier spectrum of the measured beat signal between the reference and amplifier arms, over a 2 ms chirp interval. The nominal loop delay parameters are $\tau_d = 20$ m and $\tau_{r1} \approx 0$ m. The time-domain signal was apodized with a Hamming window.

large $K(\omega)$. The offset oscillator phase noise is transferred to the optical wave, and should be kept as small as possible.

6.3.3 Passive-Fiber Heterodyne OPLL

The heterodyne phase-locking experiment of figure 6.4 was performed at 1550 nm using a VCSEL-based optoelectronic SFL with a chirp rate of 2×10^{14} Hz/s (see chapter 3 for a summary of its operation). We used polarization-maintaining fiber-optic components, and an AOFS (Brimrose Corporation) with a nominal frequency shift of 100 MHz and a frequency modulation bandwidth of ~ 75 kHz. We used a DDS integrated circuit to provide the 100 MHz offset signal. The circuit can rapidly switch the output amplitude, phase and frequency when driven by an external trigger, which allowed us to use different locking parameters for the up and down chirps. Similarly, we designed a triggered arbitrary waveform generator in order to vary the AOFS bias during the up and down chirps. The experiment was performed for different values

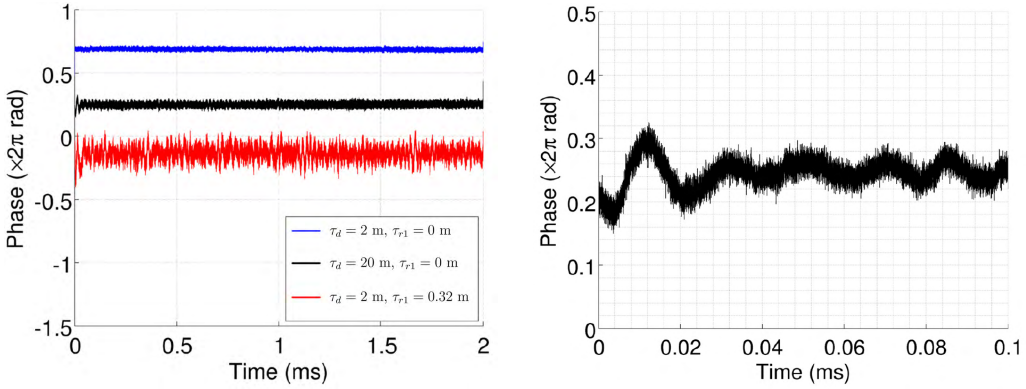

(a) (b)

Figure 6.7: (a) Phase difference between the reference and amplifier arms calculated using the I/Q demodulation technique. The three curves (offset for clarity) correspond to different values of the loop delay τ_d and the path-length mismatch τ_{r1}. (b) Transient at the beginning of the chirp. The locking time is determined by the loop bandwidth, which is limited by the AOFS to about 60 KHz.

of the loop propagation delay τ_d and path-length mismatch τ_{r1}.[1]

We measured the beat signal between the reference and amplifier arms in order to characterize the performance of the heterodyne OPLL. The locked-state beat signal phase fluctuations, $\delta\theta_{r1}(t)$, are described in the frequency domain by equation (6.20). The variance of these phase fluctuations, $\langle \delta\theta_{r1}^2(t) \rangle_t$, is the critical metric of loop performance since it determines the fraction of the amplifier power that is coherent with the reference path [8, 104]. The spectrum of the beat signal over one 2 ms chirp duration is calculated using a Fourier transform with a Hamming window, and is shown in figure 6.6. The delay parameters were $\tau_d = 20$ m and $\tau_{r1} \approx 0$. The spectrum comprises a transform-limited peak at 100 MHz and a small noise pedestal. The loop bandwidth is about 60 kHz, limited by the AOFS. The residual noise may be calculated by integrating the noise in the spectral measurement [8, 104]. From figure 6.6, the standard deviation of the phase fluctuations is calculated to be 0.08 rad, which corresponds to 99.4% of the amplifier optical power being coherent with the reference wave.

An alternative means of analysis is to use the in-phase and quadrature (I/Q)

[1]The optical delay is reported here in units of length, and is to be understood as the time taken for light to propagate along that length of polarization-maintaining Panda fiber.

demodulation technique, as described in appendix A. It allows us to extract the time-domain phase fluctuations $\delta\theta_{r1}(t)$, and directly calculate the variance $\langle\delta\theta_{r1}^2(t)\rangle_t$. The locked-state phase fluctuations during one 2 ms chirp are plotted in figure 6.7a for three different values of the loop delay τ_d and the differential delay τ_{r1} (the curves are offset from each other for clarity). The locking transient is shown in figure 6.7b. The locking time is determined by the loop bandwidth, which is limited by the AOFS to about 60 KHz.

We calculated the phase error standard deviations and locking efficiencies for different delays, and the results are tabulated in table 6.1. For a given differential delay, the addition of a large loop delay $\tau_d = 20$ m slightly reduces the bandwidth of the loop, resulting in a marginally lower phase-locking efficiency. On the other hand, for a given loop delay, the addition of $\tau_{r1} = 32$ cm of differential delay results in an increased amount of SFL phase noise affecting the loop, as predicted by equation (6.20). This reduces the locking efficiency from $\sim 99\%$ to $\sim 90\%$. Differential delays much smaller than 32 cm are trivially achieved in practice, and correspond to phase-locking efficiencies larger than 90%.

Loop delay τ_d (m)	Differential delay τ_{r1} (cm)	Phase error std. dev. $\sigma_{r1} = \langle\delta\theta_{r1}^2(t)\rangle_t^{1/2}$ (mrad)	Locking efficiency $\eta = \frac{1}{1+\sigma_{r1}^2}$
2	0	47	99.8%
2	32	279	92.8%
20	0	76	99.4%
20	32	315	91.0%

Table 6.1: Measured OPLL phase error standard deviation and phase-locking efficiency for different values of the loop delay τ_d and the differential delay τ_{r1}

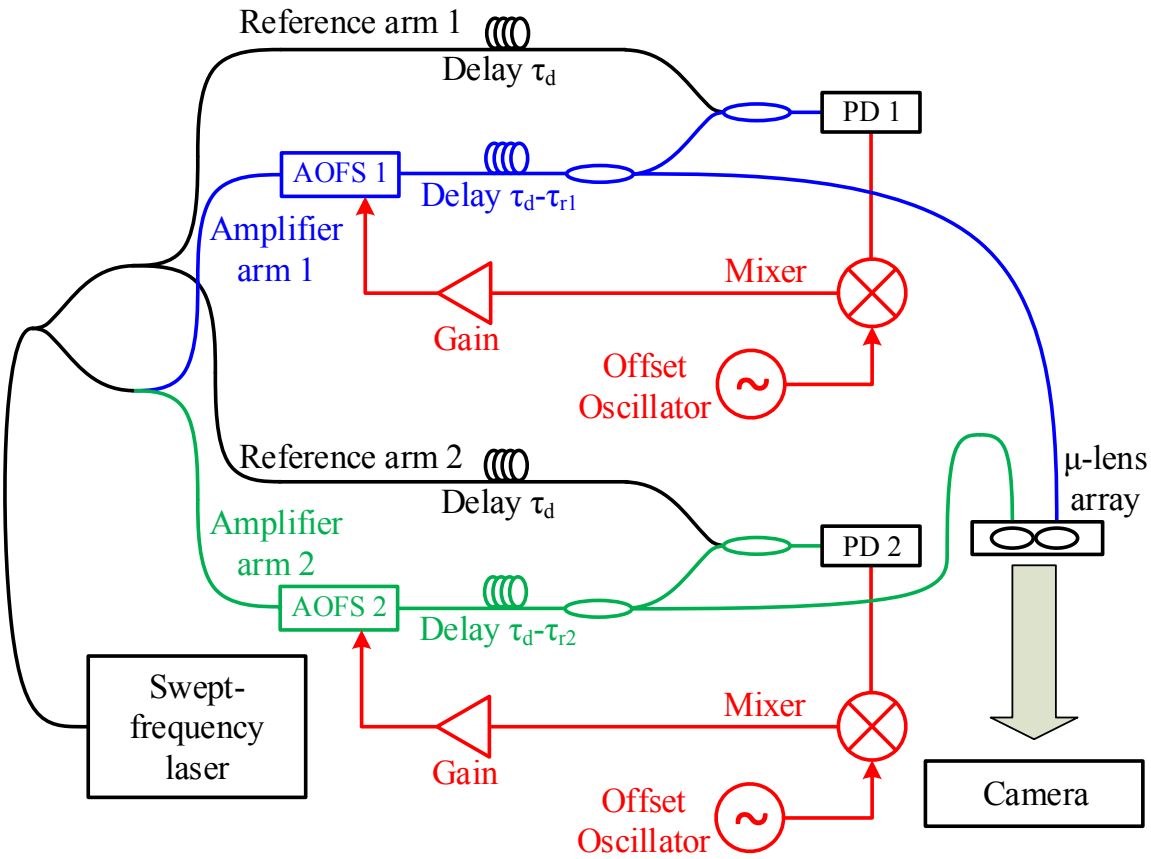

Figure 6.8: Schematic diagram of the passive-fiber chirped-seed CBC experiment with two channels. Heterodyne optical phase-locked loops are used to lock the amplifier (blue, green) and reference (black) arms. The outputs of the amplifier arms are coupled to a microlens (μ-lens) array to form a two-element tiled-aperture beam combiner. The far-field intensity distribution of the aperture is imaged on a CCD camera.

6.4 Coherent Combining of Chirped Optical Waves

6.4.1 Passive-Fiber CBC Experiment

To demonstrate beam combining and electronic beam steering, we constructed two separate heterodyne OPLLs, as shown in figure 6.8. The SFL output was split into a reference arm and two amplifier channels. The reference arm was further split into two, and delivered to the two OPLLs. The two loops were locked using electronic offset signals that were provided by a pair of synchronized DDS oscillators, with individually controllable amplitudes and phases. We measured the OPLL photocurrents in each loop for three values of the loop delay τ_d and differential delays τ_{r1} and τ_{r2}. The calculated spectra and demodulated phases are shown in figure 6.9 for $\tau_d \approx 0$ m, $\tau_{r1} = \tau_{r2} \approx 0$ cm, figure 6.10 for $\tau_d \approx 18$ m, $\tau_{r1} = \tau_{r2} \approx 0$ cm, and figure 6.11 for $\tau_d \approx 18$ m, $\tau_{r1} = \tau_{r2} \approx 32$ cm. The performance of the two loops is essentially identical. The same trend that is described above is evident in these figures—a large loop delay τ_d only slightly affects the loop bandwidth and marginally increases the measured noise levels, while the addition of a differential delay τ_{r1} or τ_{r2} increases the effect of SFL phase noise, causing a noticeable increase in the spectra pedestals and phase deviations.

The outputs of the two amplifier paths (after the AOFSs and additional fiber delays) were used to form a coherent aperture using a fiber V-groove array placed at the focal plane of a microlens array. The emitter spacing was 250 μm. A CCD camera was used to image the far-field intensity distribution of the aperture over many chirp periods. The delays in the fiber paths that deliver the amplifier channels to the microlens array are not compensated for by the OPLLs, which yields an optical frequency difference between the two channels at the aperture. We solved this issue by simply phase-locking the two loops at slightly different offset frequencies, so as to get a stable fringe pattern on the camera. Moreover, we isolated these fibers using a vibration-damping polymer sheet, in order to minimize the fluctuations in their path

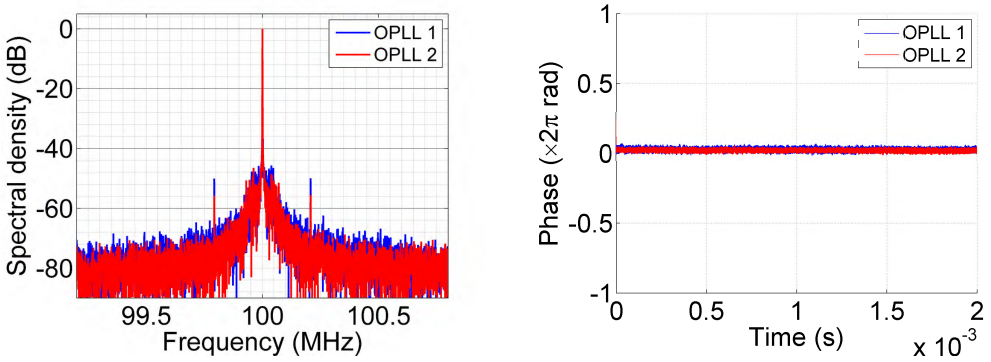

(a) OPLL spectra. (b) I/Q-demodulated OPLL phases.

Figure 6.9: Characterization of the two heterodyne OPLLs in the locked state. $\tau_d \approx 0$ m, $\tau_{r1} = \tau_{r2} \approx 0$ cm.

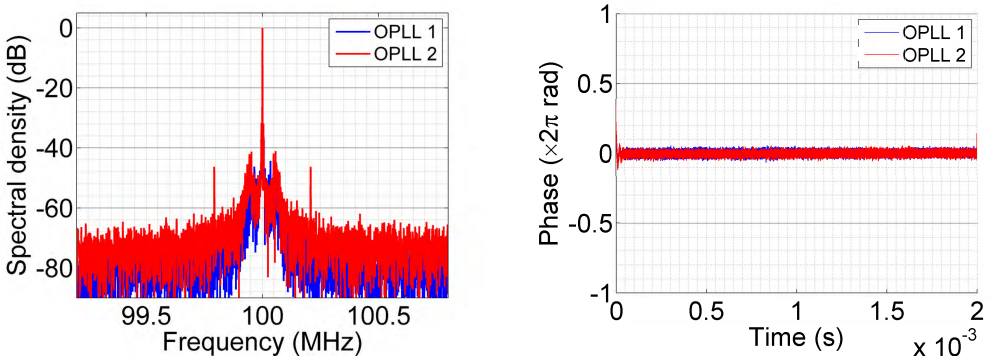

(a) OPLL spectra. (b) I/Q-demodulated OPLL phases.

Figure 6.10: Characterization of the two heterodyne OPLLs in the locked state. $\tau_d \approx 18$ m, $\tau_{r1} = \tau_{r2} \approx 0$ cm.

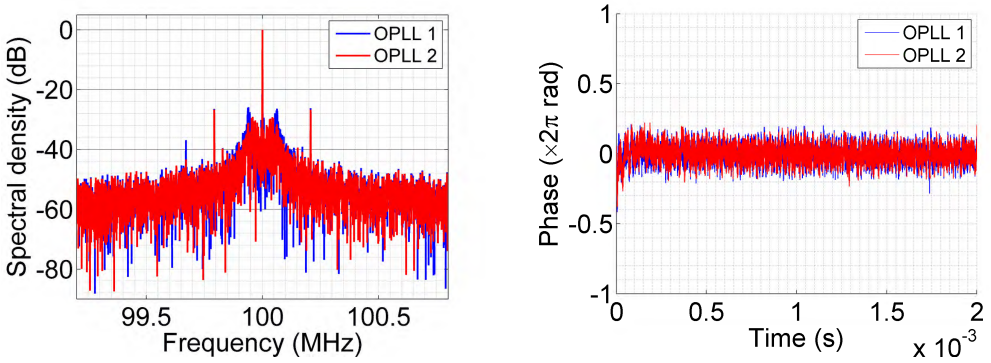

(a) OPLL spectra. (b) I/Q-demodulated OPLL phases.

Figure 6.11: Characterization of the two heterodyne OPLLs in the locked state. $\tau_d \approx 18$ m, $\tau_{r1} = \tau_{r2} \approx 32$ cm.

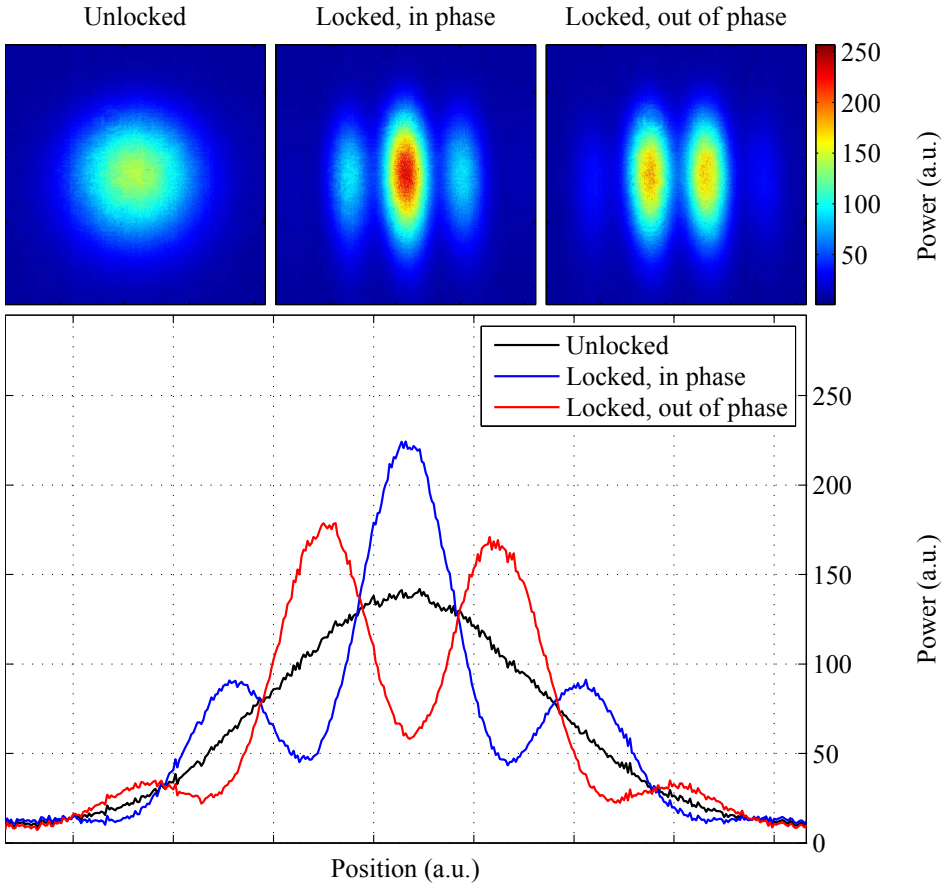

Figure 6.12: Experimental demonstration of electronic phase control and beam steering of chirped optical waves. (a) Far-field intensity profiles for the unlocked and phase-locked cases. The position of the fringes is controlled by varying the phase of the electronic oscillator in one loop. (b) Horizontal cross sections of the far-field intensity patterns

lengths. It is important to note that these efforts are not necessary in the free-space experiment of section 6.4.3

The far-field intensity distributions of the aperture in the locked and unlocked states are shown in figure 6.12. We observe a narrowing of the central lobe in the locked case vs. the unlocked case, and a corresponding increase in its intensity by a factor of 1.6. We also demonstrate electronic steering of the far-field intensity pattern by varying the phase of one of the offset oscillators, as shown in figure 6.12. The demonstrated coherent-combining approach also scales well to larger systems,

since the combination of coherent signal gain and incoherent phase errors leads to an increasing interferometric visibility with increasing number of array elements [105].

6.4.2 Combining Phase Error in a Heterodyne Combining Experiment

We briefly revisit the small-signal residual phase error analysis. So far we have focused on measuring phase errors between the reference and amplifier arms, which is useful in characterizing the OPLL performance. However, in a dual-channel combining experiment, the relevant phase error is the combining error $\delta\theta_{12}(\omega)$, given by

$$\delta\theta_{12}(\omega) \equiv \delta\theta_{r2}(\omega) - \delta\theta_{r1}(\omega) \tag{6.21}$$

Plugging in equation (6.20), we arrive at

$$\delta\theta_{12}(\omega) = \frac{\theta_{12}^{n}(\omega)}{1+K(\omega)} - j\omega\tau_{12}\frac{\theta_L(\omega)e^{-j\omega\tau_d}}{1+K(\omega)}, \tag{6.22}$$

where θ_{12}^{n} is the relative path-length fluctuation of the two amplifier arms. In deriving equation (6.22), we have assumed equal gains in the two OPLLs, and neglected the contribution of the offset oscillator noise.

In the experiment of section 6.4.1, we learned that the amount of differential path-length mismatch essentially determines the locked-state noise levels. From equation (6.22), it is clear that the combining noise level is actually determined by $\tau_{12} = \tau_{r2} - \tau_{r1}$, the path-length mismatch between the two amplifier arms, and not by τ_{r1} or τ_{r2} alone.

6.4.3 Free-Space Beam Combining of Erbium-Doped Fiber Amplifiers

A schematic of the dual-channel chirped-seed amplifier (CSA) CBC experiment is shown in figure 6.13. An optoelectronic SFL based on a 1550 nm VCSEL is linearly

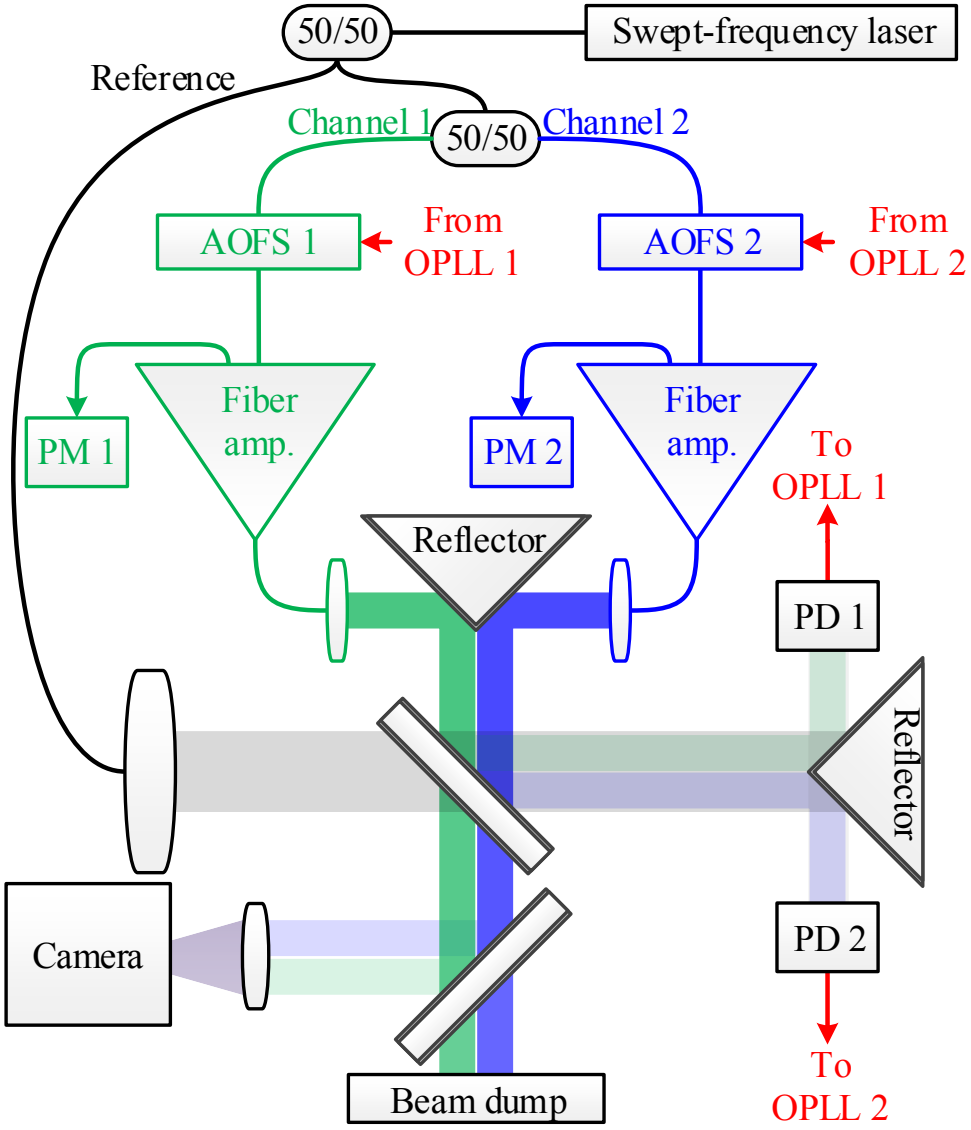

Figure 6.13: Schematic diagram of the dual-channel CSA coherent-combining experiment. PD: Photodetector, PM: Back-scattered power monitor

chirped over a bandwidth of 500 GHz in 1 ms, resulting in a sweep rate $\xi/(2\pi) = 5 \times 10^{14}$ Hz/sec. At the end of the 1 ms sweep time, the laser is chirped in reverse at the same rate, bringing it back to its original starting frequency. Channels 1 and 2 are boosted to powers of ~ 3 W each with commercially available erbium-doped fiber amplifiers.

The back-scattered power from the 5 m final amplifier stage and the 45 m delivery fiber is recorded for each channel. We define the stimulated Brillouin scattering threshold as the power level at which the ratio of the back-scattered power to the forward power is 10^{-4}. We report a threefold increase in the SBS threshold for the 5×10^{14} Hz/sec chirp rate, when compared to a single-frequency seed.

Synchronized DDS circuits are used as offset oscillators in the two heterodyne OPLLs. An offset frequency of 100 MHz is chosen to match the nominal acousto-optic frequency shift. A tiled-aperture is formed using a 90° prism with reflecting legs, and its far-field distribution is imaged onto a phosphor-coated CCD camera with a lens.

Intensity distributions of the individual channels, as well as that of the locked aperture are shown in figure 6.14. The path lengths are nominally matched, with $l_{12} = 20$ mm. This level of path-length matching is easily achieved. We observe, in the locked state, a twofold narrowing of the central lobe and an associated increase in the peak lobe intensity. The phases of the individual emitters track the phases of the DDS oscillators, and we are therefore able to electronically steer the combined beam. Intensity distributions corresponding to relative DDS phases of $\theta_{os,12} = 0$, $\pi/2$, π, and $3\pi/2$ radians are shown in figure 6.15.

We extract the time-dependent phase differences between the reference and amplifier channels from the two photodetector signals. The phase differences corresponding to the four values of $\theta_{os,12}$ are shown figure 6.16. As expected, the OPLL phases, and hence the phases of the individual chirped waves track the DDS setpoint.

To characterize performance, we consider three path-length matching cases, summarized in Table 6.2. The I/Q technique yields the residual phase errors, $\delta\theta_{r1}(t)$ and $\delta\theta_{r2}(t)$. The time-domain combining phase error is then calculated using equation

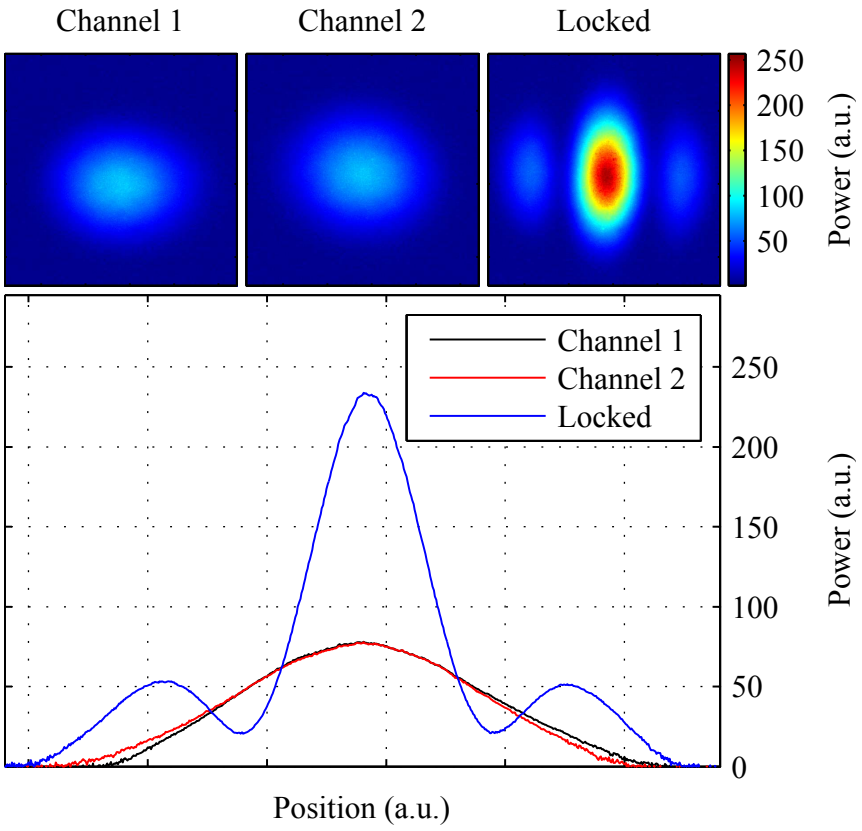

Figure 6.14: Far-field intensity distributions of the individual channels and the locked aperture. $\tau_{r1} = -19$ mm, and $\tau_{r2} = 1$ mm

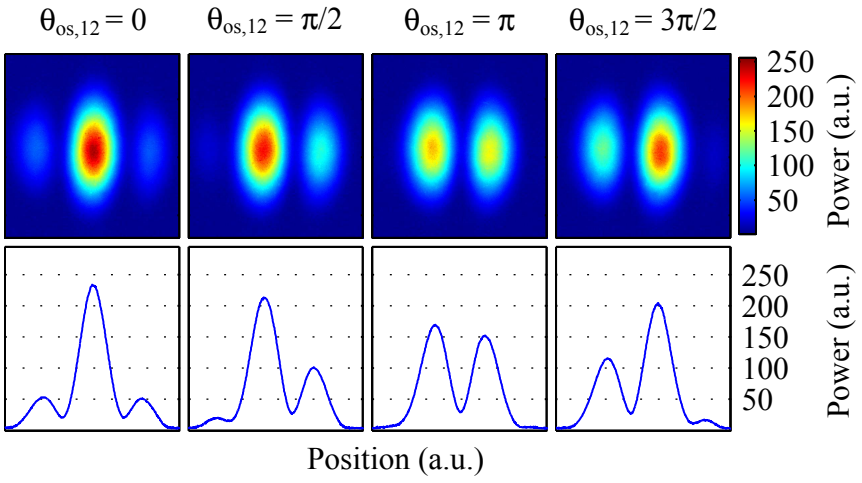

Figure 6.15: Steering of the combined beam through emitter phase control. $\theta_{os,12}$ is the relative DDS phase.

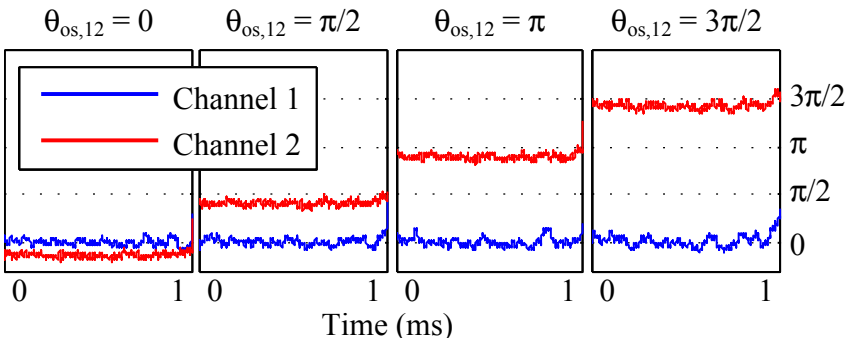

Figure 6.16: I/Q-demodulated phase differences between the amplifier channels and the reference. $\theta_{os,12}$ is the relative DDS phase.

(6.21). The standard deviations $\sigma_{xy} = \sqrt{\langle \delta\theta_{xy}^2(t) \rangle_t}$ of all three phase errors, along with the phase-noise-limited fringe visibilities are listed in table 6.2. The visibilities are calculated from the standard deviations σ_{12} using a Gaussian phase noise model, as described in appendix B.

The first case (nominally path-length-matched) has the lowest combining error, which is consistent with equation (6.22). The second and third cases have nearly identical amplifier path-length mismatches and exhibit nearly identical combining phase errors. This is consistent with the prediction that the residual combining error is determined solely by the mismatch between the amplifier channels.

The phase-noise-limited fringe visibility for the path-length-matched case is almost 99%, yet the fringe visibility in figure 6.14 is only about 80%. We believe the discrepancy is due to the wavefront distortions introduced by the collimators and the prism reflectors.

6.5 Summary

We have analyzed and experimentally demonstrated the phase-locking of chirped optical waves in a master oscillator power amplifier configuration. The precise chirp linearity of the optoelectronic SFL enables non-mechanical compensation of optical delays using acousto-optic frequency shifters, and is at the heart of our chirped phase-locking and coherent-combining systems.

We have demonstrated heterodyne phase-locking of optical waves with a chirp rate of 5×10^{14} Hz/sec at 1550 nm, achieving a loop bandwidth of 60 kHz and a phase error variance less than 0.01 rad^2. We used the heterodyne OPLL architecture to construct a dual-channel passive-fiber coherent beam combining experiment, and have demonstrated coherent combining and electronic beam steering of chirped optical waves.

We have also implemented and characterized a 1550 nm chirped-seed amplifier coherent-combining system. We used a chirp rate of 5×10^{14} Hz/sec, which resulted in a threefold increase of the amplifier SBS threshold, when compared to a single-frequency seed. We demonstrated efficient phase-locking and electronic beam steering of two 3 W erbium-doped fiber amplifier channels. We achieved temporal phase noise levels corresponding to fringe visibilities exceeding 90% at path-length mismatches of ≈ 300 mm, and exceeding 98% at a path-length mismatch of 20 mm.

The optoelectronic SFL has the potential to significantly increase the achievable output power from a single fiber amplifier by increasing its SBS threshold. Coherent beam combining techniques developed in this chapter can be used to efficiently combine multiple chirped amplifier outputs, without imposing strict path-length matching requirements, presenting a viable path towards high-power continuous-wave sources.

Case	Differential delay (mm)[a]			Phase error (mrad)			Fringe visibility
	τ_{r1}	τ_{r2}	τ_{12}	σ_{r1}	σ_{r2}	σ_{12}	$V = e^{-\sigma_{12}^2/2}$
1	−19	1	20	118	79.3	160	98.7%
2	110	450	340	184	531	428	91.3%
3	−118	220	338	150	273	410	92.0%

[a]These are fiber lengths corresponding to the time delays between the different paths. Actual mismatches have both free-space and fiber components.

Table 6.2: OPLL phase errors and phase-noise-limited fringe visibilities in the dual-channel active CBC experiment

Chapter 7

Conclusion

7.1 Summary of the Thesis

7.1.1 Development of the Optoelectronic SFL

We have demonstrated the use of optoelectronic feedback for precise control over the optical chirp of a semiconductor laser diode. This system, the optoelectronic SFL, formed the backbone of all the work described in this thesis. The development of the optoelectronic SFL was guided by optical FMCW reflectometry and 3-D imaging applications. Specifically, we aimed to build a swept-source with narrow linewidth (for long-range imaging), linear frequency tuning (to reduce the processing overhead), and high chirp bandwidth (for high axial resolution), all on a compact platform without moving parts.

The optoelectronic SFL works like a PLL. A portion of the SCL light is launched into a Mach-Zehnder interferometer, and the loop locks the sinusoidal intensity fluctuation at the interferometer output to a reference electronic oscillator. The optoelectronic SFL, just as a regular PLL, only achieves lock if the feedback bandwidth is larger than the unlocked beat signal linewidth, which is determined by the free-running SCL chirp nonlinearity. As the SCL is chirped faster, the nonlinearity is increased, which lead to poor locking—our initial experiments were limited to a chirp rate of 10^{14} Hz/s for DFB lasers and 5×10^{14} for VCSELs. To improve the free-running sweep nonlinearity, we developed a bias current predistortion algorithm. Even though

the algorithm was based on a very naive nonlinear tuning model, it yielded impressive results when iterated. Using iterative predistortion we were able to significantly increase the chirp rates of our systems, up to 10^{15} Hz/s for DFB lasers and 10^{16} for VCSELs. We developed SFLs based on VCSELs and DFB lasers at wavelengths of 1550 nm and 1060 nm, and demonstrated their use in reflectometry and profilometry applications. Electronic development of the SFL undertaken as part of our work eventually lead to its commercialization by Telaris, Inc.

A key feature of the optoelectronic SFL, albeit not one that we recognized until after the first system was built and tested, is that successive chirps are exactly repeatable. The PLL locks not just the beat signal frequency, i.e., the instantaneous chirp rate, but also the beat signal phase, i.e., the starting chirp frequency. This means that each frequency sweep starts at the exact same point. As it turned out, stability of the starting sweep frequency was crucial for our work on MS-FMCW reflectometry and TomICam.

7.1.2 Ranging and 3-D Imaging Applications

7.1.2.1 MS-FMCW Reflectometry and Stitching

In an effort to increase the axial resolution of an SCL-based ranging system, we developed a novel variant of the FMCW optical imaging technique. This method, MS-FMCW reflectometry, uses multiple lasers that sweep over distinct but adjacent regions of the optical spectrum, in order to "stitch" a measurement with increased optical bandwidth and a corresponding improvement in the axial resolution. This technique bears resemblance to synthetic aperture radar, in which RF signals collected at multiple physical locations are used to approximate a large antenna aperture, and hence a high transverse resolution. In MS-FMCW reflectometry, the synthesized aperture is not physical, but instead represents the accessible optical frequency range.

The culmination of this work was an MS-FMCW system with four VCSEL channels, yielding a total chirp bandwidth of 2 THz and a scan time of 500 μs. This particular demonstration relied on hardware stitching to remove the need for addi-

tional signal processing that was present in our early MS-FMCW work. In a hardware stitching system, the SCL sweeps are locked to the same MZI with an electronic reference oscillator whose phase is not reset during channel switching. Because the starting frequencies of the sweeps are controlled exclusively by the reference oscillator phase, this configuration allowed perfect stitching to be performed in hardware. Each channel's chirp started precisely where the previous one ended!

7.1.2.2 The Tomographic Imaging Camera

One of the goals of our work is to enable rapid, high-resolution, and low-cost 3-D imaging without moving parts. The tomographic imaging camera was our solution to the problem of non-mechanical acquisition of transverse pixel information. TomICam uses low-cost full-field detector arrays to acquire depth information one transverse slice at a time. This is achieved by modulating the intensity of the transmitted beam with sinusoidal function, which shifts the signal spectrum to DC, allowing the use of low-speed integrating detector arrays, i.e., CCD and CMOS cameras. The depth of the slice is determined by the modulation frequency, and can therefore be tuned electronically. As a result, TomICam completely eliminates the need for moving parts traditionally employed in 3-D imaging.

We demonstrated basic TomICam functionality in a single-pixel proof-of-concept experiment at 1550 nm, and showed that the depth scan retrieved with TomICam is identical to the traditional FMCW measurement. It turns out that multiple measurements (two to four, depending on whether or not the imaging interferometer is balanced) at the same modulation frequency but different modulation phases are necessary to extract the depth information. This means that TomICam imaging would not be possible if there was appreciable starting frequency jitter between subsequent SFL sweeps. For TomICam, as for MS-FMCW, precise repeatability of the frequency sweeps generated by the optoelectronic SFL turned out to be a necessary requirement. We also discussed the application of compressive sensing to the TomICam platform, and showed, through computer simulations, that a tenfold improvement in the volume acquisition speed is possible for sufficiently sparse depth signals.

7.1.3 Phase-Locking and CBC of Chirped Optical Waves

Out group's current focus on the phase and frequency control of SCLs started a few years ago with phase-locking and coherent beam combining experiments that used commercially available, single-frequency semiconductor laser diodes. We have generalized these experiments to the case of chirped optical waves. The precise chirp linearity of the optoelectronic SFL enables non-mechanical compensation of optical delays using acousto-optic frequency shifters, and is at the heart of our chirped phase-locking and coherent-combining systems.

We have demonstrated heterodyne phase-locking of optical waves with a chirp rate of 5×10^{14} Hz/sec at 1550 nm, and constructed a dual-channel passive-fiber coherent beam combining experiment. We achieved efficient combining and demonstrated electronic beam steering of chirped optical waves by tuning the electronic offset oscillator phase in one of the heterodyne OPLLs.

The key physical result driving this work is that swept-frequency optical waveforms suppress stimulated Brillouin scattering (SBS) in fiber by reducing the effective length over which SBS occurs. This has the potential to increase the maximum output of high-power fiber amplifiers; and the chirped phase-locking techniques developed in this thesis can be used to form coherent amplifier arrays, further scaling the optical power. Conventional SBS suppression techniques result in a decrease of the seed laser coherence length, and coherent combining therefore requires very strict path-length matching. In practice, sub-mm matching is necessary at the kW power level. The chirped-seed combining approach developed in this thesis does not have strict matching requirements, due to the comparatively long coherence lengths of SCL-based SFLs, and therefore presents a viable path towards high-power continuous-wave sources.

We have also performed, for the first time, an active CBC experiment using a chirp rate of 5×10^{14} Hz/sec and two 3 W erbium-doped fiber amplifier channels. We recorded a threefold increase of the amplifier SBS threshold, when compared to a single-frequency seed. We demonstrated efficient phase-locking and electronic

beam steering of amplified chirped beams, and achieved temporal phase noise levels corresponding to fringe visibilities exceeding 90% at path-length mismatches of ≈ 300 mm, and exceeding 98% at a path-length mismatch of 20 mm.

7.2 Current and Future Work

The ground for continuing SFL development is fertile. One of the projects undertaken in our group, led by Yasha Vilenchik, is the integration of the optical components of the optoelectronic SFL on a hybrid Si/III-V integrated platform. Images of the subcomponents fabricated to date are shown in figure 7.1. The hybrid platform has the potential to bring photonic and electronic components together on a single bonded chip, and continuing development will one day yield a chip-scale chirped LIDAR transmitter.

Another interesting development in our group is the recent demonstration of a hybrid Si/III-V high-coherence semiconductor laser based on a modulated-bandgap design, shown in figure 7.2 [106]. The laser's high-Q resonator, designed and fabricated by Christos Santis, is contained entirely in silicon, and is therefore subject to much lower optical loss than traditionally used III-V resonators. This laser's chirp bandwidth is comparable to that of commercially available DFBs, while its linewidth is inherently superior. The use of this laser in an optoelectronic SFL will enable 3-D imaging systems that simultaneously possess long imaging range and high axial resolutions.

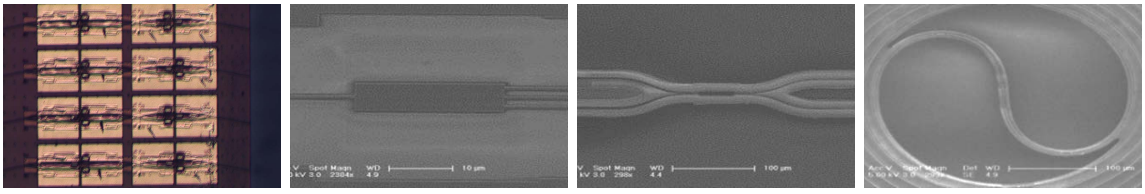

(a) (b) (c) (d)

Figure 7.1: (a) Hybrid Si/III-V DFB laser bar. (b) Scanning electron microscope (SEM) image of a 1×3 multimode interference (MMI) coupler, (c) SEM image of a 2×2 MMI coupler. (d) SEM closeup of the a spiral delay line for the loop MZI

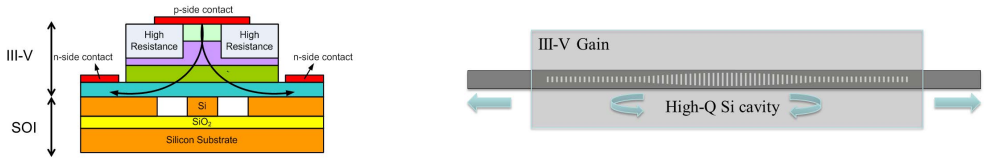

(a) (b)

Figure 7.2: Schematic of the hybrid Si/III-V high-coherence semiconductor laser. (a) Side-view cross section. (b) Top-view of the laser and the modulated-bandgap resonator

Development of narrow-linewidth swept-frequency lasers will also contribute to the group's label-free biomolecular sensing project, led by Jacob Sendowski. The sensor comprises an ultra-high-Q SiN microdisk resonator and a microfluidic analyte delivery system [15], as shown in figure 7.3. Biomolecular binding events shift the microdisk resonance frequency, which is detected using the optoelectronic SFL. Long-term repeatability of the starting frequency of SFL sweeps was a deciding factor in using it to interrogate the biomolecular sensor. The use of narrow-linewidth SFLs has the potential to improve measurement sensitivity by enhancing the sensor's ability to resolve small resonant frequency shifts. Moreover, integration of the SFL will enable a complete chip-scale high-sensitivity biomolecular sensor.

Recent developments in the field of microelectromechanical (MEMS) VCSELs hold promise for SFLs with extremely high chirp rates [107]. These devices are based on an electrically-tunable MEMS mirror, and are capable of sweeping a bandwidth of 100 nm at a wavelength of 1060 nm, with repetition rates exceeding 100 kHz. This corresponds to a chirp rate $> 10^{18}$ Hz/sec, which is two orders of magnitude higher than the fastest SFLs constructed with conventional SCLs.

Our chirped-waveform CBC experiments are currently being repeated at 1060 nm using the VCSEL-based SFL. This is the wavelength of choice for high-power laser sources because of the extremely efficient Yb-doped fiber amplifier technology. The development of an SFL based on the 1060 nm MEMS VCSEL will yield unprecedented chirped-seed SBS suppression results, due to the extremely high chirp rates attainable with these devices.

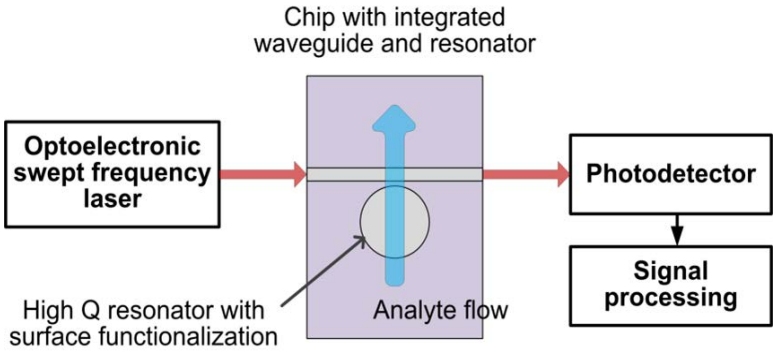

Figure 7.3: Schematic representation of the label-free biomolecular sensing system

TomICam experiments aimed at demonstrating full 3-D imaging capability using a low-cost silicon CCD camera are currently being performed in our group. These experiments rely on our 1060 nm DFB and VCSEL SFLs for illumination. A preferred wavelength for silicon sensors is 850 nm, and we are currently developing an 850 nm VCSEL-based SFL to address this demand. Recently-demonstrated 850 nm MEMS VCSELs [108] can be used to build SFLs that will enable μm-scale axial resolutions in our TomICam systems. An alternative path towards increasing TomICam axial resolution is through the use of MS-FMCW. Hardware stitching can be adopted to the TomICam platform in a very straightforward way, and an array of 850 nm VCSELs can therefore be used for broadband swept-frequency illumination.

In summary, electronic control over the frequency of semiconductor lasers enables a range of swept-frequency applications, from spectroscopy and biomolecular sensing, to ranging and 3-D imaging, to stimulated Brillouin scattering suppression in, and coherent combining of high-power fiber amplifiers. Continuing development and integration of the SFL technology holds promise for chip-scale coherent sensing and 3-D imaging systems.

Appendix A

Time-Domain Phase Analysis Using I/Q Demodulation

In this appendix we describe the in-phase and quadrature (I/Q) demodulation technique which is used for time-domain analysis of the locked-state OPLL phase error in chapter 6.

The goal of the technique is to separate the amplitude modulation $A(t)$ from the phase modulation $\theta(t)$ of a sinusoidal signal $y(t)$ with a known frequency ω_0,

$$y(t) = A(t)\sin\left[\omega_0 t + \theta(t)\right]. \tag{A.1}$$

We form the in-phase signal $y_i(t)$ and the quadrature signal $y_q(t)$ by multiplying $y(t)$ with sine and cosine waveforms at a frequency of ω_0, and low-pass filtering the results.

$$\begin{aligned} y_i(t) &= h(t) \star \left[y(t)\sin\omega_0 t\right] \\ &= h(t) \star \left\{ \frac{A(t)}{2}\cos\theta(t) - \frac{A(t)}{2}\cos\left[2\omega_0 t + \theta(t)\right] \right\}, \text{ and} \end{aligned} \tag{A.2}$$

$$\begin{aligned} y_q(t) &= h(t) \star \left[y(t)\cos\omega_0 t\right] \\ &= h(t) \star \left\{ \frac{A(t)}{2}\sin\theta(t) + \frac{A(t)}{2}\sin\left[2\omega_0 t + \theta(t)\right] \right\}, \end{aligned} \tag{A.3}$$

where $h(t)$ is the impulse response of the low-pass filter, and '$\star$' denotes the convolution operation. The filter is designed to average out the sum frequency terms at

frequency $2\omega_0$, while retaining the difference frequency terms at DC, yielding

$$y_i(t) = \frac{A(t)}{2}\cos\theta(t), \text{ and} \tag{A.4}$$

$$y_q(t) = \frac{A(t)}{2}\sin\theta(t). \tag{A.5}$$

The amplitude and phase modulations are recovered using

$$A(t) = 2\sqrt{y_i^2(t) + y_q^2(t)}, \text{ and} \tag{A.6}$$

$$\theta(t) = \text{atan2}\left[y_q(t), y_i(t)\right], \tag{A.7}$$

where $\text{atan2}(y_q, y_i)$ is the four-quadrant inverse tangent function defined below.

$$\text{atan2}(y_q, y_i) \equiv \begin{cases} \tan^{-1}\left(\frac{y_q}{y_i}\right) & y_i > 0 \\ \tan^{-1}\left(\frac{y_q}{y_i}\right) + \pi & y_q \geq 0,\ y_i < 0 \\ \tan^{-1}\left(\frac{y_q}{y_i}\right) - \pi & y_q < 0,\ y_i < 0 \\ +\frac{pi}{2} & y_q > 0,\ y_i = 0 \\ -\frac{pi}{2} & y_q < 0,\ y_i = 0 \\ \text{undefined} & y_q = 0,\ y_i = 0 \end{cases} \tag{A.8}$$

Appendix B

Phase-Noise-Limited Tiled-Aperture Fringe Visibility

We consider the case of tiled-aperture CBC with two emitters. We assume that the emitters have equal intensities and are phase-locked with a residual phase error $\delta\theta_{12}(t)$. The far-field intensity at location $\boldsymbol{r}$ is then given by:

$$I \propto \langle |1 + \exp\left[j\theta_{12}(\boldsymbol{r}) + j\delta\theta_{12}(t)\right]|^2 \rangle_t = 2 + 2e^{-\sigma_{12}^2/2} \cos\theta_{12}(\boldsymbol{r}), \tag{B.1}$$

where $\theta_{12}(\boldsymbol{r})$ is the mean phase difference between the beams at the point $\boldsymbol{r}$ and $\langle\rangle_t$ denotes an average over time. We assumed that $\delta\theta_{12}(t)$ is a zero-mean Gaussian random variable with variance σ_{12}^2, so that $\langle e^{j\delta\theta_{12}(t)} \rangle_t = e^{-\sigma_{12}^2/2}$. Intensity extrema are found at points of constructive and destructive interference, with $\cos\theta_{12}(\boldsymbol{r}) = \pm 1$. The fringe visibility is therefore given by:

$$V \equiv (I_{max} - I_{min})/(I_{max} + I_{min}) = e^{-\sigma_{12}^2/2} \tag{B.2}$$

Strictly speaking, this derivation applies only to single-frequency beams, since in the chirped case the propagation phase θ_{12} is a function of both $\boldsymbol{r}$ and t. However, equation (B.2) still applies to the chirped-seed CBC experiments of chapter 6, because the frequency ranges considered there are $\sim 0.25\%$ of the nominal lasing frequency. Chirp ranges that constitute a significant fraction of the lasing frequency require a more sophisticated analysis based, for example, on chirped Gaussian modes [109].

Bibliography

[1] N. Satyan, A. Vasilyev, G. Rakuljic, V. Leyva, and A. Yariv, "Precise control of broadband frequency chirps using optoelectronic feedback," *Opt. Express*, vol. 17, no. 18, pp. 15991–15999, 2009.

[2] K. Iiyama, L.-T. Wang, and K. Hayashi, "Linearizing optical frequency-sweep of a laser diode for fmcw reflectometry," *Lightwave Technology, Journal of*, vol. 14, no. 2, pp. 173–178, 1996.

[3] P. A. Roos, R. R. Reibel, T. Berg, B. Kaylor, Z. W. Barber, and W. R. Babbitt, "Ultrabroadband optical chirp linearization for precision metrology applications," *Opt. Lett.*, vol. 34, pp. 3692–3694, Dec 2009.

[4] M. Young, T. Koch, U. Koren, D. Tennant, B. Miller, M. Chien, and K. Feder, "Wavelength uniformity in lambda;/4 shifted dfb laser array wdm transmitters," *Electronics Letters*, vol. 31, no. 20, pp. 1750–1752, 1995.

[5] A. Yariv, "Dynamic analysis of the semiconductor laser as a current-controlled oscillator in the optical phased-lock loop: applications," *Opt. Lett.*, vol. 30, pp. 2191–2193, Sep 2005.

[6] N. Satyan, *Optoelectronic control of the phase and frequency of semiconductor lasers*. PhD thesis, California Institute of Technology, 2011.

[7] N. Satyan, W. Liang, and A. Yariv, "Coherence cloning using semiconductor laser optical phase-lock loops," *Quantum Electronics, IEEE Journal of*, vol. 45, no. 7, pp. 755–761, 2009.

[8] N. Satyan, W. Liang, A. Kewitsch, G. Rakuljic, and A. Yariv, "Coherent power combination of semiconductor lasers using optical phase-lock loops," *Selected Topics in Quantum Electronics, IEEE Journal of*, vol. 15, no. 2, pp. 240–247, 2009.

[9] N. Satyan, A. Vasilyev, W. Liang, G. Rakuljic, and A. Yariv, "Sideband locking of a single-section semiconductor distributed-feedback laser in an optical phase-lock loop," *Opt. Lett.*, vol. 34, pp. 3256–3258, Nov 2009.

[10] N. Satyan, A. Vasilyev, G. Rakuljic, J. O. White, and A. Yariv, "Phase-locking and coherent power combining of broadband linearly chirped optical waves," *Opt. Express*, vol. 20, pp. 25213–25227, Nov 2012.

[11] N. Satyan, A. Vasilyev, G. Rakuljic, J. O. White, and A. Yariv, "Phase-locking and coherent power combining of linearly chirped optical waves," in *Conference on Lasers and Electro-Optics 2012*, p. CF2N.1, Optical Society of America, 2012.

[12] A. Vasilyev, E. Petersen, N. Satyan, G. Rakuljic, A. Yariv, and J. O. White, "Coherent power combining of chirped-seed erbium-doped fiber amplifiers," *Photonics Technology Letters, IEEE*, Forthcoming 2013.

[13] A. Vasilyev, N. Satyan, S. Xu, G. Rakuljic, and A. Yariv, "Multiple source frequency-modulated continuous-wave optical reflectometry: theory and experiment," *Appl. Opt.*, vol. 49, pp. 1932–1937, Apr 2010.

[14] A. Vasilyev, N. Satyan, G. Rakuljic, and A. Yariv, "Terahertz chirp generation using frequency stitched vcsels for increased lidar resolution," in *Conference on Lasers and Electro-Optics 2012*, p. CF3C.1, Optical Society of America, 2012.

[15] J. Sendowski, *On-chip integrated label-free optical biosensing system.* PhD thesis, California Institute of Technology, 2013.

[16] A. McCarthy, R. J. Collins, N. J. Krichel, V. Fernández, A. M. Wallace, and G. S. Buller, "Long-range time-of-flight scanning sensor based on high-speed

time-correlated single-photon counting," *Appl. Opt.*, vol. 48, pp. 6241–6251, Nov 2009.

[17] A. Kirmani, A. Colaço, F. N. C. Wong, and V. K. Goyal, "Exploiting sparsity in time-of-flight range acquisition using a single time-resolved sensor," *Opt. Express*, vol. 19, pp. 21485–21507, Oct 2011.

[18] A. Dieckmann, "FMCW-LIDAR with tunable twin-guide laser diode," *Electronics Letters*, vol. 30, pp. 308–309, Feb 1994.

[19] K. W. Holman, D. G. Kocher, and S. Kaushik, "MIT/LL development of broadband linear frequency chirp for high resolution ladar," vol. 6572, p. 65720J, SPIE, 2007.

[20] M. A. Choma, K. Hsu, and J. A. Izatt, "Swept source optical coherence tomography using an all-fiber 1300-nm ring laser source," *Journal of Biomedical Optics*, vol. 10, no. 4, p. 044009, 2005.

[21] R. Motaghiannezam and S. Fraser, "In vivo human retinal and choroidal vasculature visualization using differential phase contrast swept source optical coherence tomography at 1060 nm," pp. 821304–7, 2012.

[22] C. Ndiaye, T. Hara, and H. Ito, "Profilometry using a frequency-shifted feedback laser," in *Lasers and Electro-Optics, 2005. (CLEO). Conference on*, vol. 3, pp. 1757–1759 Vol. 3, May 2005.

[23] T. Anna, C. Shakher, and D. S. Mehta, "Simultaneous tomography and topography of silicon integrated circuits using full-field swept-source optical coherence tomography," *Journal of Optics A: Pure and Applied Optics*, vol. 11, no. 4, p. 045501, 2009.

[24] J. Kittler, A. Hilton, M. Hamouz, and J. Illingworth, "3D Assisted Face Recognition: A Survey of 3D Imaging, Modelling and Recognition Approaches," in *Computer Vision and Pattern Recognition - Workshops, 2005. CVPR Workshops. IEEE Computer Society Conference on*, pp. 114–114, June 2005.

[25] S. K. Dubey, T. Anna, C. Shakher, and D. S. Mehta, "Fingerprint detection using full-field swept-source optical coherence tomography," *Applied Physics Letters*, vol. 91, no. 18, p. 181106, 2007.

[26] S. H. Yun, G. J. Tearney, B. J. Vakoc, M. Shishkov, W. Y. Oh, A. E. Desjardins, M. J. Suter, R. C. Chan, J. A. Evans, I.-K. Jang, N. S. Nishioka, J. F. de Boer, and B. E. Bouma, "Comprehensive volumetric optical microscopy in vivo," *Nat Med*, vol. 12, pp. 1429–1433, Dec 2006.

[27] "A third industrial revolution," *The Economist*. Apr 21, 2012.

[28] G. Bonnema, K. Cardinal, J. McNally, S. Williams, and J. Barton, "Assessment of blood vessel mimics with optical coherence tomography," *Journal of biomedical optics*, vol. 12, no. 2, pp. 024018–024018, 2007.

[29] P. Bagnaninchi, Y. Yang, N. Zghoul, N. Maffulli, R. Wang, and A. Haj, "Chitosan microchannel scaffolds for tendon tissue engineering characterized using optical coherence tomography," *Tissue engineering*, vol. 13, no. 2, pp. 323–331, 2007.

[30] Y. Yang, A. Dubois, X. Qin, J. Li, A. E. Haj, and R. K. Wang, "Investigation of optical coherence tomography as an imaging modality in tissue engineering," *Physics in Medicine and Biology*, vol. 51, no. 7, p. 1649, 2006.

[31] M. Rimann and U. Graf-Hausner, "Synthetic 3D multicellular systems for drug development," *Current opinion in biotechnology*, 2012.

[32] Y. Aoki, K. Tajima, and I. Mito, "Input power limits of single-mode optical fibers due to stimulated brillouin scattering in optical communication systems," *Lightwave Technology, Journal of*, vol. 6, no. 5, pp. 710–719, May.

[33] G. D. Goodno, S. J. McNaught, J. E. Rothenberg, T. S. McComb, P. A. Thielen, M. G. Wickham, and M. E. Weber, "Active phase and polarization locking of a 1.4 kw fiber amplifier," *Opt. Lett.*, vol. 35, pp. 1542–1544, May 2010.

[34] S. B. Weiss, M. Weber, and G. Goodno, "Group delay locking of broadband phased lasers," in *Lasers, Sources, and Related Photonic Devices*, p. AM3A.5, Optical Society of America, 2012.

[35] J. O. White, A. Vasilyev, J. P. Cahill, N. Satyan, O. Okusaga, G. Rakuljic, C. E. Mungan, and A. Yariv, "Suppression of stimulated brillouin scattering in optical fibers using a linearly chirped diode laser," *Opt. Express*, vol. 20, pp. 15872–15881, Jul 2012.

[36] C. Mungan, S. Rogers, N. Satyan, and J. White, "Time-dependent modeling of brillouin scattering in optical fibers excited by a chirped diode laser," *Quantum Electronics, IEEE Journal of*, vol. 48, no. 12, pp. 1542–1546, Dec.

[37] M.-C. Amann, T. Bosch, M. Lescure, R. Myllylä, and M. Rioux, "Laser ranging: a critical review of usual techniques for distance measurement," *Optical Engineering*, vol. 40, no. 1, pp. 10–19, 2001.

[38] S. Venkatesh and W. V. Sorin, "Phase noise considerations in coherent optical fmcw reflectometry," *Lightwave Technology, Journal of*, vol. 11, no. 10, pp. 1694–1700, 1993.

[39] I. Komarov and S. Smolskiy, *Fundamentals of short-range FM radar*. Artech House, 2003.

[40] A. Yariv, *Quantum Electronics*. John Wiley, 1975.

[41] M. Lax, "Classical noise. v. noise in self-sustained oscillators," *Phys. Rev.*, vol. 160, pp. 290–307, Aug 1967.

[42] C. Henry, "Theory of the linewidth of semiconductor lasers," *Quantum Electronics, IEEE Journal of*, vol. 18, no. 2, pp. 259–264, 1982.

[43] M. O'Mahony and I. Henning, "Semiconductor laser linewidth broadening due to 1/f carrier noise," *Electronics Letters*, vol. 19, no. 23, pp. 1000–1001, 1983.

[44] L. Cutler and C. Searle, "Some aspects of the theory and measurement of frequency fluctuations in frequency standards," *Proceedings of the IEEE*, vol. 54, no. 2, pp. 136–154, 1966.

[45] A. Kersey, M. Marrone, A. Dandridge, and A. B. Tveten, "Optimization and stabilization of visibility in interferometric fiber-optic sensors using input-polarization control," *Lightwave Technology, Journal of*, vol. 6, no. 10, pp. 1599–1609, 1988.

[46] L. Richter, H. Mandelberg, M. Kruger, and P. McGrath, "Linewidth determination from self-heterodyne measurements with subcoherence delay times," *Quantum Electronics, IEEE Journal of*, vol. 22, no. 11, pp. 2070–2074, 1986.

[47] E. Strzelecki, D. Cohen, and L. Coldren, "Investigation of tunable single frequency diode lasers for sensor applications," *Lightwave Technology, Journal of*, vol. 6, pp. 1610–1618, Oct 1988.

[48] S. H. Yun, C. Boudoux, G. J. Tearney, and B. E. Bouma, "High-speed wavelength-swept semiconductor laser with a polygon-scanner-based wavelength filter," *Opt. Lett.*, vol. 28, no. 20, pp. 1981–1983, 2003.

[49] W. Y. Oh, S. H. Yun, G. J. Tearney, and B. E. Bouma, "115 khz tuning repetition rate ultrahigh-speed wavelength-swept semiconductor laser," *Opt. Lett.*, vol. 30, pp. 3159–3161, Dec 2005.

[50] H. Lim, J. De Boer, B. Park, E. Lee, R. Yelin, and S. Yun, "Optical frequency domain imaging with a rapidly swept laser in the 815-870 nm range," *Opt. Express*, vol. 14, no. 13, pp. 5937–5944, 2006.

[51] F. Gardner, *Phaselock Techniques*. Wiley, 2005.

[52] S. Saito, O. Nilsson, and Y. Yamamoto, "Coherent fsk transmitter using a negative feedback stabilised semiconductor laser," *Electronics Letters*, vol. 20, no. 17, pp. 703–704, 1984.

[53] P. Corrc, O. Girad, and J. De Faria, I.F., "On the thermal contribution to the fm response of dfb lasers: theory and experiment," *Quantum Electronics, IEEE Journal of*, vol. 30, no. 11, pp. 2485–2490, 1994.

[54] G. Pandian and S. Dilwali, "On the thermal fm response of a semiconductor laser diode," *Photonics Technology Letters, IEEE*, vol. 4, no. 2, pp. 130–133, 1992.

[55] A. Hangauer, J. Chen, R. Strzoda, and M.-C. Amann, "The frequency modulation response of vertical-cavity surface-emitting lasers: Experiment and theory," *Selected Topics in Quantum Electronics, IEEE Journal of*, vol. 17, no. 6, pp. 1584–1593, 2011.

[56] W. V. Sorin, K. W. Chang, G. A. Conrad, and P. R. Hernday, "Frequency domain analysis of an optical fm discriminator," *Lightwave Technology, Journal of*, vol. 10, no. 6, pp. 787–793, 1992.

[57] J. T. Ahn, H. K. Lee, K. H. Kim, M.-Y. Jeon, D. S. Lim, and E.-H. Lee, "A stabilised fibre-optic mach-zehnder interferometer filter using an independent stabilisation light source," *Optics Communications*, vol. 157, no. 16, pp. 62–66, 1998.

[58] Y. Kokubun, N. Funato, and M. Takizawa, "Athermal waveguides for temperature independent lightwave devices," *Photonics Technology Letters, IEEE*, vol. 5, no. 11, pp. 1297–1300, 1993.

[59] T. G. McRae, S. Ngo, D. A. Shaddock, M. T. L. Hsu, and M. B. Gray, "Frequency stabilization for space-based missions using optical fiber interferometry," *Opt. Lett.*, vol. 38, pp. 278–280, Feb 2013.

[60] B. Nagler, M. Peeters, J. Albert, G. Verschaffelt, K. Panajotov, H. Thienpont, I. Veretennicoff, J. Danckaert, S. Barbay, G. Giacomelli, *et al.*, "Polarization-mode hopping in single-mode vertical-cavity surface-emitting lasers: Theory

and experiment," *PHYSICAL REVIEW-SERIES A-*, vol. 68, no. 1, pp. 013813–013813, 2003.

[61] S. Li, X. Jin, X. Zhang, and Y. K. Zou, "Digitally controlled programmable high-speed variable optical attenuator," *Microwave and Optical Technology Letters*, vol. 48, no. 6, pp. 1019–1021, 2006.

[62] J. Mork, A. Mecozzi, and G. Eisenstein, "The modulation response of a semiconductor laser amplifier," *Selected Topics in Quantum Electronics, IEEE Journal of*, vol. 5, no. 3, pp. 851–860, 1999.

[63] M. K. K. Leung, A. Mariampillai, B. A. Standish, K. K. C. Lee, N. R. Munce, I. A. Vitkin, and V. X. D. Yang, "High-power wavelength-swept laser in littman telescope-less polygon filter and dual-amplifier configuration for multichannel optical coherence tomography," *Opt. Lett.*, vol. 34, pp. 2814–2816, Sep 2009.

[64] R. Huber, M. Wojtkowski, and J. G. Fujimoto, "Fourier Domain Mode Locking (FDML): A new laser operating regime and applications for optical coherence tomography," *Opt. Express*, vol. 14, pp. 3225–3237, Apr 2006.

[65] C. Chong, T. Suzuki, A. Morosawa, and T. Sakai, "Spectral narrowing effect by quasi-phase continuous tuning in high-speed wavelength-swept light source," *Opt. Express*, vol. 16, pp. 21105–21118, Dec 2008.

[66] J. C. Marron and K. W. Gleichman, "Three-dimensional imaging using a tunable laser source," *Optical Engineering*, vol. 39, no. 1, pp. 47–51, 2000.

[67] M. L. Simpson, C. A. Bennett, M. S. Emery, D. P. Hutchinson, G. H. Miller, R. K. Richards, and D. N. Sitter, "Coherent imaging with two-dimensional focal-plane arrays: design and applications.," *Applied Optics*, vol. 36, no. 27, pp. 6913–6920, 1997.

[68] W. van der Mark and D. Gavrila, "Real-time dense stereo for intelligent vehicles," *Intelligent Transportation Systems, IEEE Transactions on*, vol. 7, pp. 38 –50, march 2006.

[69] R. Baraniuk, A. Davenport, Mark, F. Durate, Marco, and C. Hedge, eds., *An Introduction to Compressive Sensing*. Connexions, 2011.

[70] S. Foix, G. Alenya, and C. Torras, "Lock-in Time-of-Flight (ToF) Cameras: A Survey," *Sensors Journal, IEEE*, vol. 11, pp. 1917–1926, sept. 2011.

[71] M. Young, E. Lebed, Y. Jian, P. J. Mackenzie, M. F. Beg, and M. V. Sarunic, "Real-time high-speed volumetric imaging using compressive sampling optical coherence tomography," *Biomed. Opt. Express*, vol. 2, pp. 2690–2697, Sep 2011.

[72] S. Boyd and L. Vandenberghe, *Convex optimization*. Cambridge, UK: Cambridge University Press, 2009.

[73] M. Fornasier and H. Rauhut, "Compressive sensing," in *Handbook of Mathematical Methods in Imaging* (O. Scherzer, ed.), pp. 187–228, Springer New York, 2011.

[74] J. Simsarian, M. Larson, H. Garrett, H. Xu, and T. Strand, "Less than 5-ns wavelength switching with an SG-DBR laser," *Photonics Technology Letters, IEEE*, vol. 18, pp. 565–567, 15, 2006.

[75] J. Wesström, S. Hammerfeldt, J. Buus, R. Siljan, R. Laroy, and H. De Vries, "Design of a widely tunable modulated grating Y-branch laser using the additive Vernier effect for improved super-mode selection," in *Proc. of 18th Int. Semiconductor Laser Conf.(ISLC), Garmisch, Germany*, 2002.

[76] H. Rauhut, "Compressive Sensing and Structured Random Matrices," in *Theoretical Foundations and Numerical Methods for Sparse Recovery* (M. Fornasier, ed.), vol. 9 of *Radon Series Comp. Appl. Math.*, pp. 1–92, deGruyter, 2010.

[77] M. P. Minneman, J. Ensher, M. Crawford, and D. Derickson, "All semiconductor high-speed akinetic swept-source for OCT," pp. 831116–831116–10, 2011.

[78] H. K. Philipp, A. Scholtz, E. Bonek, and W. Leeb, "Costas loop experiments for a 10.6 μm communications receiver," *Communications, IEEE Transactions on*, vol. 31, no. 8, pp. 1000–1002, 1983.

[79] L. G. Kazovsky, "Performance analysis and laser linewidth requirements for optical psk heterodyne communications systems," *Lightwave Technology, Journal of*, vol. 4, no. 4, pp. 415–425, 1986.

[80] J. Kahn, A. Gnauck, J. Veselka, S. Korotky, and B. L. Kasper, "4-gb/s psk homodyne transmission system using phase-locked semiconductor lasers," *Photonics Technology Letters, IEEE*, vol. 2, no. 4, pp. 285–287, 1990.

[81] F. Herzog, K. Kudielka, D. Erni, and W. Bächtold, "Optical phase locked loop for transparent inter-satellite communications," *Opt. Express*, vol. 13, pp. 3816–3821, May 2005.

[82] U. Gliese, T. Nielsen, M. Bruun, E. Lintz Christensen, K. Stubkjaer, S. Lindgren, and B. Broberg, "A wideband heterodyne optical phase-locked loop for generation of $3 - 18$ GHz microwave carriers," *Photonics Technology Letters, IEEE*, vol. 4, no. 8, pp. 936–938, 1992.

[83] L. Johansson and A. Seeds, "Millimeter-wave modulated optical signal generation with high spectral purity and wide-locking bandwidth using a fiber-integrated optical injection phase-lock loop," *Photonics Technology Letters, IEEE*, vol. 12, no. 6, pp. 690–692, 2000.

[84] S. Takasaka, Y. Ozeki, S. Namiki, and M. Sakano, "External synchronization of 160-ghz optical beat signal by optical phase-locked loop technique," *Photonics Technology Letters, IEEE*, vol. 18, no. 23, pp. 2457–2459, 2006.

[85] T. von Lerber, S. Honkanen, A. Tervonen, H. Ludvigsen, and F. Kuppers, "Optical clock recovery methods: Review (invited)," *Optical Fiber Technology*, vol. 15, no. 4, pp. 363 – 372, 2009.

[86] T. Fan, "Laser beam combining for high-power, high-radiance sources," *Selected Topics in Quantum Electronics, IEEE Journal of*, vol. 11, no. 3, pp. 567–577, 2005.

[87] L. Bartelt-Berger, U. Brauch, A. Giesen, H. Huegel, and H. Opower, "Power-scalable system of phase-locked single-mode diode lasers," *Appl. Opt.*, vol. 38, pp. 5752–5760, Sep 1999.

[88] S. J. Augst, T. Y. Fan, and A. Sanchez, "Coherent beam combining and phase noise measurements of ytterbium fiber amplifiers," *Opt. Lett.*, vol. 29, pp. 474–476, Mar 2004.

[89] C. X. Yu, J. E. Kansky, S. E. J. Shaw, D. Murphy, and C. Higgs, "Coherent beam combining of large number of pm fibres in 2-d fibre array," *Electronics Letters*, vol. 42, no. 18, pp. 1024–1025, 2006.

[90] S. J. Augst, J. K. Ranka, T. Y. Fan, and A. Sanchez, "Beam combining of ytterbium fiber amplifiers (invited)," *J. Opt. Soc. Am. B*, vol. 24, pp. 1707–1715, Aug 2007.

[91] W. Liang, N. Satyan, A. Yariv, A. Kewitsch, G. Rakuljic, F. Aflatouni, H. Hashemi, and J. Ungar, "Coherent power combination of two master-oscillator-power-amplifier (MOPA) semiconductor lasers using optical phase lock loops," *Opt. Express*, vol. 15, pp. 3201–3205, Mar 2007.

[92] S. A. Diddams, D. J. Jones, J. Ye, S. T. Cundiff, J. L. Hall, J. K. Ranka, R. S. Windeler, R. Holzwarth, T. Udem, and T. W. Hänsch, "Direct link between microwave and optical frequencies with a 300 THz femtosecond laser comb," *Phys. Rev. Lett.*, vol. 84, pp. 5102–5105, May 2000.

[93] L.-S. Ma, Z. Bi, A. Bartels, L. Robertsson, M. Zucco, R. S. Windeler, G. Wilpers, C. Oates, L. Hollberg, and S. A. Diddams, "Optical frequency synthesis and comparison with uncertainty at the 10-19 level," *Science*, vol. 303, no. 5665, pp. 1843–1845, 2004.

[94] E. Seise, A. Klenke, S. Breitkopf, M. Plötner, J. Limpert, and A. Tünnermann, "Coherently combined fiber laser system delivering 120 μj femtosecond pulses," *Opt. Lett.*, vol. 36, pp. 439–441, Feb 2011.

[95] K. Shiraki, M. Ohashi, and M. Tateda, "SBS threshold of a fiber with a brillouin frequency shift distribution," *Lightwave Technology, Journal of*, vol. 14, no. 1, pp. 50–57, Jan.

[96] J. Hansryd, F. Dross, M. Westlund, P. Andrekson, and S. Knudsen, "Increase of the SBS threshold in a short highly nonlinear fiber by applying a temperature distribution," *Lightwave Technology, Journal of*, vol. 19, no. 11, pp. 1691–1697, 2001.

[97] J. M. C. Boggio, J. D. Marconi, and H. L. Fragnito, "Experimental and numerical investigation of the SBS-threshold increase in an optical fiber by applying strain distributions," *J. Lightwave Technol.*, vol. 23, p. 3808, Nov 2005.

[98] G. D. Goodno, C.-C. Shih, and J. E. Rothenberg, "Perturbative analysis of coherent combining efficiency with mismatched lasers," *Opt. Express*, vol. 18, pp. 25403–25414, Nov 2010.

[99] G. D. Goodno, C.-C. Shih, and J. E. Rothenberg, "Perturbative analysis of coherent combining efficiency with mismatched lasers: errata," *Opt. Express*, vol. 20, pp. 23587–23588, Oct 2012.

[100] D. Botez, "High-power monolithic phase-locked arrays of antiguided semiconductor diode lasers," *Optoelectronics, IEEE Proceedings J*, vol. 139, no. 1, pp. 14–23, 1992.

[101] D. G. Youmans, "Phase locking of adjacent channel leaky waveguide co2 lasers," *Applied Physics Letters*, vol. 44, no. 4, pp. 365–367, 1984.

[102] J. R. Leger, M. L. Scott, and W. B. Veldkamp, "Coherent addition of AlGaAs lasers using microlenses and diffractive coupling," *Applied Physics Letters*, vol. 52, no. 21, pp. 1771–1773, 1988.

[103] Y. Kono, M. Takeoka, K. Uto, A. Uchida, and F. Kannari, "A coherent all-solid-state laser array using the Talbot effect in a three-mirror cavity," *Quantum Electronics, IEEE Journal of*, vol. 36, no. 5, pp. 607–614, 2000.

[104] L. Langley, M. D. Elkin, C. Edge, M. Wale, U. Gliese, X. Huang, and A. Seeds, "Packaged semiconductor laser optical phase-locked loop (opll) for photonic generation, processing and transmission of microwave signals," *Microwave Theory and Techniques, IEEE Transactions on*, vol. 47, no. 7, pp. 1257–1264, 1999.

[105] C. D. Nabors, "Effects of phase errors on coherent emitter arrays," *Appl. Opt.*, vol. 33, pp. 2284–2289, Apr 1994.

[106] C. Santis, *High-coherence Hybrid Si/III-V Semiconductor Lasers*. PhD thesis, California Institute of Technology, 2013.

[107] V. Jayaraman, G. Cole, M. Robertson, C. Burgner, D. John, A. Uddin, and A. Cable, "Rapidly swept, ultra-widely-tunable 1060 nm MEMS-VCSELs," *Electronics letters*, vol. 48, no. 21, pp. 1331–1333, 2012.

[108] H. A. Davani, C. Grasse, B. Kögel, C. Gierl, K. Zogal, T. Gründl, P. Westbergh, S. Jatta, G. Böhm, P. Meissner, *et al.*, "Widely electro thermal tunable bulk-micromachined MEMS-VCSEL operating around 850nm," in *Conference on Lasers and Electro-Optics/Pacific Rim*, Optical Society of America, 2011.

[109] F. Sohbatzadeh, S. Mirzanejhad, H. Aku, and S. Ashouri, "Chirped Gaussian laser beam parameters in paraxial approximation," *Physics of Plasmas*, vol. 17, Aug 2010.